TECHNISCHE
UNIVERSITÄT
WIEN

DISSERTATION

Through process modeling of microalloyed steel production

Ausgeführt zum Zwecke der Erlangung des akademischen Grades einer Doktorin der technischen Wissenschaften unter der Leitung von

Univ.Prof. Dipl.-Ing. Dr.techn. Ernst Kozeschnik
E 308
Institut für Werkstoffwissenschaft und Werkstofftechnologie

eingereicht an der Technischen Universität Wien
Fakultät für Maschinenwesen und Betriebswissenschaften

von
Dipl.-Ing. Sabine Zamberger
9535125
Adam von Lebenwaldweg 8g, A-8700 Leoben

Wien, am

Diese Dissertation haben begutachtet:

Univ.Prof. Dipl.-Ing. Dr.techn. Ernst Kozeschnik

Univ.-Prof. Dr.-Ing. Wolfgang Bleck

Deutsche Kurzfassung

Für Anwendungen, wo höchste Festigkeit und Zähigkeit verlangt werden, werden häufig mikrolegierte Stähle eingesetzt und entsprechend der Anforderungen zielgerichtet entwickelt. Beispiele hierfür sind Stähle für die Automobilindustrie, hochfeste Leitungsrohre und Rohre für den Einsatz in sauergashaltigen Medien. „Mikrolegiert“ bezieht sich in diesem Fall auf die geringen Zusätze an Nb, Ti und V von bis zu 0,1Gew.% im Stahl. Diese Elemente bilden während der Verarbeitung des Werkstoffes Nitride, Karbide und/ oder Karbonitride. Diese Ausscheidungen beeinflussen die Materialeigenschaften signifikant, weshalb es von großem Interesse ist, ihr Ausscheidungsverhalten zu verstehen. Die Ausscheidungskinetik wird durch die chemische Zusammensetzung und die thermo-mechanische Verarbeitung bestimmt. Die Ausscheidungsverteilung, die durch die Ausscheidungsdichte, den Radius und die chemische Zusammensetzung der Ausscheidungen repräsentiert wird, ist einer der Haupteinflussfaktoren für die Kontrolle der Werkstoffeigenschaften. Aufgrund der geringen Größe der Partikel, sie variiert typischerweise zwischen einigen wenigen und ~ 100nm, können sie nur durch hochauflösende Methoden, wie z.B. die Transmissionselektronenmikroskopie (TEM), charakterisiert werden.

Durch den Einsatz der numerischen Simulation können die Ausscheidungsvorgänge im Werkstoff analysiert werden. In weiterer Folge, kann der Ausscheidungszustand vorhergesagt werden und daraus kann eine Aussage über die Materialeigenschaften abgeleitet werden. Dies ermöglicht eine raschere Werkstoffentwicklung und Prozessoptimierung mit reduziertem experimentellen Aufwand und minimierter Anzahl an industriellen Versuchen.

Die vorliegende Arbeit basiert im Wesentlichen auf fünf Fachartikeln (Teil II der Arbeit), die in anerkannten wissenschaftlichen Journalen veröffentlicht wurden. Für die numerische Simulation wurde das thermokinetische Software-Paket MatCalc eingesetzt. Mit dessen Hilfe wurde die Ausscheidungskinetik von mikrolegierten Stählen während ihrer Verarbeitung analysiert und vorhergesagt.

Ziel der vorliegenden Arbeit ist es, eine Methode zu entwickeln, die es erlaubt, den Ausscheidungszustand über die gesamte Prozessroute der Stahlherstellung, -weiterverarbeitung und -anwendung zu analysieren und vorherzusagen. Als Anwendungsbeispiel im konkreten Fall ist der Einsatz in sauergashältigen Medien ausgewählt worden, wobei die Aufnahme und das „Festhalten“ – das „Trapping“ – von H-Atomen an z.B. Oberflächen von Ausscheidungen mit Hilfe der numerischen Simulation untersucht wurde.

Teil I der Dissertation beschreibt die den Artikeln zugrunde liegenden Ideen und Ergebnisse aus zusätzlichen Simulationsrechnungen, um die in Teil II der Dissertation angeführten Fachartikel einzuhüllen und zu ergänzen.

Through process modeling of microalloyed steel production

Sabine Zamberger

Doctoral thesis

Vienna University of Technology,

Faculty for Mechanical and Industrial Engineering

Institute of Materials Science and Technology

December 2015

The research in this thesis was performed at voestalpine Stahl Donawitz GmbH and at the

Institute of Materials Science and Technology,

University of Technology, Vienna, Austria,

within the research activities of the Christian Doppler Laboratory “Early Stages of Precipitation”.

Keywords:

Microalloyed steel, precipitation kinetics, primary precipitates, secondary precipitates, H-trapping

We’ll carry on,

We’ll carry on,

And though you’re dead and gone, believe me,

Your memory will carry on,

We’ll carry on.

[My chemical romance “The Black Parade”]

Acknowledgement

I would like to thank my advisor, Professor Ernst Kozeschnik, for giving me the opportunity to do this research and for his help, encouragement and counsel throughout the project.

Also, I would like to thank Herbert Schifferl, who motivated me to start this work. Special thanks also to Gerald Klösch, who further promoted the activities for this thesis.

I especially thank my family for their great support.

The financial support by the Austrian Federal Ministry of Science, Research and Economy and the National Foundation for Research, technology and Development is gratefully acknowledged.

Donawitz, 2015

Sabine Zamberger

Preface

This thesis is submitted in compliance with the requirements for the degree of technical doctor at the Vienna University of Technology. The doctoral work has been carried out at the Faculty of Mechanical and Industrial Engineering, Institute of Materials Science and Technology, Vienna, Austria.

The thesis is divided into two parts. In the first part, an introduction to the field of process modeling of steel production is given. Then, the underlying concepts for the five papers, given in part two of the thesis, are outlined. The five papers compiled in this cumulative PhD thesis are:

- Zamberger S, Pudar M, Spiradek-Hahn K, Reischl M and Kozeschnik E: Numerical simulation of the evolution of primary and secondary Nb(CN), Ti(CN) and AlN in Nb-microalloyed steel during continuous casting, Int. J. Mat. Res. (formerly Z. Metallkd.) Vol. 103 Is. 6 (2012), 680-687
- Zamberger S and Kozeschnik E: Carbo-nitride precipitation in tempered martensite- computer simulation and experiment, Mat. Sci. Forum, Vols. 706-709 (2012), 1586-1591
- Zamberger S, Wojcik T, Klarner J, Klösch G, Schifferl H and Kozeschnik E: Computational and experimental analysis of carbo-nitride precipitation in tempered martensite, Steel Res. Int. Vol 84 No. 1 (2013), 20-30
- Zamberger S, Whitmore L, Krisam S, Wojcik T and Kozeschnik E: Experimental and computational study of cementite precipitation in tempered martensite, Modelling Simul. Mater. Sci. Eng. 23 (2015) 055012, 22pp
- Zamberger S, Lang P, Klösch G, Klarner J and Kozeschnik E: Long-range diffusion of H in the presence of traps in a microalloyed steel, Comput. Mater. Sci. doi:10.1016/j.commatsci.2015.11.014

Part I

Introduction & Background

S Zamberger

Contents part I

1. Introduction

Microalloyed steel grades are developed for high strength, high toughness applications in the automotive industry, high strength line pipe and severe sourgas uses [e.g. 1-7]. The term microalloyed is related to the minute additions of Nb, Ti and V of up to 0.1wt%, which form nitrides, carbonitrides and carbides. These particles influence the materials properties essentially and the understanding of their precipitation behavior is therefore of greatest interest, see e.g. refs. [8-9]. Precipitation kinetics is influenced by the chemical composition and the thermo-mechanical processing of the steel. The precipitate distribution, which is represented by the number density, radii and chemical composition of the particles, is one of the main ingredients for the control of materials properties. Due to the small dimensions of the secondary particles, their radii typically vary between a few and ~100 nm, they can only be characterized by a considerable experimental effort with high resolution techniques, like transmission electron microscopy (TEM).

Numerical simulation, therefore, offers the opportunity to understand and to predict precipitation kinetics. Consequently, a significant part of the properties of structural materials can be deduced from the precipitate distribution. This enables a faster materials design and process optimization with a reduced number of laboratory and industrial trials.

The present work is based on five papers (part II, [12-16]) that are published in recognized scientific journals and where the thermokinetic software package MatCalc [17] is utilized for the analysis and the prediction of precipitation kinetics in microalloyed steel grades during the different processing steps of the material. The thesis is based on the idea of developing a methodology to investigate and predict the precipitation kinetics of microalloyed steel grades starting from the as-cast condition and ending with the thermo-mechanical properties of the material in service and application. Our application example in the present case is the investigation of the trapping effects of microstructural features for H-atoms, which are essential for steel exposed to sourgas media.

Before going into detail, the next section should provide the ‘big picture’ of the present thesis, the motivation for starting the presented investigations. What follows, is a brief overview of the investigated materials and the characterization methods. The subsequent sections give a detailed description of the ideas behind the technical papers. Results of additionally performed simulations are introduced to support the discussion. Summary and outlook finalize part I of the thesis.

2. ‘The big picture’

This chapter explains the general background, the stimulus why this work has been started. The target has been to investigate precipitation kinetics in microalloyed steel grades by “through process modeling”. So, the first question raised is: what is the initial condition of the material under investigation?

Usually, if one analyses precipitation kinetics of steels numerically, the starting condition is a precipitate free matrix, here: austenite, with some initial heterogeneous nucleation sites like austenite grain boundaries and/or dislocations (fig. 1a) at a certain temperature, T_1. With decreasing temperature, T_2, precipitation starts and one eventually finds an austenite grain with precipitates at triple points, grain boundaries etc. (fig. 1b). Further lowering of the temperature leads to a phase decomposition of austenite into, e.g., ferrite and the precipitation of additional particles.

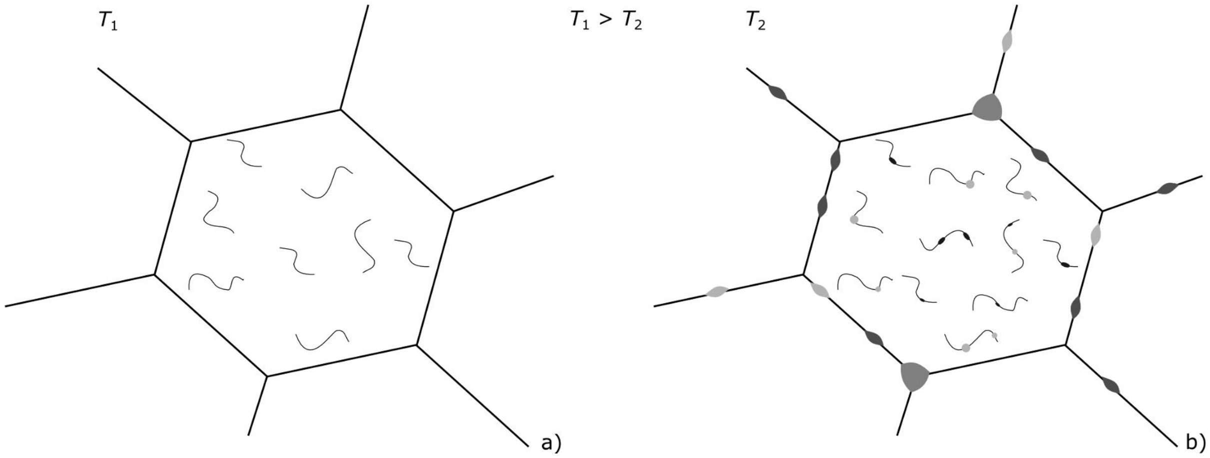

Figure 1: a) Starting condition for the numerical simulation of precipitation kinetics: precipitate free austenite grain with heterogeneous nucleation sites. b) At the lower temperature, T_2, precipitation at grain boundaries and dislocations starts and additional dislocations are induced by cooling and/or deformation.

This starting condition might be true for fully solution annealed material, but in reality, we observed something completely different. Fig. 2 illustrates the results of an electron probe microanalysis in the as-cast condition of the microalloyed steel grade with the composition given in table 1. It is obvious that we do not have a homogeneous chemical composition throughout the material and that primary precipitates are already formed during solidification, which might reduce the amount of the according element in the matrix.

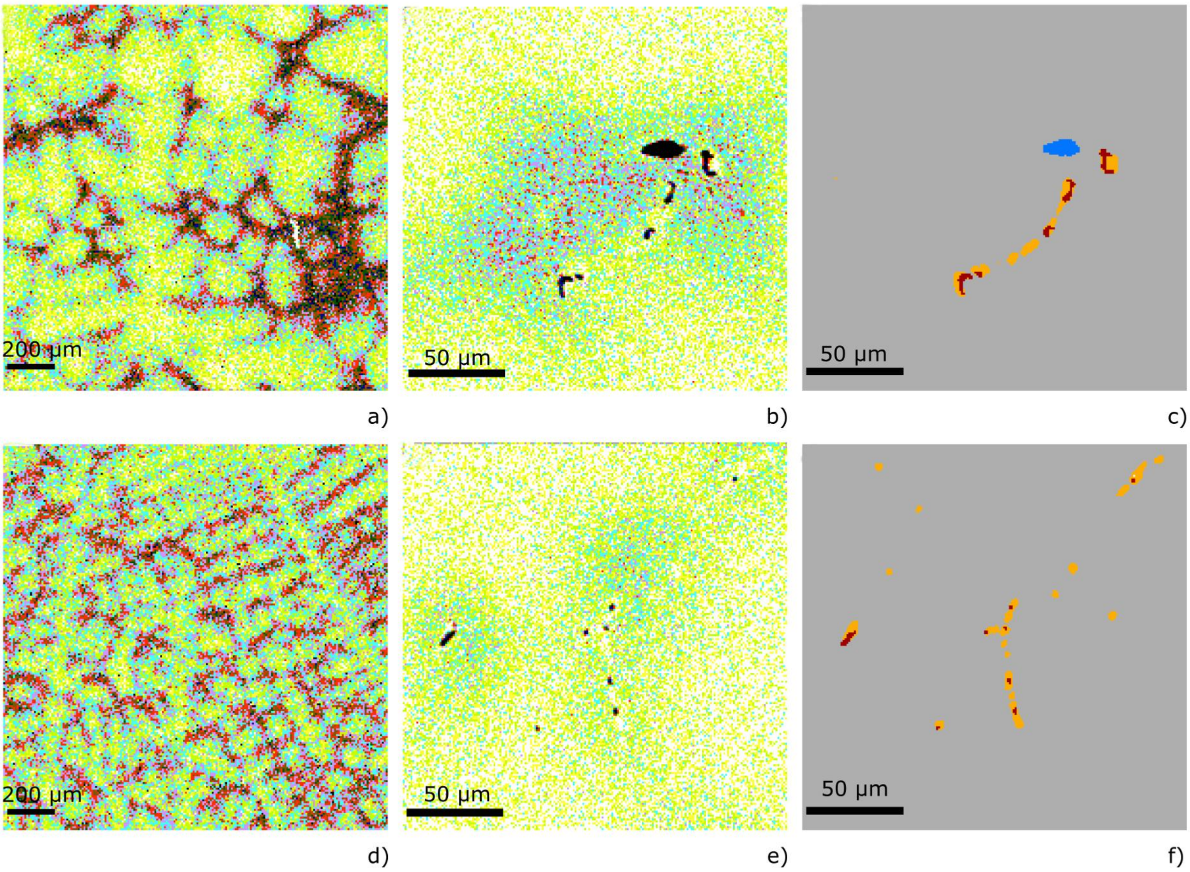

Figure 2: Electron probe microanalysis of a Nb-microalloyed steel; the darker the color, the higher the element concentration. a) to c) stems from a sample taken from the mid-position of a cross-section of the as-cast material. d) to f): elemental mapping from a sub-surface sample. a) and b): Mn-mapping. b) and c): Nb-mapping. c) and f): phase analysis of the primary precipitates shown in b) and e). Blue and red particles are Nb-rich precipitates with differing Nb-contents. Orange particles are MnS precipitates.

The first paper [12] in part II of the theses shows additional experimental results of this steel and, from these investigations, the concept for the first paper is deduced.

After development of the methodology of how to analyze steel, which is not fully solution annealed, the focus of the work is moved on to the next processing step. In this case, we investigate the precipitation kinetics of a V-microalloyed steel, which is reheated to a temperature of 1300°C, hot-rolled, quenched and subsequently tempered at 690°C. The conventional procedure for the computational materials engineering analysis in this kind of materials is to treat Fe_3C, cementite, as para-equilibrium cementite (see chapter 4.2 and ref. [13,15]

for detailed explanations). Here, we found that it is not possible to predict the Fe_3C precipitate distribution according to the experiment, using the para-equilibrium nucleus composition at high annealing temperatures. Beyond that, also the V-rich precipitates and the M_7C_3-carbides are not predicted in a satisfying agreement with the experiments. Similar results are observed in the Nb-Ti-microalloyed steel, which is analyzed in ref. [14]. As a result the model presented in ref. [15] has been developed, with which it has been possible to predict Fe_3C and all other carbides in the material during tempering of a martensitic matrix at all temperatures above 300°C, without defining the nucleus-composition ‘a-priori’.

The last point of interest in the present work is the performance of steel in extreme environment, i.e., conditions where the material has to resist H-embrittlement. Since it is reported in literature, see the references in [16], that precipitates in steel can act as trapping sites for H-atoms, a new model developed by Svoboda and Fischer [18-20], is applied for a detailed study on the influence of particles in a microalloyed steel on the long-range diffusion of H. In that work, for the first time, all models predicting precipitation kinetics [21-29], the diffusion of interstitials in the presence of traps [18-20] and the microstructural evolution with respect to defects [29,30] are integrated into one consistent treatment of hydrogen diffusion and trapping in a multi-component polycrystal microstructure. The results presented in the last of the five papers [16] in part II are obtained by a full coupling of precipitation kinetics calculations and diffusion simulation, which is a novelty in computational materials engineering.

3. Materials and characterization

The steels under investigation are microalloyed C-Mn steels with C contents between 0.20 and 0.35 wt%. The microalloying elements are Nb, Ti and V. The precipitates formed by these elements are of fcc lattice structure and show mutual miscibility for all of the microalloying elements [32-38]. All grades are Al-killed and contain trace amounts of N. Therefore, AlN precipitation is expected. Other carbide forming elements present in the steel alloys are Cr and Mo.

If industrial material is investigated, the processing of the material is as follows: the steel is continuously cast into a format with a dimension of Ø 230 mm. The 'blooms' are subsequently air cooled to room temperature and delivered to the customer. There, the blooms are reheated, rolled and quenched and tempered twice. Fig. 3 sketches the process, the corresponding simulation inputs and results, as well as the applied characterization methods.

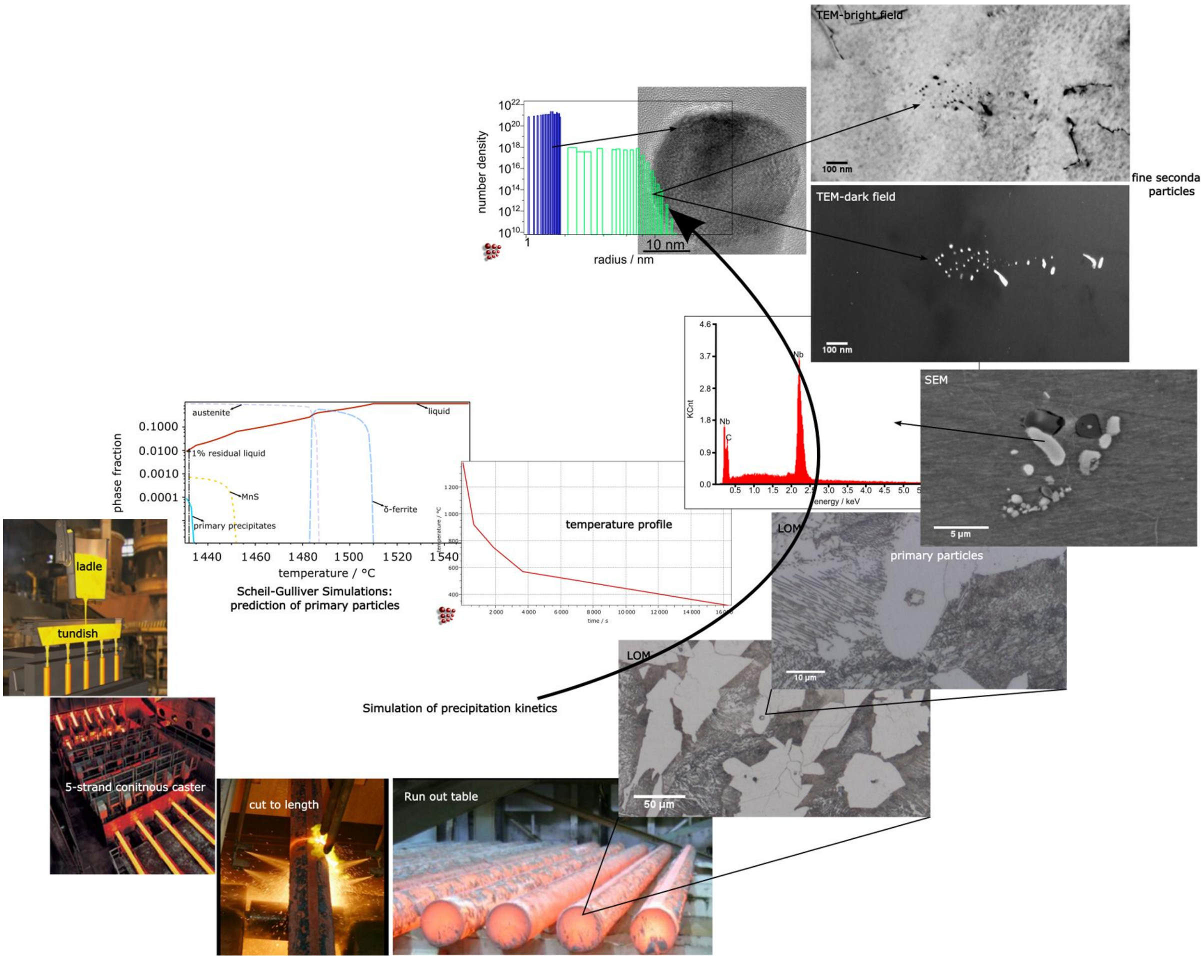

Figure 3: Casting of the industrial material, characterization and examples for results of the numerical simulations.

If the material is produced in laboratory scale, it is cast into blocks of about 150 x 150 mm² with a length of ~300 mm. The as-cast material is ground to avoid surface defects during subsequent rolling. The reheating temperatures are lower than the industrial reheating temperatures. However, the laboratory rolling schedule is in general comparable to the industrial rolling process.

For characterization of the materials, light optical microscopy, automatic scanning electron microscopy energy dispersive x-ray analysis (SEM-EDX), electron probe microanalysis (EPMA) and transmission electron microscopy (TEM) are used. The chemical composition of the samples is measured by spectral analysis. The characterization is done on the cross-sections of the casting and rolling direction, respectively.

The evolution of cementite particles in tempered martensite is studied by means of dilatometer experiments in a Baer dilatometer 805A/D. The dilatometer samples are post mortem investigated in TEM and the particles are analyzed by EDX and selected area electron diffraction (SAED).

The time-temperature profiles of the processing routes of the material are used to identify the cooling rates. With this information, the transformation temperatures from austenite to ferrite, bainite or martensite are either determined by calculations with software tools [39,40] or by the assessment of existing dilatometer curves. The precipitation kinetics are simulated based on these time-temperature profiles. The information about possible precipitating phases is taken from own investigations or from literature. Detailed information about chemical composition, time-temperature profiles and the experimental methods is given in each of the papers in part II of the thesis.

4. Through process modeling

This chapter describes the ideas behind the papers presented in part II [12-16] of the present work. Numerical simulations are additionally performed to explain in detail the developed routines and models given in the articles. Since we want to develop a ‘through process model’, the chapter is structured according to the production flow: casting, reheating and rolling and the final heat treatment and its effect on the materials properties. The applied models are described in the papers and are, therefore, not repeated here. However, there is one exception: the Scheil-Gulliver model is explained in the next section since this is not done in the papers.

The models are implemented in the thermokinetic software package MatCalc [17], in which the precipitate distribution is calculated based on nucleation and growth laws considering also the microstructural evolution of the material through processing such as, e.g., the evolution of the dislocation density and grain growth. The size-class oriented Kampmann-Wagner [41] approach is realized in the software, in combination with an extended classical nucleation theory for homogeneous and heterogeneous nucleation in multi-component systems [26-28]. The evolution equations for the radius and chemical composition of the precipitates are derived by utilizing the thermodynamic extremum principle [21-25]. Application examples of the software package can be found in e.g. refs. [42-46].

4.1 Scheil-Gulliver simulation

The Scheil-Gulliver model is applied for the calculation of the inhomogeneous as-cast chemical composition of the steels under consideration. In this chapter, the model is briefly reviewed and the application of the simulation for the prediction of primary carbides and for the precipitation kinetics in this chemically inhomogeneous matrix is presented.

The compositional change of the steel during solidification can be calculated by applying the Scheil-Gulliver model with full consideration of the redistribution of the fast diffusing interstitial elements, boron, carbon and nitrogen [47]. The sketch in fig. 4a shows an arbitrary phase diagram of a solidifying liquid with the initial composition c_0. At T_1, the alloy is slightly undercooled and a certain amount of solid is formed with the composition $c_{s,1}$. The residual liquid has the composition $c_{l,1}$ according to the lever rule. Since it is assumed that the substitional atoms are mostly immobile, the composition of the solid is frozen from that moment onwards. However, the fast diffusing interstitials B, C and N are further allowed to partition between liquid and solid phase until equilibrium is achieved. With further undercooling this process repeats, enriching the solid and the liquid phase with solutes. In reality, substitutional elements also have a finite mobility and, therefore, some potential to back-diffuse once some critical residual liquid fraction is reached; hence, the Scheil-Gulliver analysis must be terminated at some upper limit of segregation or minimum fraction residual liquid, respectively. The moment, when final solidification of the alloy occurs depends on the cooling rate: at high cooling rates, the residual liquid fraction can reach values up to 8% whereas, at low cooling rates, solidification can continue until residual liquid fractions of as low as 0.1% [47].

With increasing element concentration in the residual liquid, the precipitation of primary particles becomes possible as soon as the solubility limit corresponding to the enriched chemical composition is reached. The sketch in fig. 4b illustrates the dendritic microstructure with primary particles within the enriched residual liquid pockets.

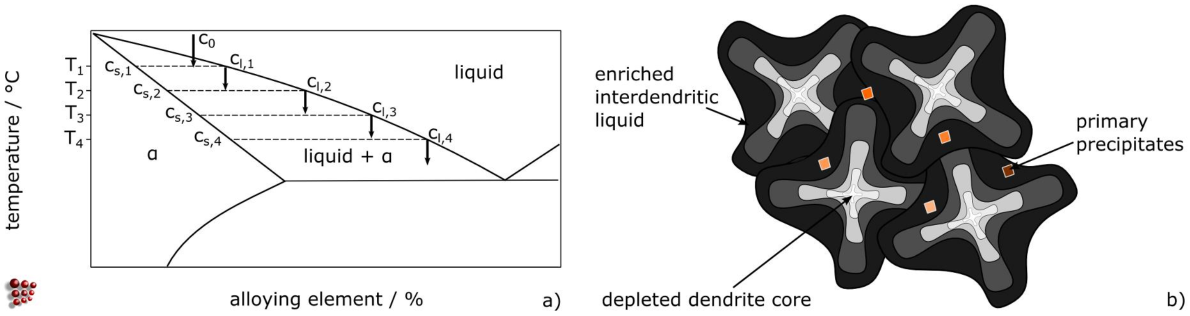

Figure 4: a) Arbitrary binary phase diagram indicating the change of chemical composition of the material during solidification. b) Sketch of dendrites with enriched interdendritic liquid and primary precipitates.

During solidification of the steel, we observe a peritectic reaction, where δ-ferrite plus liquid react to form austenite. This phase transformation is also considered in the Scheil-Gullivers simulations, which are described in the following chapter.

4.1.1 Prediction of primary particles

In the following two sections, the results of a Scheil-Gulliver simulation are discussed and it is shown how these results are further utilized for the analysis of the as-cast condition of a microalloyed steel with a nominal composition given in table 1.

First, the prediction of primary particles is analyzed. In fig. 5a, the phase fraction diagram corresponding to a Scheil-Gulliver simulation is plotted. The first crystal appearing in the system is δ-ferrite. At about 1485°C, liquid and δ-ferrite transform to liquid and austenite. The two dash-dotted lines in the plot mark the residual liquid fractions of 5% and 1%, respectively. These are the limits of interest for the subsequent analyses.

For the prediction of primary precipitates, 1% residual liquid fraction has shown to be a reasonable value [12]. Fig. 5a shows that, at this liquid fraction, three phases are predicted to be present in form of primary precipitates: MnS, TiN and NbC. It should be mentioned here that TiN and NbC are treated in this simulation as solid solution phases, due to the mutual miscibility for all microalloying elements and the interstitials C and N [32-38]. However, the calculated concentrations of C in TiN and N in NbC are low and, therefore, they are neglected in the present nomenclature of phases. The first paper in part II [12] summarizes the experimental data, which confirm these predictions.

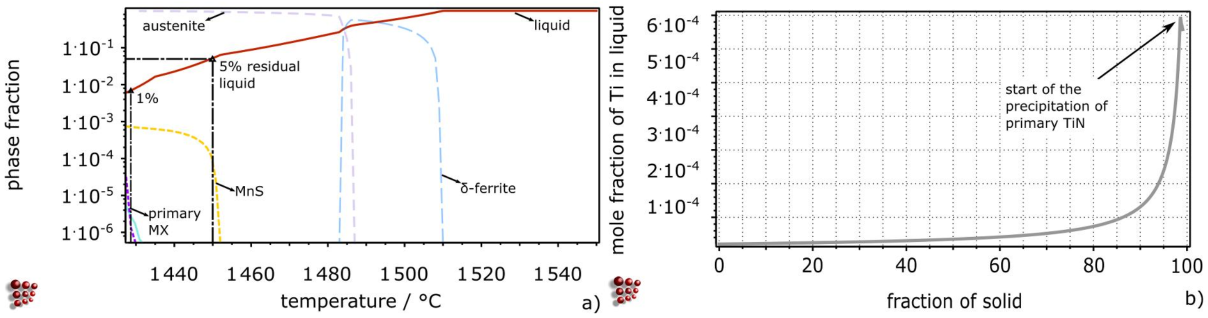

Figure 5: a) Result of the Scheil-Gulliver simulation: mole fraction of the phases vs. temperature (°C). The primary MX indicate TiN and NbC. b) Calculated Ti-enrichment in the residual liquid.

Fig. 5b displays the calculated Ti-enrichment of the liquid. The Ti-content in the residual liquid shows a steep increase at solid fractions higher than 80%. At about 1.5% liquid fraction, the Ti-content is above the solubility limit of the liquid and precipitation of primary Ti-particles commences. Due to the precipitation reaction, the Ti-concentration in the liquid drops again and, in the concentration curve, a peak is observed as illustrated in fig. 5b.

Due to the strong segregation behavior of Ti, the Ti-concentration is multiplied by a factor of ~30 in the given example. Although Ti is only a tramp element in this alloy, due to its segregation potential during solidification, primary Ti-precipitation is possible and experimentally observed: both, primary particles as well as secondary particles, are detected in samples of this alloy [12].

Finally, if the phase fraction of primary particles is high, the amount of alloying elements bound in their primary precipitates might reduce their concentration in the steel matrix significantly, since it is not expected that these particles dissolve again during further processing. This would lead to a change in precipitation kinetics of secondary particles. Consequently, to be able to predict the precipitation kinetics during processing of the material, the primary precipitates have to be considered correctly.

4.1.2 Precipitation kinetics of secondary particles in the as-cast condition

The considerations of the last section demonstrate that, in the as-cast condition, the material is of quite inhomogeneous chemical composition due to the segregation tendency of the alloying elements during solidification. In this chapter, this information is used for the calculation of the precipitation kinetics of particles in a material in the as-cast condition as presented in the paper [12] in part II. The difference in the precipitate distribution is shown using the nominal composition and the chemical composition of two extremes, which can be found in the as-cast structure of steel.

The steels under consideration solidify dendritically, which means that the first crystal formed from the liquid is solute depleted due to its lower solubility for most elements compared to the liquid. On the other hand, the last fraction of residual liquid, which finally solidifies, is a strongly solute enriched region. This inhomogeneity in the chemical composition is indicated in the sketch in fig. 4b. It is expected therefore that locally differing precipitation behavior is evident. In fact, we analyze a material, which might be comparable to a kind of compound: having in mind the dendritic structure, we face a solute depleted core region. Then, a first shell of solidified material is built around it with a chemical composition, slightly solute enriched. In a next step, a second shell is formed, more enriched in solute elements, and this process is continued until the most strongly enriched region, the interdendritic, residual melt, solidifies. The varying chemical composition of these shells is indicated in fig. 6 by the different shades of gray, where the Ti-content of the liquid phase is given and the Ti-content of the solid is illustrated. The nominal Ti-content of the material (see table 1 for the chemical composition in wt%) is marked as dash-dotted line in the plot. The step at around 70% fraction solidified is caused by the peritectic reaction.

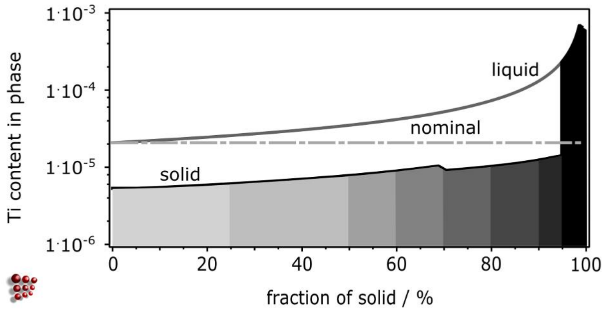

Figure 6: Calculated Ti-contents of the liquid and the solid phase. The different grey scales indicate the degree of the solute-element enrichment with decreasing liquid fraction.

For the paper in part II [12], two limiting extremes are considered: the solute-depleted dendrite core and the solute-enriched interdendritic region. Now, the comparison is shown between the results of the simulations considering these two limiting cases and the nominal composition for the precipitation kinetics of Ti-rich particles. In table 1, the nominal composition of the steel, the calculated chemical composition of the dendrite core and the interdendritic liquid are summarized.

The simulation setup is the same as described in the paper [12], with minor differences, which are labelled here. For the present simulations, the chemical composition of the first fcc crystal is taken into account as calculated by the Scheil-Gulliver simulation for the depleted dendrite core. The enriched region is read from the residual liquid at a liquid fraction of 5%. All data necessary for the simulation are given in table 2.

Table 1: Chemical composition for the simulation of the precipitation kinetics in the as-cast condition of a steel (wt%).

Condition	C	Si	Mn	S	Al	Ti	Nb	N
Nominal	0.22	0.24	1.24	0.025	0.025	0.0018	0.0356	0.0061
Depleted	0.07	0.16	0.87	0.000	0.027	0.0005	0.0076	0.0034
Enriched	0.63	0.68	2.89	0.359	0.019	0.0204	0.0452	0.0105

Table 2: Nucleation sites as defined in the simulation and the calculated temperatures, where 50% of ferrite has already formed [40].

Condition	Nucleation sites austenite	Nucleation sites ferrite	$\gamma \rightarrow \alpha$ transition
Nominal	Grain boundaries, dislocations	dislocations	710°C
Depleted	Dislocations	dislocations	730°C
Enriched	Grain boundaries, dislocations	dislocations	675°C

The plots in fig. 7 show the distribution plots of the TiN-populations, calculated on basis of the compositions given in table 1.

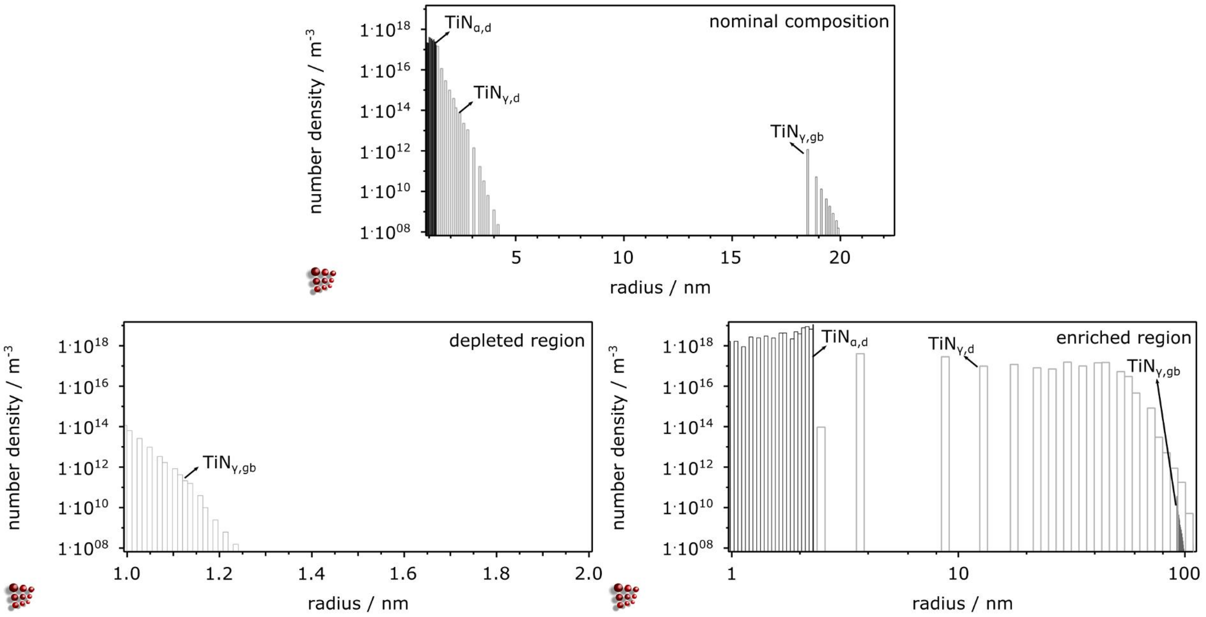

Figure 7: Calculated precipitate distribution plots of TiN-particles.

For estimation of the detectability of particles with TEM, we use a rule of thumb: the number density has to be higher than 10^{17} m^{-3} and the particles should have a mean radius of more than 1 nm. For the investigations with SEM, the number density might be lower, but the minimum radius should be larger than 50 nm to be able to find these precipitates. These limits should be kept in mind for the following discussion.

The simulations based on the nominal composition of the steel deliver a significant number of TiN precipitates at dislocations in ferrite, however, their maximum radius is smaller than 2 nm and, therefore, the probability of finding these particles in the experiment is rather small. Due to the small number density for the other two TiN-populations, it is not expected that they are detected with TEM.

For the depleted region, both, number density and particle size, are too small to be detected in the experiment. However, for the solute enriched region, we find particle sizes and number densities, which should be observed in the experiment and, indeed, Ti-rich particles are found in the TEM-analyses, with radii ~ 15 nm (fig. 8).

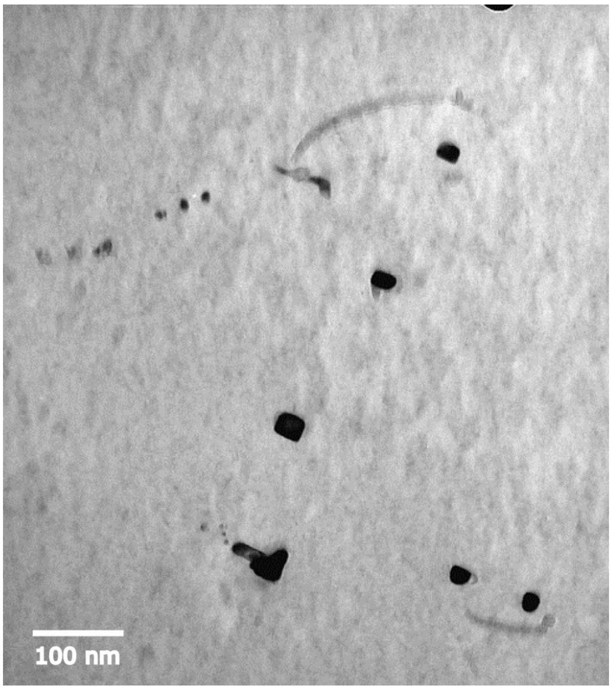

Figure 8: TEM bright field image of Ti-rich precipitates in the steel with the nominal composition given in table 1.

Of course, with regard to the plot in fig. 6, it is obvious that the strongly enriched regions make up only a small fraction of the microstructure. Consequently, if quantitative experimental analyses are performed and phase fractions are determined, the numerical results from the regions of different chemical compositions have to be weighted accordingly. Otherwise the contributing phase fractions from the enriched region would be too high, an example can be found in ref. [49].

The given example shows that, without consideration of the inhomogeneous chemical composition of the steel, the Ti-rich particles would not be predicted in a size and number density, which is observed in the experiment.

The technical papers [12,14] in part II of the thesis describe in detail the methodology how to apply the Scheil-Gulliver simulation for the analysis and prediction of primary precipitates and how they can be considered during further calculations of precipitation kinetics. The developed methodology is successfully applied for the analysis of industrially processed materials [49,50].

4.2 Precipitation kinetics in tempered martensite

The next step in the processing route after casting is reheating, rolling and the final heat treatment: quenching and tempering (Q&P). The subsequent section, compiles the main ideas of the papers [13-15], where the precipitation behavior during tempering of martensite is analyzed.

The materials under consideration are V-microalloyed [13,15] and Nb-Ti-microalloyed [14] steel grades. When starting the computational analysis of the precipitation behavior in the V-microalloyed steel grade, we observed that the calculated precipitate distribution of the cementite (Fe_3C) delivered an insufficient agreement with the experimental data. Moreover, the predicted V-particles and the M_7C_3-carbides did not correspond to the TEM-analysis.

At this point of the chapter, a short parenthesis is necessary, where the most important terms are briefly introduced, which are used when discussing cementite precipitation: In systems, Fe-C-X, with slow diffusing substitutional elements (X) and fast diffusing interstitial elements (C), it is generally accepted that phase transitions can be delineated by several different modes [51]:

i) Local equilibrium with full partitioning of all elements (ortho-equilibrium, OE)
ii) Negligible partitioning of substitutional elements and full partitioning of interstitials (NP-LE)
iii) No partitioning of substitutional elements and local equilibrium established only for the interstitial components (para-equilibrium, PE)
iv) A mixture of all modes, the mixed mode model [52]

With regard to the precipitation behavior during tempering of martensite, the analysis of TEM foils of the steel show that the Cr/Fe-ratio in the cementite particles differs to that of the matrix [13-15]. Up to these investigations, Fe_3C is usually considered in the simulation calculations with a para-equilibrium nucleus composition, where it is assumed that the solute/Fe-ratio is the same as in the matrix and C is the rate-determining element. Consequently, the precipitates nucleate rapidly and, after a short growth period, coarsening sets in, even before the annealing temperature of 690°C is reached. The computationally predicted particle size, therefore, is larger as experimentally observed. As a result, the cementite precipitates are calculated with the model according to the ortho-equilibrium to meet the experimental data. This change in the simulation set up leads to a good agreement at high annealing temperatures [13,14]. However, at lower temperatures, one has to switch again to the ‘para-equilibrium’ model to get an agreement between simulation and experiment. Due to these results, the model presented in paper four of part II [15] of the thesis is developed. In contrast to the descriptions, which are based on local equilibrium approaches, a model based on the thermodynamic extremal principle and a formulation of the precipitation problem in terms of mean-field quantities is applied. The nucleus composition is calculated according to the minimum nucleation barrier (min. G*) concept and the solute enrichment of the particles is considered by an enhancement of the solute diffusion coefficient inside the particles. The detailed description and the underlying formulae of the model are given in paper four in part II.

In the following section, the results of the simulations based on the ortho-, para- and the newly developed model are shown and discussed.

The plots in fig. 9 and fig. 10 illustrate the evolution of the Cr/Fe-ratio, the cementite mean radii and the number density. The point in time when nucleation happens is marked by the dashed lines. The onset of the coarsening stage is indicated by the symbols in the diagrams showing the mean radii and the number densities of cementite. The first plot in the columns shows the annealing temperatures, varying from 400°C to 700°C.

From the plots, which show the results for the PE calculations, it can be deduced that the rate-determining element for nucleation, growth and coarsening is C: the particles nucleate during quenching from austenitization temperature, followed by a very short growth stage and, during heating to the annealing temperature, coarsening starts. The coarsening rate increases with increasing annealing temperature. In contrast, if the nucleus composition is calculated according to OE, there is a significant delay of cementite nucleation at 400°C, which is reduced with increasing temperature. At the lower temperatures, the particles do not reach the coarsening stage during the heat treatment. Only at 700°C, coarsening is observed.

If we compare the Cr/Fe-ratio of cementite at the different temperatures, we see that the ratio in the cementite particles calculated according to the minimum nucleation barrier is similar to the PE calculations at low temperatures and short times and to the OE calculations at high temperatures at the end of the annealing temperature. Considering the size evolution of the particles, the plots in fig. 10b show that the coarsening rate decreases with increasing Cr-content in the phase.

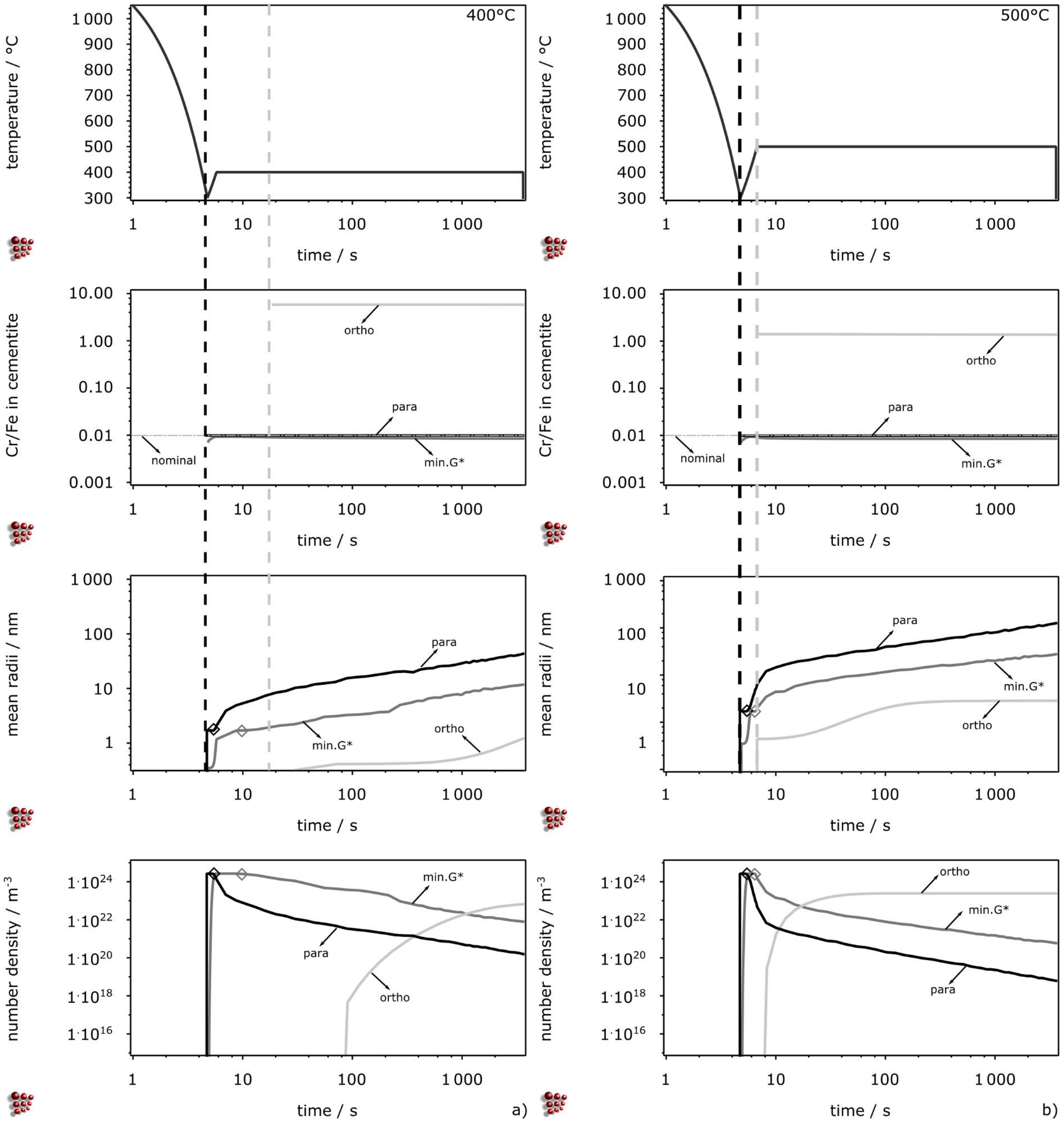

Fig. 9: Temperature profiles, Cr/Fe-ratios, mean radii and number densities of cementite particles calculated according to PE, OE and the min. G* [15]. a) 400°C and b) 500°C. The symbols indicate the onset of coarsening.

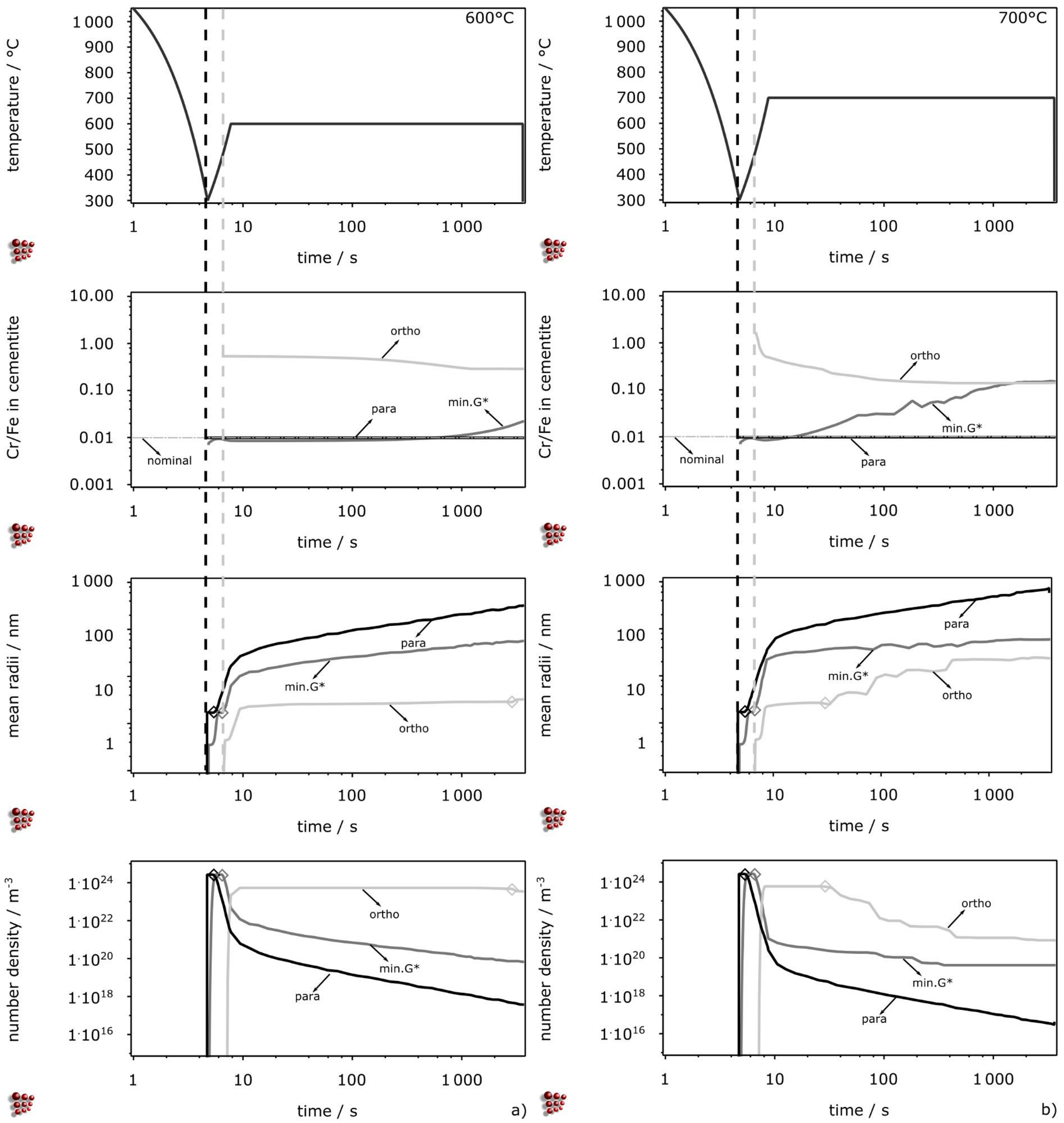

Figure 10: Temperature profiles, Cr/Fe-ratios, mean radii and number densities of cementite particles calculated according to PE, OE and the min. G* [15]. a) 600°C and b) 700°C. The symbols indicate the onset of coarsening.

The agreement between experiment and the calculations based on the new model is quite good as shown in paper four in part II. The model enables the calculation of the precipitation kinetics of cementite during tempering of martensite at temperatures higher than 300°C without changing the model for the nucleus composition. At lower temperatures, this concept might fail, since, at low temperatures, other mechanisms influence the cementite precipitation, such as C-trapping at dislocations or the precipitation of transition carbides or the tetragonal distortion of the bcc-lattice.

4.3 Simulation of the long-range diffusion of H in the presence of traps

Lastly, after the final heat treatment, the product, produced via continuous casting and hot rolling, is applied in service. The example considered here, is a sour gas application. In this case, the resistance against H-induced failure is one of the essential criteria for the materials performance. The fifth paper of the thesis deals with the long-range diffusion of H atoms in a Nb-microalloyed steel grade.

In this work, we investigated the H-charging and -discharging behavior of the material at room temperature in the presence of traps compared to the situation without active traps. The traps are defined as positions at the interfaces of the precipitates NbC, TiN and M_7C_3, which form during processing of the material. Parameter studies on the influence of the assigned trapping energy between H-atoms and precipitate interfaces on the H-diffusion and of the shape of the particles complement the analysis.

In this section, the influence of the H-concentration at the surface of the sample on the delay of the H-diffusion and the amount of free H in the sample is investigated. This is of special interest, since, in some experiments, like e.g. the electro-chemical permeation measurements in a Devanathan-Stachurski cell [53], which are often utilized to evaluate the 'trapping effect' of a material for H-atoms, do not deliver the information about the H-concentration at the sample surface [54].

For the analysis, the same simulation setup is used as in the paper [16]. NbC-particles are assumed to be the active traps with a binding energy of 37 kJ/mol. For better understanding, the simulation grid and the boundary conditions are given again in fig. 11. The H-concentration at the surface is varied from 1 ppm to 100 ppm.

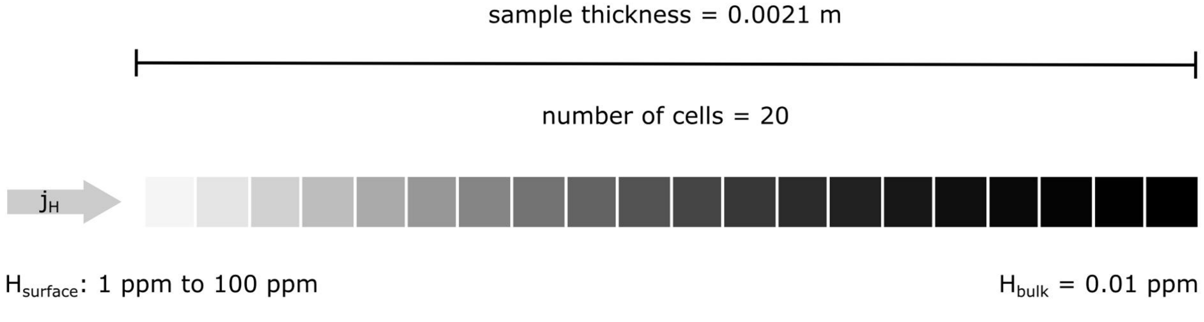

Figure 11: Simulation grid as defined for the H-diffusion simulations. The H-surface concentration is varied from 1 to 100 ppm.

The sketches in fig. 12 illustrate the loading situation in a sample in case of high and low H-surface concentrations. In the first case, the available traps in the sample are filled immediately and the excess H-atoms can diffuse more or less freely through the sample as if there were no traps at all. This is indicated by the size of the arrows for the H-flux into the sample and out of the sample (fig. 12a).

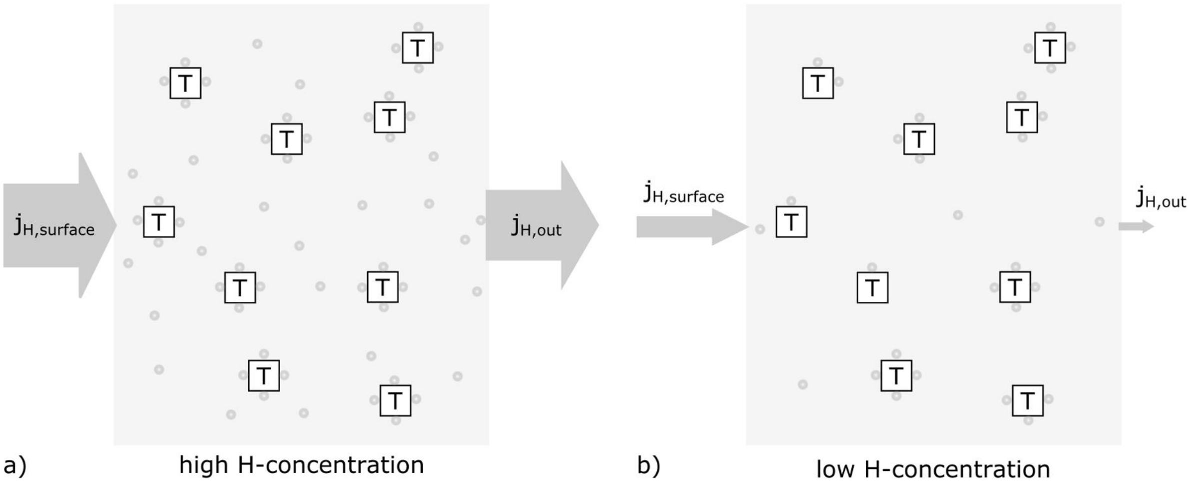

Figure 12: Sketch of the influence of a) high H-surface concentration and b) low H-surface concentration on the amount of free H-atoms in the lattice.

In fig. 12b, the same sample with the same trap density is depicted, but at a significantly lower H-concentration at the surface. H-atoms diffusing into the samples are efficiently trapped and there are still traps available. As a result, the amount of diffusible H is very low.

In this section, the results of the diffusion simulation with varying H-concentration at the surface are discussed. In the plot in fig. 13, the y-axis shows the amount of free H in the lattice as calculated for the outmost right cell of the diffusion sample (fig. 11) vs. time.

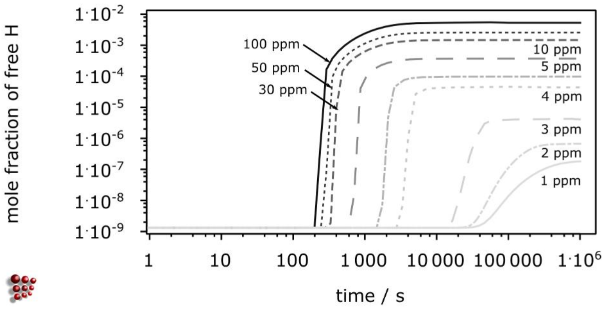

Figure 13: Results of the H-diffusion simulations with varying H-concentration at the surface. The mole fraction of the free H-atoms in the lattice is given on the y-axis vs. time. The results are shown for the outmost right cell of the diffusion sample.

The moment, where the H-curves increase, corresponds to the moment where H atoms leave the sample again. Of course, the lower the concentration at the surface is, the lower is the concentration at the end of the sample. But there is a significant delay in time, comparing the results for 100 ppm H and 1 ppm H.

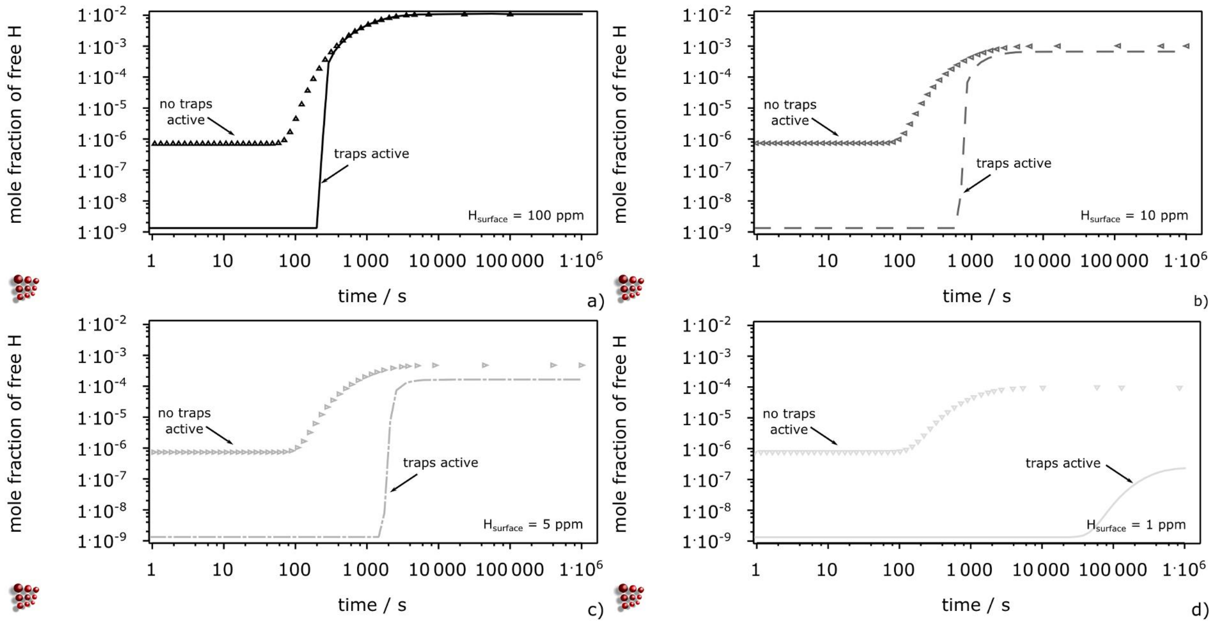

Figure 14: Variation of the H-surface concentration between 100 and 1 ppm H. The y-axes in the plots show the mole fraction of free H-atoms in the lattice without traps and with active traps vs. time. The results are shown for the outmost right cell of the diffusion sample.

Fig. 14a shows the results of the diffusion simulation with an H-surface concentration of 100 ppm with and without active traps in the material. At this high surface concentration, the available traps in the sample are filled within

~200 s. The amount of diffusible H-atoms reaches the total H concentration at the same time as if there were no traps active. With decreasing surface concentration, the delay in time for the effusion of H-atoms increases and the concentration of free H-atoms in the lattice does not reach the surface concentration anymore. The plot in fig. 14d) shows the situation for a low H-concentration of 1 ppm H (or a mole fraction of $5.5 \cdot 10^{-5}$) at the surface, the increase of the curve starts after ~ 40 000 s. The plateau value, a mole fraction of $1.9 . 10^{-7}$, is significantly lower than the total H concentration.

Considering now the experiment again, it might be speculated that the H-concentration in the experiment is high and the results lead to the interpretation that the long range diffusion of H-atoms is not hindered by any microstructural features. However, it is clearly shown by the simulation, that this interpretation is not correct, since the trapping effect is quite strong in case of low H-concentrations. From the experimental side of view, one might raise the question as to which H-concentration is comparable to the real situation, like e.g. the application in sour gas media. From the viewpoint of materials design, it should be considered how the diffusivity of H-atoms can be influenced and which alloying concept and processing route can improve the grain-boundary cohesion and toughness of the material to resist H-embrittlement.

In this case, the simulation fulfills its main task: it leads to a better understanding of the H-diffusivity kinetics in steel and to a proper interpretation of experimental results.

5. Summary & outlook

With the methodologies and models developed during this work, an approach has been developed by which it is possible to investigate precipitation kinetics during the industrial processes of casting, rolling and the final heat treatment for low alloyed steel in the carbon range of 0.20 to 0.35 wt% with microalloying additions of Nb, V and/or Ti. With the last study presented here, the investigation of the long-range diffusion of H in the presence of traps in steel, also the performance of the material in practical application can be investigated.

Although several important questions are answered by these analyses, there are still some open questions, which are part of ongoing research. For example, the consideration of inhomogeneous chemical composition in the as-cast condition. With the help of the diffusion-simulation feature implemented in MatCalc and presented in the last section, it is planned to define a diffusion sample with cells of differing chemical compositions and geometries simulating the dendritic microstructure, to investigate not only the difference in precipitation kinetics but also the element distribution during further processing.

The last section shows that the experiments applied for the evaluation of H-embrittlement of a material have to be interpreted with respect to the total H-concentration. With that information, materials design can be revised and adopted accordingly. On the other hand, it has to be considered, whether the experimental procedures reflect the application situation accordingly or whether setup should be adopted.

In any case, the present work aids in improvement of the understanding of the precipitation kinetics in industrially processed microalloyed steel and the findings can be further applied for the development of new alloys and process optimization.

6. References

[1] Lenard JG and Tajima M: Thermo-mechanical treatment of a high Nb high V bearing microalloyed steel, ISIJ Int. Vol. 35 Is. 12 (1995), 1509-1517

[2] Lopez HF, Bharadwaj R, Albarran JL, Martinez L: The role of heat treating on the sourgas resistance of an X-80 steel for oil and gas transport, Metall. Mater. Trans. A 34A (1999), 2419-2428

[3] Lopez Turconi G, Echaniz G, Cumino G, Anelli E, Scoppio L, Perez T and Morales C: Improvement of resistance to SSC initiation and propagation of high strength OCTG through microstructure and precipitation control, Corrosion Paper No. 01077 (2001)

[4] Klinkenberg C, Trute S and Bleck W: Niobium in engineering steels for automotive applications, Steel Res. Int. No. 9-10 (2006), 698-703

[5] Barani AA, Romano P, Li F, Ponge D and Raabe D: Design of high-strength steels by microalloying and thermomechanical treatment, Mater. Sci. Eng. A-463 (2007) 138-146

[6] Rassizadehghani J, Najafi H, Emamy M and Eslami-Saeen G: Mechanical properties of V-, Nb and Ti-bearing as-cast micralloyed steels, J. Mater. Sci. Technol. Vol. 23 Is. 6 (2007), 779-784

[7] Shanmugam S, Ramisetti NK, Misra RDK, Hartmann J and Jansto SG, Microstructure and high strength-toughness combination of a new 700MPa Nb-microalloyed pipeline steel, Mater. Sci. Eng. Vol. A478 (2008), 26-37

[8] Bréchet YJM, Hutchinson CR, Zurob HS and Sinclair CW: Effect of Nb on ferrite recrystallization and austenite decomposition in microalloyed steels, Steel Res. Int Vol 78 No. 3 (2007), 210-215

[9] Zajac S: Expanded use of vanadium in new generations of high strength steels, Materials Science and Technology (MS&T) (2006), 317-326

[10] Dong JX, Siciliano F Jr, Jonas JJ, Liu WJ and Essadiqi E: Effect of Silicon on the kinetics of Nb(C,N) precipitation during the hot working of Nb-bearing steels, ISIJ Int. Vol. 40 Is. 6 (2000), 613-618

[11] Perez M, Courtois E, Acevedo D, Epicier T and Maugis P: Precipitation of niobium carbonitrides in ferrite: chemical composition measurements and thermodynamic modelling, Phil. Mag. Lett. Vol. 87 Is 9 (2007), 645-656

[12] Zamberger S, Pudar M, Spiradek-Hahn K, Reischl M and Kozeschnik E: Numerical simulation of the evolution of primary and secondary Nb(CN), Ti(CN) and AlN in Nb-microalloyed steel during continuous casting, Int. J. Mat. Res. (formerly Z. Metallkd.) Vol. 103 Is. 6 (2012), 680-687

[13] Zamberger S and Kozeschnik E: Carbo-nitride precipitation in tempered martensite- computer simulation and experiment, Mat. Sci. Forum, Vols. 706-709 (2012), 1586-1591

[14] Zamberger S, Wojcik T, Klarner J, Klösch G, Schifferl H and Kozeschnik E: Computational and experimental analysis of carbo-nitride precipitation in tempered martensite, Steel Res. Int. Vol 84 No. 1 (2013), 20-30

[15] Zamberger S, Whitmore L, Krisam S, Wojcik T and Kozeschnik E: Experimental and computational study of cementite precipitation in tempered martensite, Modelling Simul. Mater. Sci. Eng. 23 (2015) 055012, 22pp

[16] Zamberger S, Lang P, Klösch G, Klarner J and Kozeschnik E: Long-range diffusion of H in the presence of traps in a microalloyed steel, Comput. Mater. Sci. doi:10.1016/j.commatsci.2015.11.014

[17] www.matcalc.at

[18] Svoboda J and Fischer FD, Modelling for hydrogen diffusion in metals with traps revisited, Acta Mater. 60/3 (2012) 1211-1220, doi:10.1016/j.actamat.2011.11.025

[18] Fischer FD, Svoboda J and Kozeschnik E, Interstitial diffusion in systems with multiple sorts of traps, Modelling Simul. Mater. Sci. Eng. 21/2 (2013) 025008/ 13p

[19] Svoboda J, Shan YV, Kozeschnik E and Fischer FD, Determination of depths of traps for interstitials from thermodynamic data: a new view on carbon trapping and diffusion, Modelling Simul. Mater. Sci. Eng.21/6 (2013) 065012/ 15p

[20] Onsager L, Reciprocal relations in irreversible processes I., Phys. Rev. I 37 (1931) 405-426
Onsager L, Reciprocal relations in irreversible processes II., Phys. Rev. II 38 (1931) 2265-2279

[21] Svoboda J, Fischer FD, Fratzl P and Kozeschnik E, Modelling of kinetics in multi-component multi-phase systems with spherical precipitates I: Theory, Mat. Sci. Eng.: A 385/1-2 (2004) 166-174

[22] Kozeschnik E, Svoboda J, Fratzl P and Fischer FD, Modelling of kinetics in multi-component multi-phase systems with spherical precipitates II: Numerical solution and application, Mat. Sci. Eng.: A 385/1-2 (2004) 157-165

[23] Kozeschnik E, Svoboda J and Fischer FD, Modified evolution equations for the precipitation kinetics of complex phases in multi-component systems, Calphad 28/4 (2004) 379-382

[24] Svoboda J, Turek I and Fischer FD, Application of the thermodynamic extremal principle to modeling of thermodynamic processes in material sciences, Phil. Mag. 85/31 (2005) 3699-3707

[25] Kozeschnik E, Svoboda J and Fischer FD, Shape factors in modeling of precipitation, Mater. Sci. Eng. A Vol. 441 (2006) 68-72

[26] Sonderegger B and Kozeschnik E, Generalized nearest-neighbor broken-bond analysis of randomly oriented coherent interfaces in multicomponent fcc and bcc structures, Metall. Mater. Trans. A 40A/3 (2009) 499-510

[27] Sonderegger B and Kozeschnik E, Size dependence of the interfacial energy in the generalized nearest-neighbor broken-bond approach, Scripta. Mater. 60/8 (2009) 635-638

[28] B. Sonderegger and E. Kozeschnik, Interfacial energy of diffuse phase boundaries in the generalized broken-bond approach, Metall. Mater. Trans. A 41/12 (2010) 3262-3269

[29] Sherstnev P, Lang P and Kozeschnik E: , Proc. Of 6th European Congress on Computational Methods in Applied Sciences and Engineering (Vienna, Austria) e-Book Full Papers [3-9503537-0-4] 5331-5338

[30] Großeiber S, Rath M and Kozeschnik E: Modeling of the interaction between precipitate formation and forming – a thermo-kinetic approach, Proc. Meform 2013 (2013) 69-78

[31] Sharma RC, Lakshmanan VK and Kirkaldy JS: Solubility of Niobium carbonitride in alloyed austenite and ferrite, Metall. Mater. Trans. A, Vol. 15A Is. 3 (1984), 545-553

[32] Okaguchi S and Hashimoto T: Characteristics of precipitates and mechanical properties in Ti beraring HSLA steels, ISIJ Int. Vol 27 (1987), 467-473

[33] Poths RM, Higginson RL and Palmiere EJ: Complex precipitation behaviour in a microalloyed plate steel, Scripta Mater. Vol. 44 (2001), 147-151

[34] Dutta B, Palmiere EJ and Sellars CM: Modelling the kinetics of strain induced precipitation in Nb microalloyed steels, Acta Mater. Vol. 49 Is. 5 (2001), 785-794

[35] Hong SG, Kang KB and Park CG: Strain-induced precipitation of NbC in Nb and Nb-Ti microalloyed steel, Scripta Mater. Vol. 46 Is. 2 (2002), 163-168

[36] Hong SG, Jun HJ, Kang KB and Park CG: Evolution of precipitates in the Nb-Ti-V microalloyed HSLA steels during reheating, Scripta Mater. Vol. 48 (2003), 1201-1206

[37] Pandit A, Murugaiyan A, Podder AS, Haldar A, Bhattacharjee D, Chandra S and Ray RK: Strain induced precipitation of complex carbonitrides in Bb-V and Ti-V microalloyed steels, Scripta Mater. Vol. 53 Is. 11 (2005), 1309-1314

[38] Saunders N, Guo, Z, Li X, Miodownik AP and Schillé J-Ph: Using JMatPro to model materials properties and behavior, JOM (2003) 12 60-5

[39] Dr. Sommer Werkstofftechnik: StahlWissen NvaiMat 15 Basis, Dr. Sommer Werkstofftechnik GmbH, www.werkstofftechnik.com

[40] Kampmann R and Wagner R, Decomposition of alloys, the early stages, Proc. of the 2nd Acta-Scripta Metallurgica Conf., Oxford, UK, 1984

[41] Sonderegger B, Kozeschnik E, Leitner H, Clemens H, Svoboda J and Fischer FD, Computational analysis of the precipitation kinetics in a complex tool steel, Int. J. Mat. Res. 99/4 (2008) 410-415

[42] Radis R, Schaffer M, Albu M, Kothleitner G, Pölt P and Kozeschnik E, Multimodal size distributions of γ' precipitates during continuous cooling of UDIMET 720 Li, Acta Mater. 57/19 (2009) 5739-5747

[43] Holzer I and Kozeschnik E, Simulation of Copper Precipitation in Fe-Cu Alloys, Mater. Sci. Forum 638-642 (2010) 2579-2584

[44] Radis R and Kozeschnik E, Kinetics of AlN precipitation in microalloyed steel, Modelling Simul. Mater. Sci. Eng. 18/5 (2010) 055003

[45] Pudar M, Zamberger S, Spiradek-Hahn K, Radis R and Kozeschnik E, Computational analysis of precipitation during continuous casting of microalloyed steel, Steel Res. Int. 81/5 (2010) 372-380

[46] Kozeschnik E, Rindler W and Buchmayr B: Scheil-Gulliver simulation with partial redistribution of fast diffusers and simultaneous solid-solid phase transformation, Int. J. Mat. Res. (formerly Z. Metallkd.) Vol. 98 Is. 9 (2007) 826-31

[47] Rindler W, Kozeschnik E and Buchmayr B: Computer simulation of the brittle-temperatur-range (BTR) for hot cracking in steels, Steel Res. Int. Vol. 71 No. 11 (2000) 460-466

[48] Radis R: Numerical simulation of the precipitation kinetics of nitrides and carbides in microalloyed steel, PHD-thesis, Faculty of Mechanical Engineering, Graz University of Technology (2010)

[49] Pudar M, Zamberger S, Spiradek-Hahn K, Radis R and Kozeschnik E: Computational analysis of precipitation during continuous casting of microalloyed steel, Steel Res. Int. Vol. 81, No. 5 (2010), 372-380

[50] Coates D E, Diffusional growth limitation and hardenability, Metall. Mater. Trans. A Vol. 4 Is. 10 (1973), 2313-2325

[51] Sietsma J and van der Zwaag S, A concise model for mixed-mode phase transformations in the solid state, Acta Mater. Vol. 52 (2004), 4143-4152

[52] Devanathan MAV and Stachurski Z, The adsorption and diffusion of electrolytic hydrogen in palladium, Proc. R. Soc. Lond. A Vol. 270 (1962), 90-102

[53] Svoboda J, Mori G, Prethaler A and Fischer FD, Determination of trapping parameters and the chemical diffusion coefficient from hydrogen permeation experiments, Corros. Sci. 82 (2014), 93-100

Part II

Scientific papers

S Zamberger

Contents part II

Paper one:

Paper two:

Paper three:

Paper four:

Paper five:

Paper one

Numerical simulation of the evolution of primary and secondary Nb(CN), Ti(C,N) and AlN in Nb-microalloyed steel during continuous casting

Zamberger S, Pudar M, Spiradek-Hahn K, Reischl M and Kozeschnik E

Int. J. Mat. Res. (formerly Z. Metallkd.) Vol. 103 Is. 6 (2012), 680-687

Numerical simulation of the evolution of primary and secondary Nb(CN), Ti(CN) and AlN in Nb-microalloyed steel during continuous casting

S Zamberger[1], M Pudar[2], K Spiradek-Hahn[3], M Reischl[1] and E Kozeschnik[4]

[1] voestalpine Stahl Donawitz GmbH, Kerpelystraße 199, 8700 Leoben, Austria

[2] MAGNA STEYR Fahrzeugtechnik AG & Co KG, Graz, Austria

[3] AIT Austrian Institute of Technology GmbH, Seibersdorf, Austria

[4] Christian Doppler Laboratory for „Early Stages of Precipitation”, Institute of Materials Science and Technology, Vienna University of Technology, Favoritenstraße 9-11, 1040 Vienna, Austria

Abstract. The precipitation of carbides and nitrides in Nb microalloyed steel is investigated experimentally and theoretically using light optical, scanning, and transmission electron microscopy, and the thermo kinetic software MatCalc. The simulations are based on a recently developed two-step methodology for precipitation simulation in primary solidification microstructures, where the compositional inhomogeneities from microsegregation are taken into account. The computed segregation is clearly evidenced in electron probe microanalyses of the as-cast microstructure. Based on the results of a Scheil –Gulliver simulation, precipitation kinetics simulations are performed with the chemical compositions corresponding either to the solute-rich interdendritic zone or the solute-depleted dendrite core zone. The predicted phase fractions, mean radii, number densities, and compositions of the precipitates are in good agreement with the experimental investigations.

1. Introduction

The knowledge of precipitation in microalloyed steel is essential, since it is well known that microalloying elements affect the hot ductility of continuously cast blooms and can lead to surface defects in the course of the straightening process [1 – 5].

In a previous study [6], the evolution of precipitates in a V-microalloyed steel grade has been investigated experimentally, using transmission electron microscopy (TEM), and computationally, using the thermo-kinetic software MatCalc [7,8]. A simulation methodology has been developed, which takes into account the local variations in chemical composition introduced by microsegregation during solidification. The approach is based on an analysis of segregated and depleted local regions utilizing the Scheil – Gulliver simulation technique [9 – 12]. Figure 1 shows a sketch of a primary solidification microstructure with segregated and depleted regions indicated by arrows, and former austenite grain boundaries, which are assumed to represent preferential nucleation sites for precipitates.

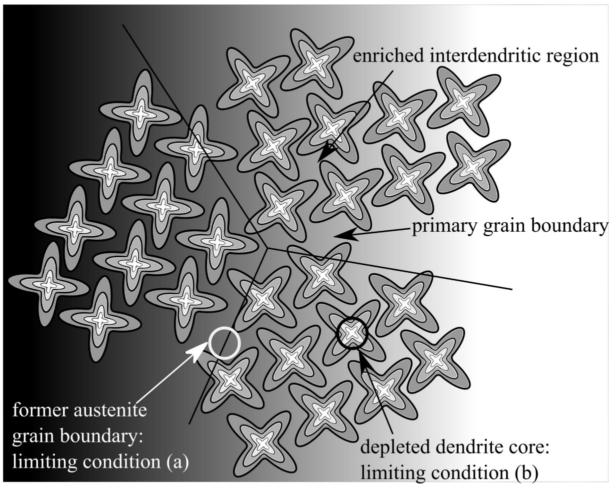

Figure 1: Sketch of the as-cast primary microstructure showing three differently oriented groups of dendrites. The primary austenite grain boundaries have slightly migrated from their original locations between the dendrite packets due to grain growth. The limiting conditions for the numerical simulations, (a) parts of the austenite grain boundary pass through the enriched interdendritic regions, and (b) the least favourable condition for precipitation, are also marked in the sketch.

In the present paper, we provide an extended investigation of another type of continuously cast microalloyed steel, mainly containing Nb. We start our analysis with the prediction and experimental verification of the coarse, primary precipitates, which form inside interdendritic residual liquid pockets, using the Scheil – Gulliver model described in Ref. [12]. Based on these results, precipitation kinetics simulations are carried out in order to describe the evolution of precipitates during the cooling process down to room temperature. For all simulations, the MatCalc software in version 5.41.0021 is used. Experimental verification is carried out with light-optical and scanning electron microscopy. Electron probe microanalysis (EPMA) is used for the description of the levels of microsegregation in the as-cast structure. The characterisation of the fine, secondary precipitates is performed with transmission electron microscopy (TEM).

2. Experimental

The nominal composition of the Nb-microalloyed line pipe steel used in the present investigation is summarised in table 1. The material has been continuously cast in a dimension with a diameter of 230 mm. The samples used for the microstructural characterisation are taken 10 mm below the bloom surface. For the EPMA, one sample is also taken from the bloom centre.

Table 1: Chemical composition (wt.%) of the investigated steel grade.

C	Si	Mn	S	Al	Ti	Nb	N
0.22	0.24	1.24	0.025	0.025	0.0018	0.0356	0.0061

The samples taken from the bloom in as-cast condition are analysed in a first step by optical light microscopy. The samples are ground, polished and etched with 3 % HNO_3. Further investigations on the type of precipitate phases visible in light optical microscopy are done with scanning electron microscopy (SEM). The chemical composition of the precipitates is determined by means of energy dispersive X-ray analysis (EDX). The degree of microsegregation is analysed with the help of electron probe microanalysis (EPMA), which is performed on a CAMECA SX-100 instrument equipped with five wavelength dispersive spectrometers. For transmission electron microscopy (TEM) and high resolution TEM (HRTEM), samples are cut into thin slices, which are subsequently electrolytically thinned. The analyses are carried out with a Philips CM20 STEM and a Tecnai F20 microscope operating at 200 kV and equipped with SE (secondary electrons), EDX, and EELS (electron energy loss spectroscopy) facilities. The precipitates are identified and characterised with selected area diffraction (SAD) and fast Fourier transformation (FFT) accompanied by analysis of the chemical composition with EDX.

3 Simulation methodology

3.1 Prediction of primary precipitates with the Scheil-Gulliver model

The Scheil – Gulliver model utilised in the analysis of primary precipitates and microsegregation has been described in detail in Ref. [12]. It is important to emphasise that these simulations are carried out by fully accounting for back-diffusion of interstitial elements and the peritectic solid – solid phase transformation, using the chemical composition given in table 1.

Our simulations indicate that primary precipitates form due to the high enrichment inside the residual liquid pockets. The threshold for final solidification in the Scheil – Gulliver simulation procedure is set at a residual liquid fraction between 1 and 5 %. The higher value for the threshold applies to rapid solidification conditions, whereas a lower value corresponds to slow cooling [12]. In the present work, the threshold is set to the value of 1 % residual liquid, which has also shown to be reasonable for the prediction of primary precipitates during continuous casting in the investigations described in Refs. [6, 11, 12].

3.2 Precipitation kinetics simulation

3.2.1 Treatment of microsegregation

For the precipitation kinetics simulations of secondary precipitates, the composition of the solute-rich interdendritic regions after final solidification can be reasonably well described by the chemical composition of the residual liquid at a threshold of 5 %, according to Refs. [6, 11]. This higher value accounts for the fact that there occurs some diffusional redistribution of enriched elements (back-diffusion) in the course of the slow cooling process during continuous casting, until the start temperatures of secondary precipitation are reached. This long-range diffusional redistribution will generally decrease the peak amount of segregation, which is indirectly taken into account by the higher threshold.

When performing kinetic simulations, the chemical composition of the solute-enriched and solute-depleted zones are evaluated at the residual liquid composition of 5 % and the composition of the first solid phase, bcc or fcc, directly below the liquidus temperature. The corresponding values are summarised in table 2.

Table 2: Predicted chemical composition (wt.%) of enriched and depleted regions.

zone	C	Si	Mn	S	Al	Ti	Nb	N
enriched	0.64	0.71	2.66	0.138	0.042	0.022	0.487	0.011
depleted	0.13	0.21	1.19	0.001	0.018	0.001	0.009	0.006

Due to the peritectic reaction occurring in the present steel grade, and austenite grain growth at higher temperatures, the prior (or former) austenite grain boundaries, as visible in micrographs, usually do not coincide with the primary grain boundaries originally located between the dendrite packets. Having this in mind, it has been suggested [6] that there exist two limiting cases with respect to the conditions for secondary precipitation: (a) The former austenite grain boundary passes through the enriched interdendritic regions. This represents the most favourable situation for precipitate nucleation, due to maximum available supersaturation and the presence of heterogeneous nucleation sites. (b) The depleted core of the dendrites in the absence of prior austenite grain boundaries, where only weak heterogeneous nucleation sites are available (dislocations). This represents the least favourable condition for precipitation.

The sketch in Fig. 1 illustrates these assumptions. The different grey scales of the dendrites indicate the degree of solute enrichment.

3.2.2 Simulation setup

The precipitation kinetics simulations are based on the temperature profile shown in fig. 2. This temperature profile is calculated with the help of an in-house model of the continuous casting process available at voestalpine company, and it corresponds roughly to the temperature at 10 mm distance from the bloom surface.

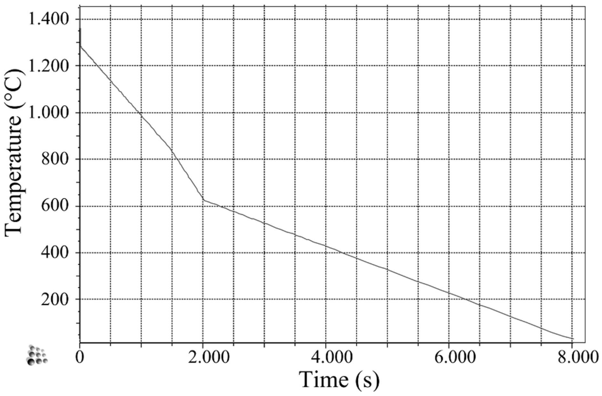

Figure 2: Calculated temperature profile which corresponds to the temperature at a distance of 10 mm from the bloom surface.

In the present work, experimentally determined mean grain sizes of 1200 µm for austenite and 10 µm for ferrite are used. Typical dislocation densities of 10^{-11} m^{-2} for undeformed austenite and 10^{-12} m^{-2} for ferrite are utilized [13].

Within the solute-enriched regions in austenite and ferrite, grain boundaries and dislocations are defined as potential nucleation sites. In the calculations for the depleted zone, only dislocations are allowed in austenite. In ferrite, again, both nucleation sites are assumed to be available. The major effect of the choice of nucleation sites is that it defines the number of potential nucleation sites when evaluating the nucleation rate [7]. For AlN precipitation, we also take into account the effective volumetric misfit, which is assumed to be different at dislocations and grain boundaries. See Ref. [14] for details on the simulation setup for AlN precipitation.

The precipitation kinetics simulations start at 1450 °C, which is the temperature where the threshold of 5 % residual liquid is reached. The austenite to ferrite transformation is determined based on the results delivered by the software package JMatPro [15]. Accordingly, the 50 % transformation temperature is evaluated with 625 °C and 790 °C for the enriched and the depleted zones, respectively. Above these temperatures, precipitation is assumed to take place within an austenitic matrix, below within a ferritic matrix.

4. Results

4.1 Experimental results

4.1.1 Characterisation of primary precipitates

The as-cast microstructure consists of ferrite, pearlite, and some bainite. Also, coarse primary precipitates are visible in the centre of the image in Fig. 3b, arranged in a ring-like structure.

Figure 4 presents a close-up and the corresponding EDX analyses of the primary precipitates typically found in the residual liquid pockets. The spectra clearly show that the precipitates are mainly Nb-carbides with traces of Ti, and MnS in between and at the top of this cluster.

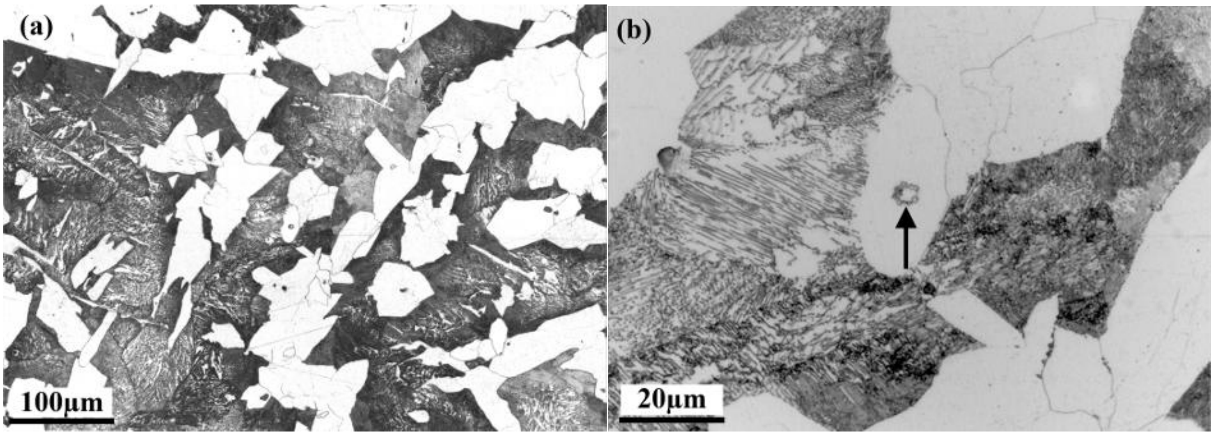

Figure 3: (a) Light optical micrograph of the as-cast microstructure consisting of ferrite, pearlite, and bainite. (b) Same as (a), but with higher resolution. In the centre, primary precipitates are visible arranged in a ring-like structure; etchant: 3 % HNO_3.

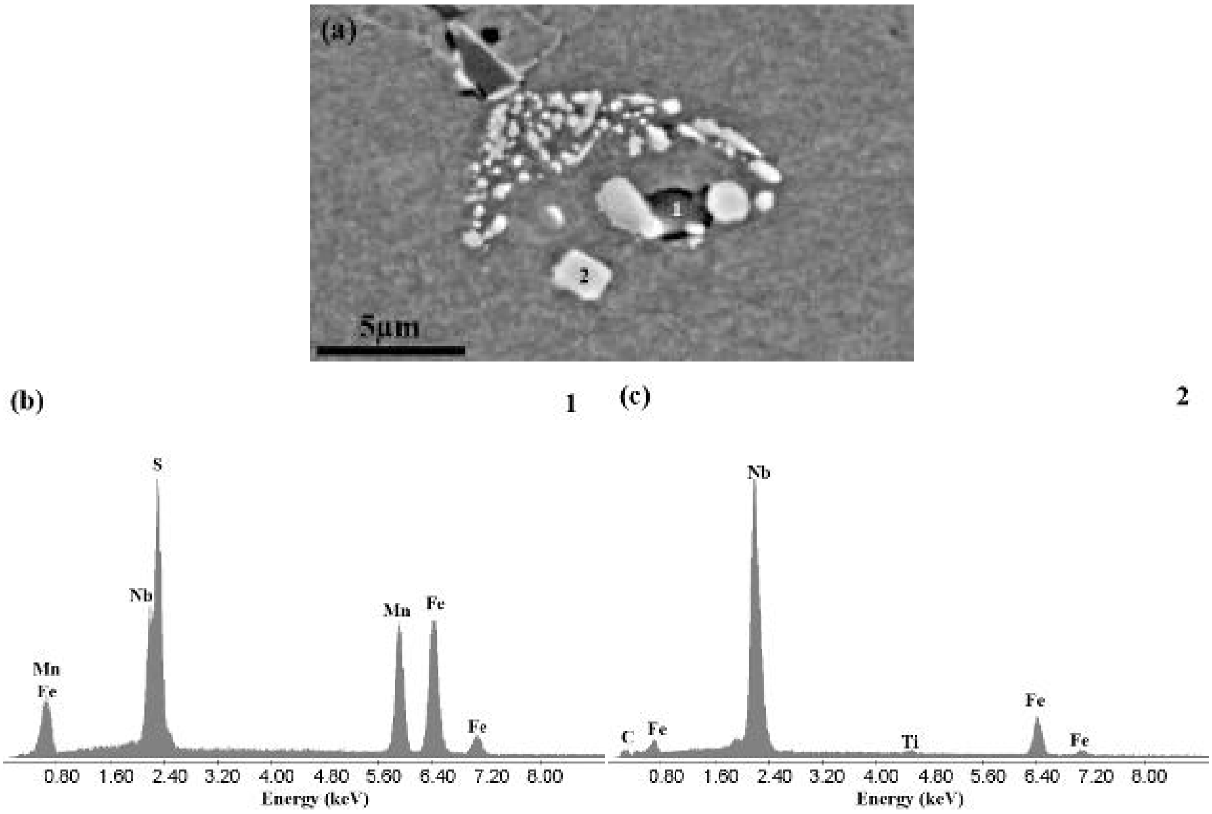

Figure 4: SEM micrograph of primary precipitates: the numbers 1 and 2 indicate the locations of the EDX spectra in (b) and (c).

The microsegregation levels of the as-cast structure of samples at the subsurface region and near the core of the bloom are investigated with EPMA. Figure 5 presents these results, clearly showing the enrichment in Mn and Nb.

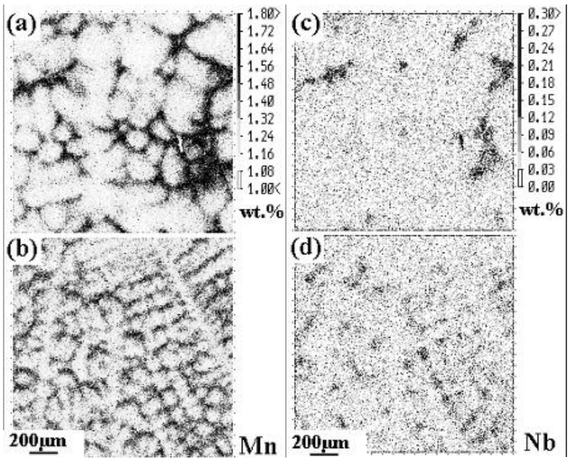

Figure 5: Mn and Nb elemental mapping of the as-cast structure; (a,c) samples are taken near the bloom centre and (b,d) near the subsurface region; the scale is the same for (a,b) as well as for (c,d).

4.1.2 Characterisation of secondary precipitates

Characterisation of the coarse, secondary precipitates is performed with SEM and EDX. Figure 6 shows a typical ferritic – pearlitic microstructure with numerous precipitates visible as bright spots. Several relatively large particles can be observed both within the ferrite as well as in the pearlite regions.

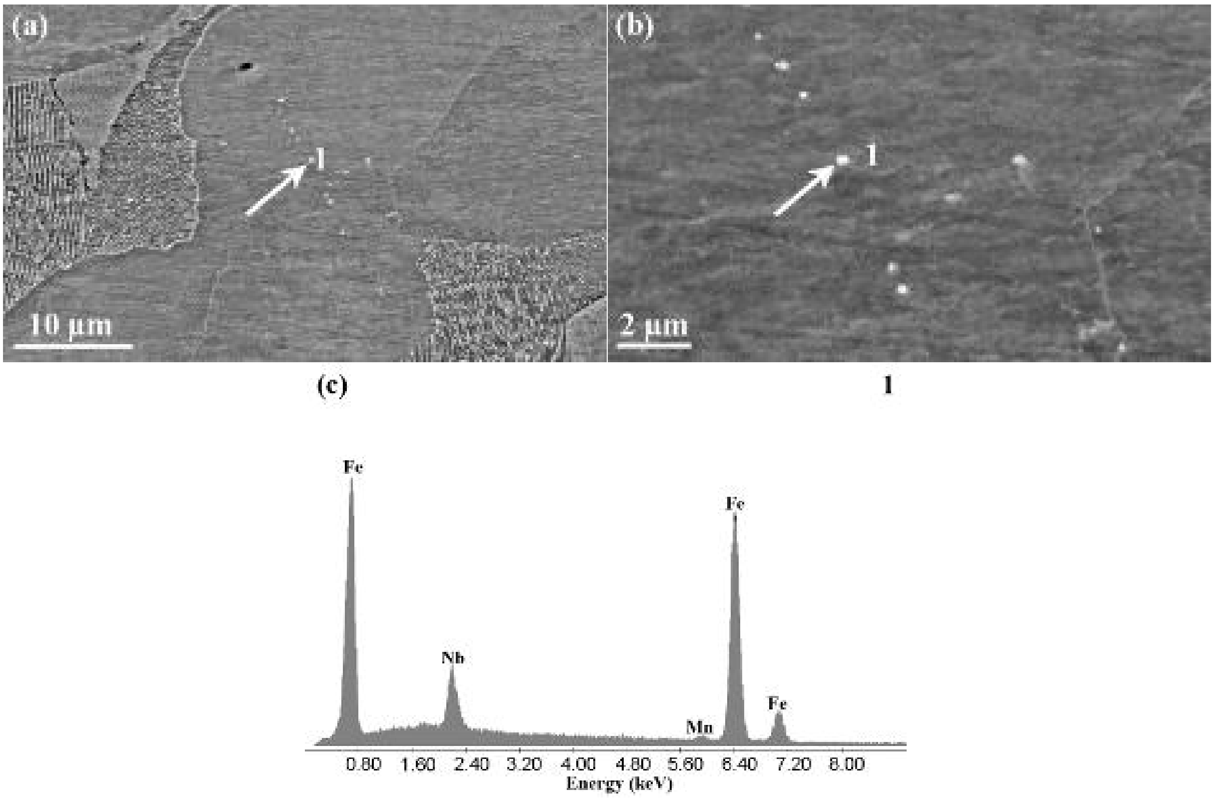

Figure 6: (a) SEM micrograph; (b) higher magnification of the region marked in (a) and (c) EDX spectra of the precipitate 1.

The precipitates in the centre of the image are clearly aligned, which we attribute to the fact that they have nucleated on some heterogeneous nucleation site, such as a former austenite grain boundary. After the transformation of the austenite matrix to ferrite and pearlite, the precipitates become located inside the ferrite grain. From the SEM image, the radius cannot be determined accurately, but the larger precipitates are in a size range between 50 to 250 nm in radius.

Figure 6b displays an enlargement of the supposedly prior austenite grain boundary precipitates. The corresponding EDX spectrum in fig. 6c shows a clear signal for Nb. The Fe and Mn peaks in this spectrum represent signals from the matrix. We therefore conclude that these precipitates are carbides, nitrides, or carbo-nitrides of Nb.

In addition, TEM and HRTEM analyses have been performed to characterise the fine secondary particles. The TEM images again show linearly aligned Nb-rich precipitates. We conclude that these precipitates have nucleated at heterogeneous nucleation sites, such as dislocations [16], as in the case of the precipitates in fig. 7a, or former austenite grain boundaries, as suggested for the precipitates shown in fig. 7b. Fine Nb-rich particles are also detected in the HRTEM analysis. The radii of the precipitates are found to be in the range of 10 to 15 nm if they are arranged along lines (fig. 7) and 2 to 10 nm if they are located within the grain.

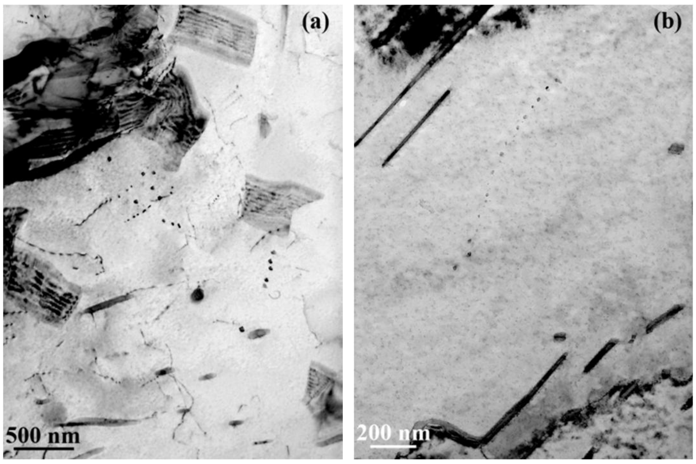

Figure 7: TEM bright-field image of Nb-rich precipitates nucleated at (a) dislocations and (b) at a former austenite grain boundary.

The observed Ti-containing precipitates have a radius of 10 to 15 nm and are often arranged linearly and can be clearly identified by their typical facetted morphology (fig. 8). Inside the grain, the Ti-containing particles are somewhat smaller with mean radii of about 5 nm.

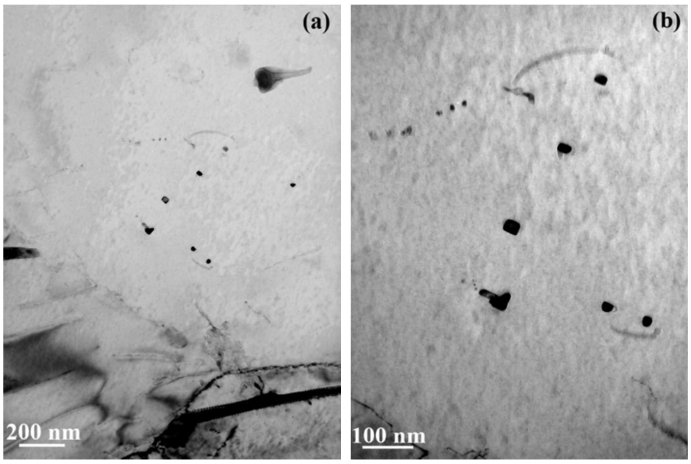

Figure 8: TEM bright-field image of (a) Ti-rich precipitates; (b) same position at higher magnification.

5. Results of the numerical simulations

5.1 Primary precipitates

With 1 % residual liquid taken as the threshold for final solidification, the simulation clearly reproduces the experimental observations described in the previous section. Both phases, a Nb-rich phase, which is referred to the MX-phase in fig. 9, and MnS are predicted to be present as primary precipitates, in accordance with the experimental results shown in fig. 4. From the simulations, we conclude that MnS precipitation occurs below a temperature of 1460 °C and primary Nb-rich precipitates form below 1435 °C. The 1 % residual liquid fraction threshold is reached at a temperature of 1433 °C. Experimentally, we also observe that the Nb-rich phase contains traces of Ti and N, therefore it may be concluded that this is (Nb,Ti)(C,N).

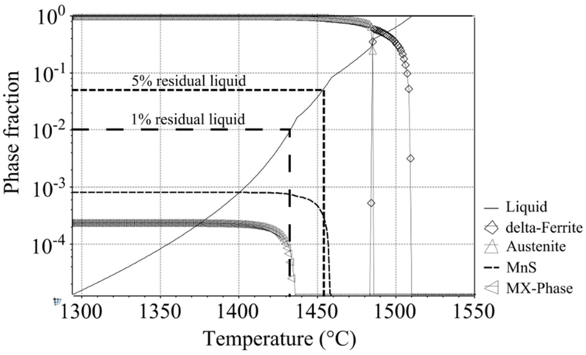

Figure 9: Phase fractions during solidification predicted by the Scheil – Gulliver simulation.

5.2 Precipitation kinetics within the solute-enriched zones

Fig. 10 depicts the assumed potential nucleation sites and summarises the predicted precipitation start temperatures, mean radii, and size distributions in austenite and ferrite.

The simulations indicate that precipitation starts almost immediately at 1450 °C with NbC both at the former austenite grain boundaries and at dislocations of austenite. TiN precipitation is predicted to start at around 1305 °C. Formation of AlN at the austenite grain boundaries sets in at around 890 °C.

At 625 °C, the precipitation domain (thermodynamic matrix phase) of the simulation is switched to ferrite. In this phase, the driving forces for precipitation are substantially higher compared to austenite, due to the low solubility of carbon in ferrite. Consequently, nucleation of new AlN and NbC particles sets in almost instantaneously at grain boundaries and, for AlN, also at dislocations.

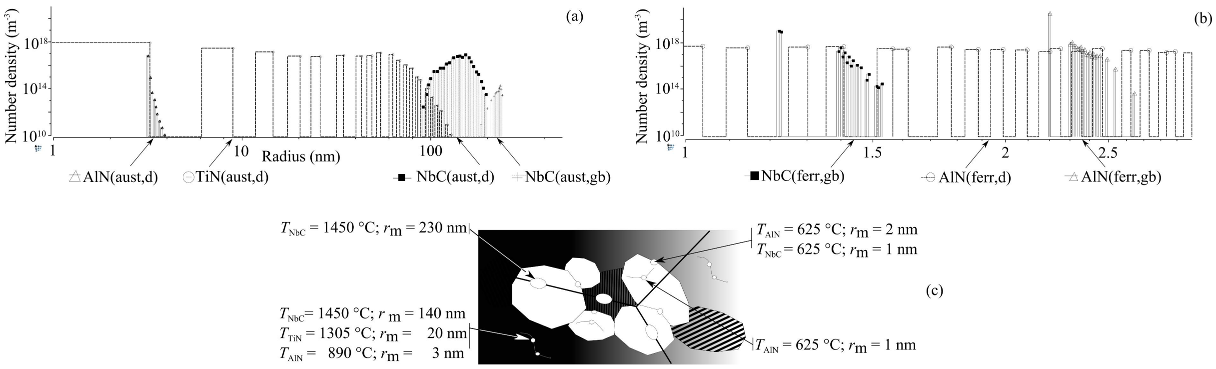

Figure 10: Calculated precipitate distribution for the solute-enriched interdendritic zone in (a) austenite and (b) ferrite. The sketch in (c) indicates the nucleation sites of the precipitates as well as their precipitation start temperature and their mean radii.

5.3 Precipitation kinetics within the solute-depleted zone

Figure 11 presents the results of the kinetic simulation, again, based on the temperature profile of fig. 2. In austenite, TiN and NbC are predicted to form, starting at approximately 1045 °C and 910 °C, respectively. Compared to the results of the solute-enriched interdendritic regions, we find that the precipitation start temperatures are lower and both, the number density as well as the size of the precipitates, are significantly smaller. This effect is simply ascribed to the reduced chemical driving forces for precipitation as a result of the lower solute content.

Below 790 °C, when precipitation is assumed to occur in ferrite, even within the solute-depleted dendrite core region, the driving forces are high enough for immediate nucleation of all possible precipitates.

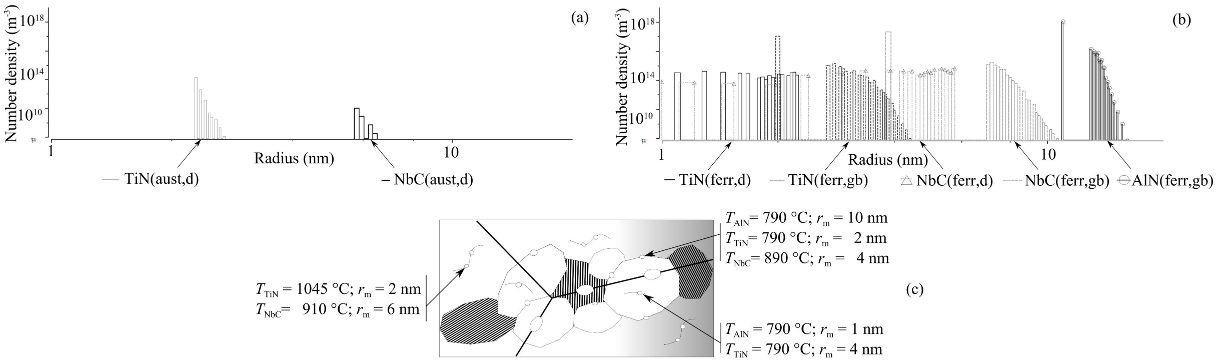

Figure 11: Calculated precipitate distribution for the solute-depleted dendrite core zone in (a) austenite and (b) ferrite. The sketch in (c) indicates the nucleation sites of the precipitates as well as their precipitation start temperature and their mean radii.

6. Discussion

When comparing the computer simulations with the experimental investigations, we have to be aware of the limitations of both. From the computational side, it should be kept in mind that the precipitate distributions shall not directly be compared with any real distribution, since the computations are carried out under the ideal situation that the local microstructural environment is identical for each single precipitate. In reality, this idealization does not apply. Moreover, we have carried out the simulation with a limited set of possible precipitate compositions, mainly in order to facilitate interpretation. Although the size distribution should therefore be looked at critically, the two precipitate parameters that should carry sufficient significance to allow for a comparison with experiment are the mean radius and the number density.

In the microscopic characterisation, we are limited by the applied techniques. For instance, in SEM, we are capable of scanning a rather large section of the sample; however, we are restricted to the identification of precipitates above a certain size. This is usually in the range of 100 nm and more. In TEM and HRTEM, limitations arise from the restricted volume of inspection per sample and the high amount of experimental effort. As a rule of thumb, we therefore claim that smaller precipitates can only be detected with a reasonably high probability if their number density exceeds approximately 10^{17} m^{-3}. Moreover, even if they appear in sufficiently high number density, they should have reached a size of at least 2 – 3 nm, otherwise there is also a good chance that they will not be detected in TEM. In SEM, the critical number density for observation of large enough precipitates can be considerably lower, since the area of inspection is orders of magnitude larger.

In tables 3 and 4, the results of the kinetic simulations based on the chemical composition of the solute-enriched and solute-depleted regions are compared to the experimentally observed precipitates. With the applied experimental techniques, it is difficult to clearly identify the nucleation sites of the precipitates, as it is done in the simulations. This is why we do not differentiate between the nucleation sites in the column for the observed particles. However, the arrangement of the Nb-rich precipitates in fig. 6, for example, at least suggests that these particles have nucleated at the former austenite grain boundaries or along dislocations. Although it is not possible to determine their radii accurately from the SEM image, for the enriched zone, the predicted and the observed particle sizes agree reasonably well. The experimentally observed radii of the Ti-rich precipitates is in the range of 10 to 15 nm when they are aligned linearly, and about 5 nm inside the grain, also in accordance with the numerical results.

From the spatial arrangement of the Nb-rich precipitates and from their size, which is shown in fig. 7a, we conclude that these particles have probably nucleated on dislocations. These particles have a radius of about 10 to 15 nm, which corresponds quite well to the numerical predictions for NbC at dislocations in the depleted core zone.

The precipitates shown in the TEM images in fig. 7b show a similar linear alignment as the precipitates in Fig. 6, their radii are considerably smaller in the range of 8 and 15 nm, though. This is not in accordance with our predictions. However, it should be pointed out here that the two chemical compositions used for the description of the segregated as-cast structure represent limiting cases. Therefore, it is plausible to assume that these precipitates could have formed at the former austenite grain boundaries in a medium segregated region, which lies in between the two considered limiting cases.

For the numerical analysis of AlN precipitation, we observe some discrepancy to the experimentally found particles. The radius and, in particular, the number densities of these precipitates show some deviation from the calculation. We assume that a considerable part of this discrepancy comes from the fact that AlN particles at grain boundaries are extremely difficult to observe in TEM due to their weak contrast. Furthermore, the ferrite grain boundaries are moving in the course of the transformation, which probably makes precipitation at ferrite grain boundaries more difficult than at static boundaries.

In our simulations, we have defined TiN and NbC as separately precipitating phases. We emphasise, however, that the Ti-rich particles often contain considerable amounts of Nb and vice versa. We have not taken this into account, since interpretation of simulation results including complex carbonitrides can be rather involved. Preliminary simulations have indicated that the basic precipitation characteristics of the system do not change significantly, if the complex precipitates are substituted by precipitates with idealised, simplified compositions.

Table 3: Results of the numerical simulations of the enriched interdendritic zone compared to the experimentally observed particles. γ austenitic matrix phase; α ferritic matrix phase; r_{mean} mean radii; NS nucleation site; r_{exp} experimentally observed radii.

Matrix	Phase	NS	r_{mean} (nm)	No. Density (m^{-3})	Predicted	Observed	r_{exp} (nm)
γ	AlN	gb	88	2×10^{11}	yes	no	-
	AlN	d	3	4×10^{16}			
	TiN	gb	73	3×10^{11}	yes	no	-
	TiN	d	21	1×10^{18}			
	NbC	gb	230	1×10^{15}	yes	yes	50 – 250
	NbC	d	143	4×10^{17}			
α	AlN	gb	2	4×10^{20}	yes	no	-
	AlN	d	1	8×10^{18}			
	TiN	gb	< 1	2×10^{20}	yes	yes	2 – 15
	TiN	d	< 1	1×10^{17}			
	NbC	gb	1	2×10^{19}	yes	yes	2 – 15
	NbC	d	< 1	3×10^{14}			

Table 4: Results of the numerical simulations of the depleted dendrite core zone compared to the experimentally observed particles. γ austenitic matrix phase; α ferritic matrix phase; r_{mean} mean radii; NS nucleation site; r_{exp} experimentally observed radii.

Matrix	Phase	NS	r_{mean} (nm)	No. Density (m^{-3})	Predicted	Observed	r_{exp} (nm)
γ	TiN	d	2	1×10^{18}	yes	no	-
	NbC	d	6	1×10^{14}	yes	no	-
α	AlN	gb	11	6×10^{19}	yes	yes	~ 15
	AlN	d	< 1	1×10^{14}			
	TiN	gb	2	1×10^{19}	yes	yes	~ 5
	TiN	d	1	6×10^{17}			
	NbC	gb	4	2×10^{19}	yes	yes	2 – 15
	NbC	d	4	8×10^{17}			

7. Summary and conclusions

The precipitation of carbides and nitrides in Nb-microalloyed line pipe steel has been investigated using light optical, scanning, and transmission electron microscopy, together with thermo-kinetic computer simulations. The simulations are based on a recently developed two-step methodology for precipitation simulation in primary solidification microstructures, where inhomogeneities from microsegregation can be taken into account. Based on the results of a Scheil – Gulliver simulation, precipitation kinetics simulations are performed for the chemical compositions corresponding either to the solute-rich interdendritic zone or the solute-depleted dendrite core region. These situations represent the limiting cases of favourable and non-favourable conditions for precipitation in cast material.

Comparison between the experimentally observed and the predicted precipitates shows good agreement. The primary precipitates, MnS and Nb-rich carbonitrides, which are predicted by a Scheil – Gulliver simulation, are also observed in accordance with the results of the microstructural characterisation.

The proposed methodology thus represents a suitable means for estimating primary and secondary precipitation during continuous casting from the liquid to the solid state.

8. References

[1] B. Mintz, J.M. Stewart, D.N. Crowther: Transactions ISIJ 27 (1987) 959.

[2] P. Sricharoenchai, C. Nagasaki , J. Kihara: ISIJ International 32 (1992)1102.

[3] B. Mintz: ISIJ International 39 (1999). 833.

[4] L. E. Cepeda, J. M. Rodriguez Ibabe, J. J. Urcola: ISIJ International 33 (1993)799.

[5] G. Cardoso, S. Yue: Proc. Mechanical Working and Steel Processing (1989) 585.

[6] M. Pudar, S. Zamberger, K. Spiradek-Hahn, R. Radis, E. Kozeschnik: Steel Res. Int. 81 (2010) 372.

[7] J. Svoboda, R.D. Fischer, P. Fratzl, E. Kozeschnik: Mater. Sci. Eng. A 385 (2004) 166.

[8] E. Kozeschnik, J. Svoboda, P. Fratzl, F.D. Fischer: Mater. Sci. Eng. A 385 (2004) 157.

[9] E. Scheil: Z. Metallkd. 34 (1942) 70.

[10] G.H. Gulliver: J. Inst. Met. 9 (1913) 120.

[11] W. Rindler, E. Kozeschnik, B. Buchmayr: Steel Res. Int. 71 (2000) 460.

[12] E. Kozeschnik, W. Rindler, B. Buchmayr: Int. J. Mat. Res. 98 (2007) 826.

[13] D. Hull, D.J. Bacon: Introduction to dislocations, Pergamon Press, Ltd. Oxford, UK (1984).

[14] R. Radis, E. Kozeschnik: Model. Sim. Mater. Sci. Eng., 18 (2010) 055003.

[15] N. Saunders, N. Guo, X. Li, A. P. Miodovnik, J.-Ph. Schille: JOM 12 (2003) 60.

[16] D.A. Porter, K.E. Easterling: “Phase Transformations in Metals and Alloys”, 2nd Ed., CRC Press, Boca Raton, FL (2004)

Paper two

Carbo-nitride Precipitation in Tempered Martensite – Computer Simulation and Experiment

Zamberger S and Kozeschnik E

Int. Mat. Sci. Forum, Vols. 706-709
(2012), 1586-1591

Carbo-nitride Precipitation in Tempered Martensite – Computer Simulation and Experiment

S Zamberger[1] and E Kozeschnik[2]

[1] voestalpine Stahl Donawitz GmbH, Kerpelystraße 199, 8700 Leoben, Austria

[2] Christian Doppler Laboratory for „Early Stages of Precipitation”, Institute of Materials Science and Technology, Vienna University of Technology, Favoritenstraße 9-11, 1040 Vienna, Austria

Abstract. In the present work, the precipitation behavior of a V-microalloyed, quenched and tempered steel with 0.3wt% C is investigated experimentally and by computer simulation. The specimens are analyzed by means of transmission electron microscopy using selected area diffraction (SAD) and energy dispersive x-ray spectroscopy (EDX). The analysis is done on electro polished foils and on extraction replica. The numerical simulation is performed with the thermo kinetic software package MatCalc, where the precipitation kinetics is examined for the experimentally applied thermo-mechanical cycles. Good agreement between experiment and simulation is obtained and the experimentally observed precipitate microstructure can be well explained on the basis of these simulations.

1. Introduction

In industrial materials development, the prediction of phase transformations and evolution of precipitates during the different stages of processing are gaining in importance. In the present case, a quenched and tempered (Q&T) line pipe steel is investigated, which is typically used in sour service applications. The sulfide stress cracking performance depends directly on the microstructure of the steels. One of the key factors determining the resistance against sulfide stress cracking is the type of carbide and nitride precipitation occurring in the production process. The present paper reviews typical precipitation reactions in comparable steel grades and describes the basic features of the model that is applied here for the numerical simulation of these reactions. This paper is mainly focused on the description of the modeling strategy for the precipitation kinetics during a complex heat treatment based on the industrial processes of hot rolling and subsequent Q&T treatment.

2. State of the art

2.1 Experimental

Tempering of martensite is utilized to adjust the mechanical properties of Q&T steel according to its application requirements. It is generally agreed that it proceeds in four stages, where the carbon segregation or clustering at lattice defects is sometimes referred to as the zeroth stage of tempering [1].

Since stage I, the precipitation of ε-carbides, and stage II, the decomposition of retained austenite, are not focus of this work, the description of tempering starts with the precipitation of cementite (Fe_3C, orthorhombic) at temperatures between 250° and 700°C (stage III). The nucleation sites are frequently martensite lath boundaries at low temperatures and recrystallized ferrite grain boundaries at higher temperatures. If carbide-forming elements such as Ti, Mo or V are added to the steel, at temperatures above 500°C (stage IV), the precipitation of fine alloy carbides occur. These carbides, like TiC, V_4C_3 or Mo_2C replace some of the coarse cementite. Dislocations inherited from martensite are primarily their nucleation sites. The addition of Cr stimulates coarse M_7C_3 precipitates with orthorhombic structure [1].

Lee and Su [2] have investigated a steel grade with a chemical composition comparable to the present steel. These authors found that, at tempering temperatures above 650°C, M_7C_3 carbides precipitate simultaneously with the partial dissolution of cementite within the matrix.

The effect of alloying elements on cementite precipitation and growth was investigated by several authors. In refs. [3,4], e.g., it is shown that the coarsening of cementite is retarded by the addition of alloying elements and the replacement of cementite by alloy carbides is easier. Shaw and Quarrell [5] claim that, in an alloy with 0.19wt% C and 1.08wt% Cr, the ratio between M_3C and M_7C_3 was 70 : 30 after tempering at 700°C. Airey et al. [6] observe that no extra X-ray diffraction lines can be observed and they suggest that the precipitates in a steel with 0.15wt% C and 1.12wt% Cr are $(Fe,Cr)_3C$. Woodhead and Quarrell [7] mentioned that, in steels containing between 1wt% and 4wt% Cr and lower vanadium contents, V prefers to appear in M_7C_3 rather than in M_3C carbides. In steel with low concentration of alloying elements, Thomson [8] suggests that the alloying elements either go into solid solution in the matrix or into cementite, rather than precipitating as an own carbide population. M_7C_3 is a Cr-rich carbide with a solubility for Fe up to 60%. Also, elements such as Mn, V and Mo can dissolve into this carbide. In identifying the type of carbide, due to the presence of extensive stacking faults in planes perpendicular to the basal plane of M_7C_3-

carbides, the electron diffraction patterns show characteristic streaks, which make it easy to identify them [8,9].

Further precipitates in comparable steels are M_2C, a Mo-rich carbide with a significant solubility for Cr and V. Fe is soluble in M_2C too, though to a smaller extent. Finally, MC-type fcc carbides and nitrides represent the most stable type of precipitates, typically rich in Ti, Nb, and V [8].

2.2 Simulation

Modeling of precipitation is often based on the numerical Kampmann Wagner model [10], compare, for instance, refs. [11,12]. In the present work, a similar approach based on the SFFK-model (Svoboda-Fischer-Fratzl-Kozeschnik-model) [13] is used, which is implemented in the thermo-kinetic software package MatCalc [14,15]. It is based on the application of the Onsager extremum principle within a mean field approach, which makes it possible to account for the complexity of multi-component multi-phase materials and the most important features of the real microstructure.

3. Experimental

3.1 Material

The material under investigation is an industrially processed linepipe steel, which was produced by continuous casting. After reheating and hot rolling of seamless pipes, the material was austenitized at 880°C, and quenched and tempered at 690°C. The chemical composition is given in table 1. The temperature profile of this process is shown in fig. 1.

Table 1: Chemical composition of the investigated steel in wt%.

C	Si	Mn	Cr	Mo	V	Al	N
0.31	0.24	0.29	0.94	0.78	0.075	0.0375	0.0147

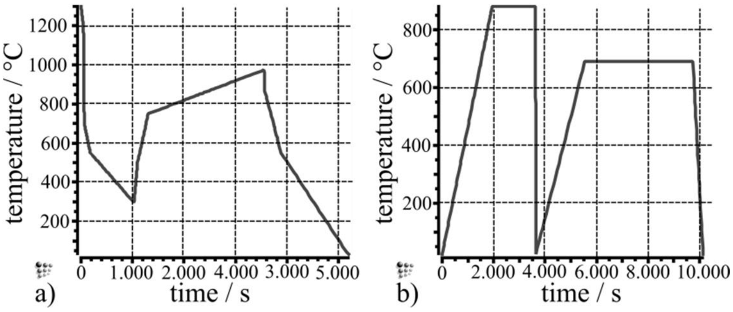

Figure 1: Temperature profile of the industrial processes of hot rolling (a) and Q&T treatment (b).

3.2 Experimental

Samples for the TEM-analysis are prepared either as electro-polished foils or carbon extraction replica. The investigations are performed on a FEI TECNAI F20 operating at 200kV equipped with EDX and EELS (electron energy loss spectroscopy) facilities. The chemical composition of the precipitates is determined by EDX-analysis and phases are identified by electron diffraction.

The main types of precipitates, which are observed are precipitates at martensite lath boundaries, accumulations of cigar-shaped precipitates, smaller spherical particles and fine precipitates with radii < 15 nm within the martensite laths (see Fig. 2 a to c). Due to the complex structure of tempered martensite, it is difficult to identify former austenite grain boundaries in TEM. Still, we observe a few particles, which seem to be nucleated at austenite grain boundaries.

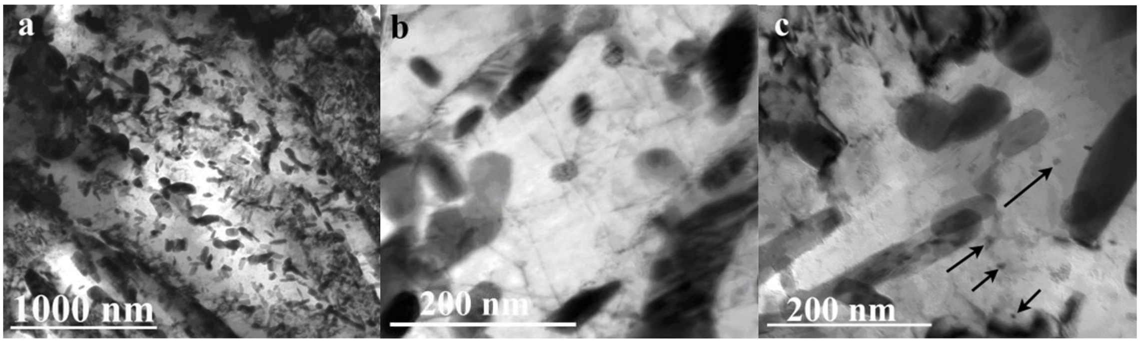

Figure 2: TEM-bright field images of electro-polished foils showing the different types and sizes of the precipitates.

With electron diffraction, it was possible to differentiate between two phases with similar chemical composition. M_7C_3, has a diffraction pattern showing the typical streaks as mentioned above, whereas M_3C has not. Unfortunately, it was not possible to identify the fine precipitates with radii < 15nm by electron diffraction. Nevertheless, their EDX-spectra indicate clearly that these precipitates are rich in V and Mo (Fig. 3).

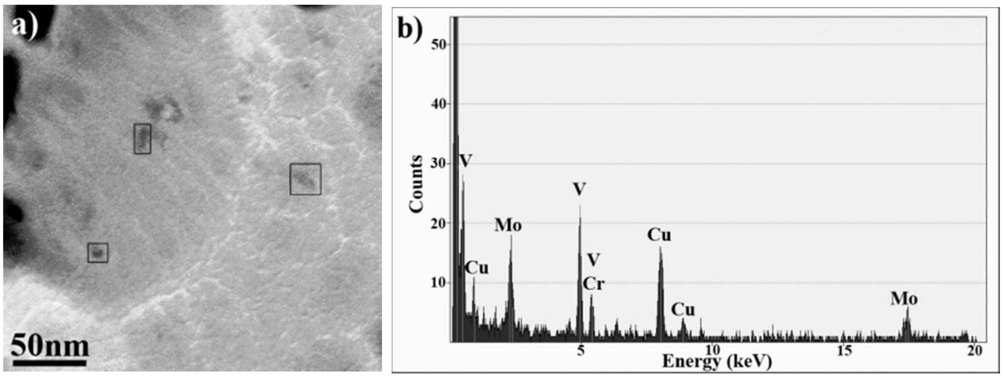

Figure 3: Carbon extraction replica with fine precipitates within the martensite laths (a) and (b) the EDX-spectrum indicating V- and Mo-rich particles. The Cu-peak is due to the Cu-TEM-grids used for the replica.

Two different types of EDX-spectra have been measured for the precipitates at lath boundaries and the cigar-shaped precipitates within the laths. Examples are shown in Fig. 4 and Fig. 5.

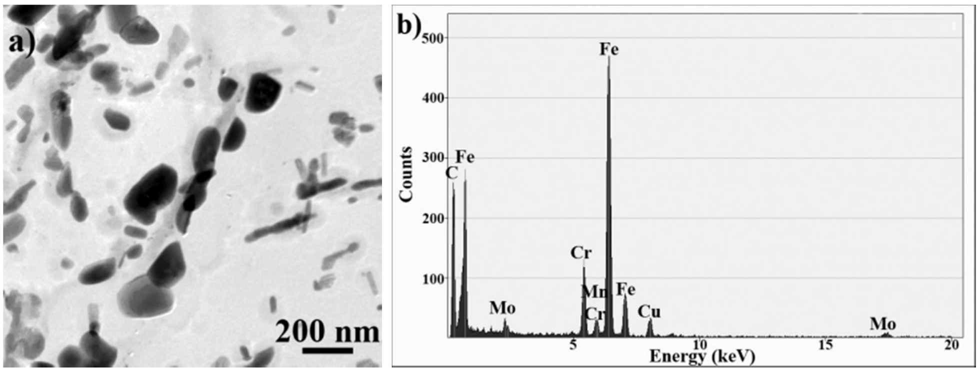

Figure 4: Example for type A precipitates at lath or grain boundaries, this type is also found for cigar-shaped precipitates within the laths (a); (b) shows the EDX-spectrum.

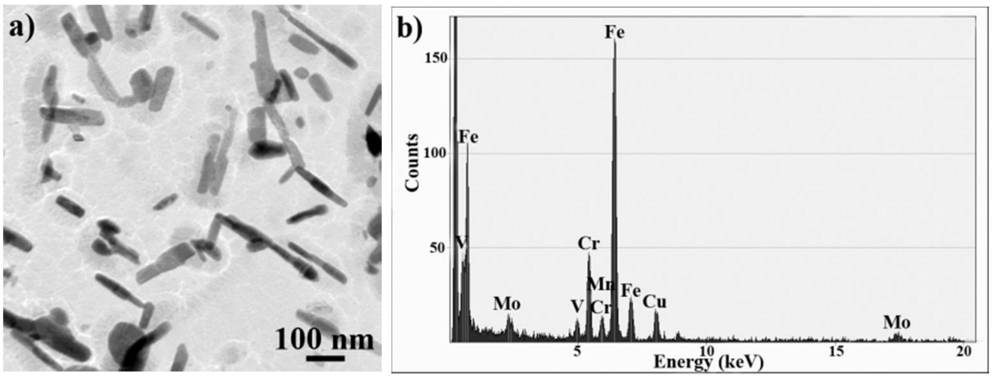

Figure 5: Example for type B precipitates (a); (b) shows the EDX-spectrum with an additional V-peak compared to type A.

4. Modelling approach

4.1 Simulation set up

For the numerical simulation of the precipitation kinetics during the industrial processes of hot rolling and subsequent heat treatment, the chemical composition given in table 1 is used. Table 2 summarizes the main microstructural input parameters for the calculations.

Table 2: Parameters for the numerical simulation.

Precipitation domain phases	Dislocation density / m^{-2}	Precipitate phases	Shape factor for M_3C, M_7C_3	Preferred nucleation sites	
fcc_A1 (austenite); bcc_A2 (bainite, martensite)	$1 \cdot 10^{11}$ (austenite); $4 \cdot 10^{14}$ (bainite); $1 \cdot 10^{15}$ (martensite)	AlN, VN, VC, Mo_2C, Cr_2N, Cementite (M_3C), M_7C_3	3	$AlN_{austenite}$:	dislocations, grain boundaries
				$AlN_{bainite,\ martensite}$:	dislocations
				VN, VC, M_2C, $Cr_2N_{all\ domains}$:	dislocations
				M_7C_3, $M_3C_{bainite}$:	dislocations
				M_7C_3, $M_3C_{martensite}$:	dislocations; subgrain boundaries

For the simulations, it is important to note that the nucleation sites at grain boundaries and dislocations differ with respect to the diffusion geometry for precipitate growth [17]. Along grain boundaries, the diffusivity of elements is enhanced and therefore, the precipitates can grow faster. Furthermore, due to the nature of grain boundaries, the nucleation of precipitates is facilitated because condensation and generation of lattice vacancies easily relax possible misfit strain. For the precipitates, which nucleate at subgrain boundaries, the short-circuit diffusion is considered by a diffusion enhancement factor of 4. The dislocation densities directly determine the number of available nucleation sites and, therefore, the number density of the precipitates. The fact that M_3C and M_7C_3 are found to be cigar-shaped is accounted for by the shape factor of 3 [18].

4.2 Results

During the rolling process, only AlN is predicted to precipitate, which are not dissolved during the austenitization at 880°C and do not change in size and number density when tempered at 690°C. Since all other precipitates are dissolved during austenitization, the results shown in this section only consider the Q&T heat treatment.

For the comparison of experiment and simulation, it is assumed that precipitates with a number density > $10^{17}/\ m^3$ and a mean radius of >1 nm are experimentally detectable in TEM. In a first step, the numerical simulation is performed with all settings left on default values, i.e., no fitting parameters and no calibration of input parameters. The most important interfacial energies are exactly evaluated as described in refs. [19,20]. The microstructural parameters are used as observed in the experiment. Using the settings given in table 2, the results shown in table 3 are obtained. As can be seen, only the M_7C_3 population, nucleated at subgrain boundaries, exists after annealing. However, it does not reach the observed number density. Also, the mean radius does not agree with the experimentally observed sizes. The M_3C precipitates, nucleated at subgrain boundaries, are too small compared to the mean radius of the analyzed precipitates. Moreover, VC is dissolved during annealing and only VN exists at the end, which is also not consistent with experiment.

Table 3: Results of the numerical simulation calculation with the simulation set up given in table 2.

Phase	T_{start} [°C]	Number density / m^{-3}	R_{mean} [nm]	Exp. Obs.	$R_{exp.}$ [nm]
M_3C_sgb	535	$2 \cdot 10^{20}$	28	yes	35 – 60
M_7C_3_sgb	535	$6 \cdot 10^{16}$	60	yes	25 – 35
M_3C_disl	564	$6 \cdot 10^{20}$	23	yes	20 – 30
VN	595	$5 \cdot 10^{20}$	4	no	-
Mo_2C	595	$2 \cdot 10^{19}$	24	yes	<15

Due to the discrepancy with the TEM-analysis using the default parameters, the simulation set up is modified with respect to the nucleation rate of cementite and the interfacial energy of M_7C_3. The nucleation constant of cementite (=multiplicative factor to the nucleation rate) is reduced to a value of $1 \cdot 10^{-3}$ with the consequence that the number density of the particles is decreased. Simultaneously, the precipitates become larger. The interfacial energy of M_7C_3 is lowered with a factor of 0.92 with the consequence that the number density of these particles is increased. Table 4 shows the results of the numerical simulation with the calibrated parameters. Obviously, not only M_3C and M_7C_3 are affected by these changes, but also VC precipitates are now in better agreement with the experiments. Number densities and mean radii of M_3C and M_7C_3 are in the range, which is observed experimentally.

Table 4: Results of the numerical simulation with modified values for nucleation constant of M_3C and interfacial energy of M_7C_3.

Phase	T_{start} [°C]	Number density / m^{-3}	R_{mean} [nm]	Exp. obs.	$R_{exp.}$ [nm]
M_3C_sgb	535	$5 \cdot 10^{19}$	55	yes	35 – 60
M_7C_3_sgb	535	$3 \cdot 10^{19}$	33	yes	25 – 35
M_3C_disl	565	$2 \cdot 10^{19}$	27	yes	20 – 30
M_7C_3_disl	565	$8 \cdot 10^{17}$	11	yes	25 – 35
VN	595	$6 \cdot 10^{20}$	4	no	-
Mo_2C	595	$3 \cdot 10^{19}$	22	yes	< 15
VC	626	$3 \cdot 10^{21}$	4	yes	< 15

5. Discussion

Although, it has been necessary to slightly adapt the simulation set up with respect to the nucleation constant of M_3C and the interfacial energy of M_7C_3, a simulation method is presented, which allows the numerical simulation of the precipitation sequence during a heat treatment based on the industrial processes of hot rolling and subsequent Q& T with more or less no undetermined fitting parameter. Comparing the experimentally observed particles with the numerical simulation, good agreement is achieved. For the experimental analysis by TEM, one has to be aware of the limitations of this method, as already mentioned in the experimental section, it was not possible to uniquely identify the finest precipitates with radii < 15 nm. However, taking into account the EDX-spectra, it is reasonable to assume that these particles are V- and Mo-rich carbides, since no N could be detected. Although it is known that the V- and Mo precipitates do have a significant mutual solubility, the consideration of VN, VC and Mo_2C as separate phases in the simulation is made to alleviate the interpretation of the calculations.

The numerical modeling results have also indicated that further work is necessary to gain a clearer picture with respect to the simultaneous precipitation of concurring precipitates. It seems that there exists some selection mechanism for the nucleation of M_7C_3 and M_3C, both representing Cr-rich carbides, which cannot be explained on a thermodynamic and mobility basis alone. The corresponding mechanism has not been identified up to now and must be further investigated.

6. Summary

The present paper describes a simulation method for the modeling of the precipitation kinetics during a heat treatment based on the industrial process of hot rolling and subsequent quenching and tempering. It is shown that simulations based on the thermo-kinetic models developed recently in the software MatCalc can reasonably well predict the precipitation behavior in an industrial-grade steel. Only slight modifications in the nucleation constant of M_3C and the interfacial energy of M_7C_3 are required to bring experiment and simulation also into quantitative agreement with respect to the observed particle sizes and the number densities. However, it is also found that there exists some need to further investigate the tempering of martensite especially with respect to the question which nuclei, M_7C_3 or M_3C, is kinetically favorable, which selection mechanism for nucleation of concurring precipitates operates and how this can be implemented into the existing model.

8. References

[1] Speich, G.R. and Leslie, W.C.: Met. Trans. Vol. 3 (1972), p. 1043

[2] Lee, W.-S. and Su, T.-T.: J. Mat. Proc. Techn. 87 (1999), p. 198

[3] Ghosh, S.: Scripta Mat. 63 (2010), p. 273

[4] Honeycombe, R.W.K.: Structure and Strength of Alloy Steels, Climax Molybdenum Company,London (1974)

[5] Shaw, S.W.K. and Quarrell, A.G.: J. Iron Steel Inst. Vol. 85 (1957), p. 10

[6] Airey, G.P., Hughes and T.A., Mehl, R.F.: Trans. AIME Vol. 242 (1968), p 1853

[7] Woodhead, J.H. and Quarrell, A.G.: J. Iron Steel Inst. Vol. 203 (1965), p. 605

[8] Thomson, R.C.: Mat. Charact. 44 (2000), p. 219

[9] Dyson, D.J. and Andrews, K.W.: J. Iron Steel Inst. Vol. 207 (1969), p. 208

[10] Kampmann, R. and Wagner, R.: Acta Scripta Metall., Series, Decomposition of alloys: early stages (1984), p. 91

[11] Robson, J.D.: Acta Mater. 52 (2004), p 4669

[12] Yang, J. and Enomoto, M.: ISIJ Vol. 45 (2005), p. 1335

[13] Svoboda, J.; Fischer, F.D., Fratzl, P. and Kozeschnik, E.: Mater. Sci. Eng. A, 385 (2004), p. 166

[14] Kozeschnik, E.; Svoboda, J.; Fratzl, P. and Fischer, F.D.: Mater. Sci. Eng. A. 385 (2004), p. 57

[15] Kozeschnik, E.; Svoboda, J. and Fischer, F.D.: CALPHAD 28 (2005), p. 379

[17] Kozeschnik, E.; Svoboda, J.; Radis, R. and Fischer, F.D.: Modelling Simul. Mater. Sci. Eng. 18 (2010) 015011

[18] Kozeschnik, E.; Svoboda, J. and Fischer, F.D.: Mat. Sci. Eng. A, 441 (2006), p. 68

[19] B. Sonderegger and E. Kozeschnik, Metall. Mater. Trans., 40A (2009) 499-510.

[20] B. Sonderegger and E. Kozeschnik, Scripta Mater. 60 (2009) 635-638.

Paper three

Computational and experimental analysis of carbo-nitride precipitation in tempered martensite

Zamberger S, Wojcik T, Klarner J,
Klösch G, Schifferl H and
Kozeschnik E

Steel Res. Int. Vol 84 No. 1 (2013),
20-30

Computational and experimental analysis of carbo-nitride precipitation in tempered martensite

S Zamberger[1], T Wojcik[2], J Klarner[3], G Klösch[1], H Schifferl[1], E Kozeschnik[4]

[1]voestalpine Stahl Donawitz GmbH, Kerpelystrasse 199, A-8700 Leoben, Austria

[2]Department of Materials Science and Metallurgy University of Cambridge, 27 Charles Babbage Rd, Cambridge CB3 0FS, UK

[3]voestalpine Tubulars GmbH & Co KG, Alpinestraße 17, A-8652 Kindberg, Austria

[4]Christian Doppler Laboratory of Early Stages of Precipitation, Institute of Materials Science and Technology, Vienna University of Technology, Favoritenstrasse 9, A-1040 Vienna, Austria

Abstract. The present work describes the analysis of carbo-nitride precipitation kinetics in tempered martensite of Nb Ti-micro alloyed steel with a carbon content of 0.3wt%. Based on the information obtained from transmission electron microscopy (TEM) and scanning electron microscopy (SEM), a computational simulation procedure is developed within the software package MatCalc, which is capable of describing the experimental results in terms of the number density, composition and type of precipitate phases. No explicit fitting parameters are used in the computer simulation. The input data is entirely based on independent physical or microstructural parameters. To determine the chemical composition and type of precipitates, energy dispersive X-ray (EDX) spectroscopy and selected area electron diffraction (SAD) are utilized. The simulation results and the experimentally obtained information are in good agreement.

1. Introduction

In the production and development of advanced steel, various complex processing steps and thermo-mechanical treatments have to be considered. In the search for new material concepts, usually, several alloy variants are produced as laboratory melts and material properties are investigated. After selection of the most promising candidates, selected steel grades are fabricated on an industrial scale. These single batches are tested and evaluated again before serial production is possible. Unfortunately, this way of materials development is time consuming and cost intensive. Therefore, more and more frequently, thermodynamic and kinetic software packages are used in industrial development departments to assess, which phases occur to which fraction in steel of different chemical composition and thermo-mechanical history.

In the design of micro alloyed steel grades, thermodynamic equilibrium analysis of phases is often insufficient in delivering information about the precipitation behavior of materials in real processes. In this kind of steel, the kinetics of the precipitation processes has decisive influence on type and distribution of precipitating phases and, hence, on the final microstructure and mechanical technological properties of the material. The possibility of predicting precipitation kinetics by computational means opens the way to shorten development times and, thus, the opportunity to reduce cost.

The present work aims at describing the methodology for simulating the precipitation kinetics in a Nb Ti micro alloyed steel with the main alloying elements C, Cr and Mo using the thermo kinetic software package MatCalc [version5.44, rel.1.012]. Compared to a recent paper [1], where the precipitation kinetics in a similar steel, but micro alloyed with V, has been treated computationally, this simulation set up has been improved in three major aspects: (i) the carbo-nitride precipitate phases are defined as multi-component solution phases and not as simplified stoichiometric phases, (ii) due to adjustments in the underlying thermodynamic database, no undetermined fitting parameters were needed in the simulation setup and (iii) precipitation of primary TiN particles is fully taken into account.

The results of the calculations are verified by comparison with experiment. The experimental analysis is done mainly by scanning electron microscopy (SEM) and transmission electron microscopy (TEM). For phase identification, selected area electron diffraction (SAD) is applied and the chemical composition of the precipitates is determined with energy dispersive X-ray spectroscopy (EDX). Experimental data and the results of the numerical simulation are consistent.

2. Computer Simulation

The precipitation model in the present work is based on the numerical Kampmann Wagner approach [2] as implemented in the thermo kinetic software package MatCalc [3-5]. In this model, the thermodynamic extremum principle described by Onsager [6] is applied for derivation of evolution equations for the radius and chemical composition of precipitates within a mean field approach. An extended formulation of Classical Nucleation Theory is used to describe the nucleation processes in multi-component environment [7-9]. Within this computationally efficient modeling framework, it is possible to account for the full system complexity and the most important features of the real technological alloy system. We thus describe the evolution of the radii, phase fractions and number densities of precipitating phases in dependence of a given time temperature profile and chemical composition.

In the simulation setup, precipitation domains, precipitate phases and nucleation sites for the precipitates must be defined. The definition of precipitation domains also involves microstructural parameters, such as dislocation density and grain size. The choice of nucleation sites for the precipitate phases, therefore, directly influences the number of available nucleation sites when evaluating the nucleation rates. Differences in thermodynamic properties and crystal structure of the thermodynamic phase assigned to the precipitation domain determine driving forces and, thus, affect nucleation and growth of precipitates. For example, the driving force for precipitation of a carbide phase in bcc ferrite is generally higher due to low solubility of C compared to fcc austenite. Each of these setup parameters, thus, plays an important role in the entire calculation. Details on the simulation procedure and the theoretical concepts behind MatCalc have been previously reported (e.g. refs. [10-16]).

3. Material and heat treatment

The steel under investigation is a low alloyed C Mn steel with the main alloying elements Cr and Mo; additionally, Nb and Ti are added as micro alloying constituents. The chemical composition of the steel is summarized in table 1. The material is melted in an induction furnace and cast into an ingot mold of dimension 150 x 150 mm^2. The block is milled and, after reheating to a temperature of 1250°C, it is rolled into a dimension of 175 x 29 mm^2. The final heat treatment is a quenching and tempering (Q & T) process, which is performed twice to improve homogeneity and to maintain grain refinement. After austenitization at 880° C and a holding time of 26 min, the material is quenched into water and immediately reheated to tempering temperature of 690°C; the holding time at that temperature is 63 min. A simplified time temperature profile, as used in the simulations, is displayed in figure 1.

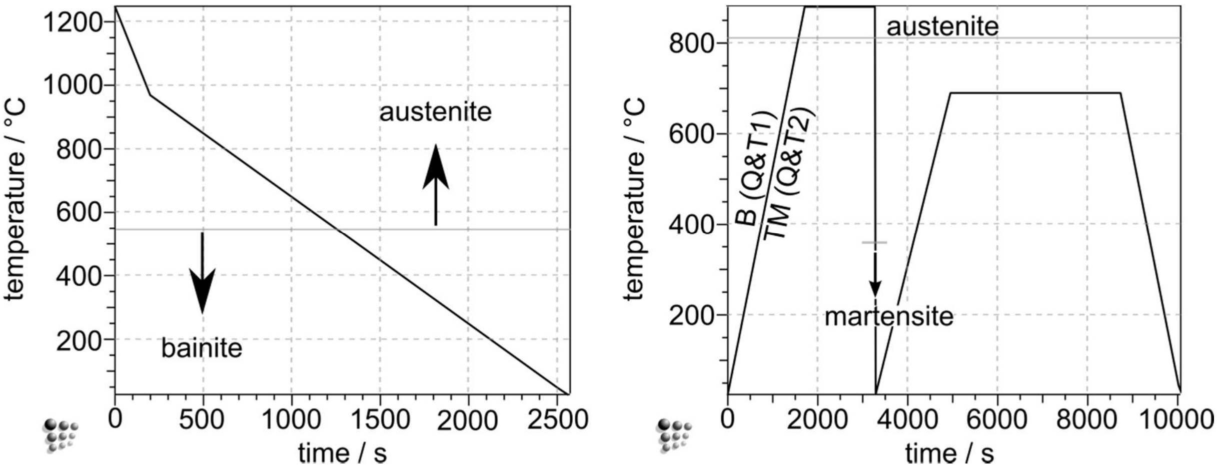

Figure 1: Time-temperature profile of the simulated rolling process (left) and of the quenching and tempering (Q&T) process, which is applied twice (right). The different precipitation domains are also indicated in the figures; B … bainite, TM … tempered martensite. Additionally, the temperatures where precipitation domains are switched are indicated by a grey line. Left: precipitation domain is switched from austenite to bainite during cooling at a temperature of 550°C. Right: precipitation domain is switched from bainite to austenite during reheating at a temperature of 815°C and from austenite to martensite during quenching at 360°C.

Table 1: Chemical composition of the investigated micro-alloyed steel (wt%).

C	Si	Mn	Cr	Mo	V	Al	N	Nb	Ti
0.33	0.29	0.42	0.91	0.75	0.003	0.043	0.011	0.028	0.034

4. Experimental analysis

In figure 2 a), the microstructure of the double-quenched and tempered steel is shown as observed with standard light microscopy. The sample is etched with 3% HNO3. In the center portion of the image, large angular shaped phases are visible, which usually appear salmon colored with this kind of etchant. With SEM and EDX spectroscopy, the phases are identified as carbo-nitrides consisting of Ti, Nb, N and C. Additionally, an automated SEM EDX particle analysis has been performed over a sample area of 127.25 mm^2 with an acceleration voltage of 15 kV and a resolution of 1024 x 800 px and a pixel size of 0.24 x 0.23 µm. The collected data is summarized in the size distribution plot in figure 3. The results indicate the existence of a population of larger TiN particles with a mean radius of around 1.5 µm, together with a population of smaller TiN precipitates around 0.5 µm. Smaller particles cannot be identified with sufficient accuracy using this characterization method.

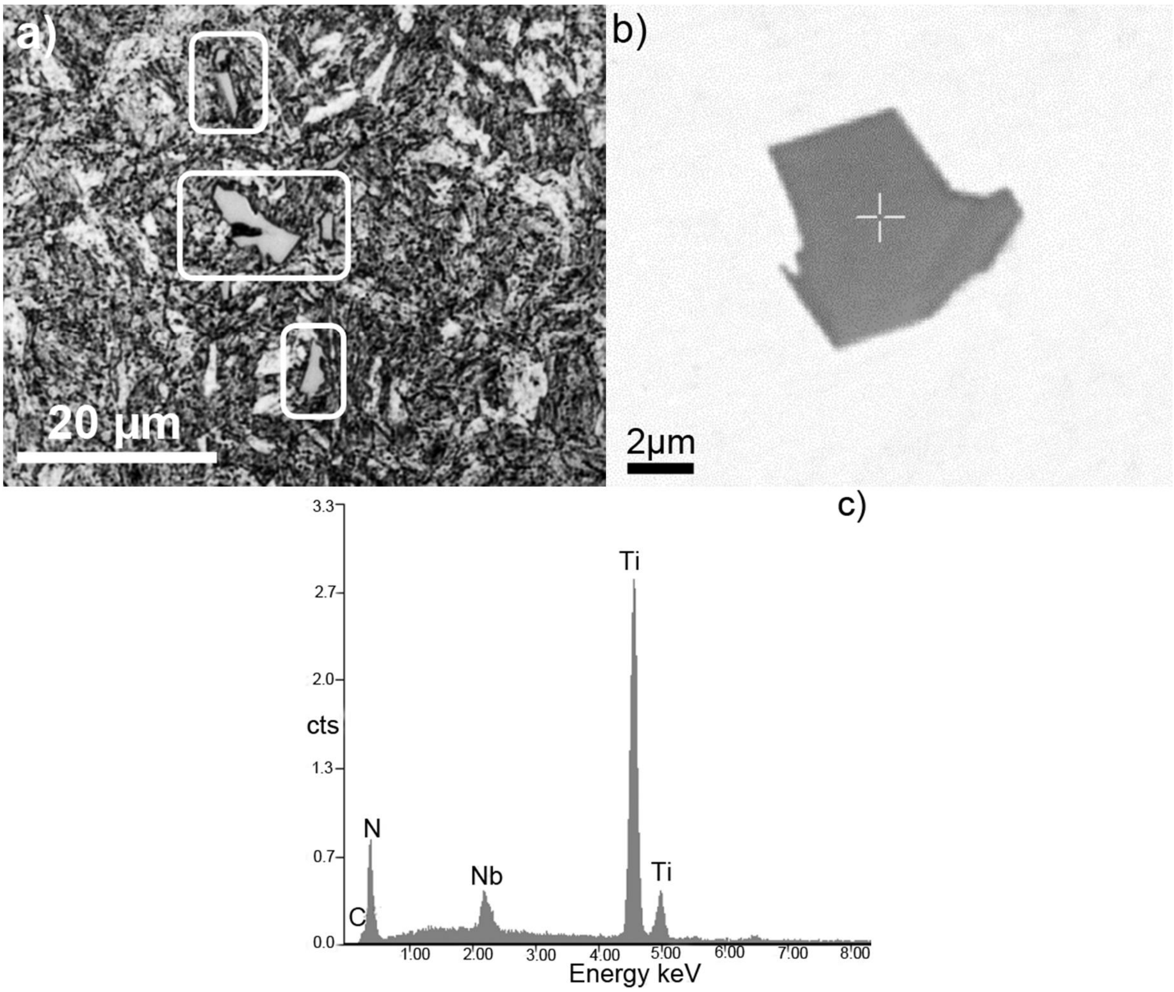

Figure 2: a) Optical micrograph, 3% HNO3 etchant; b) SEM-image and c) EDX-spectrum of the particle in b).

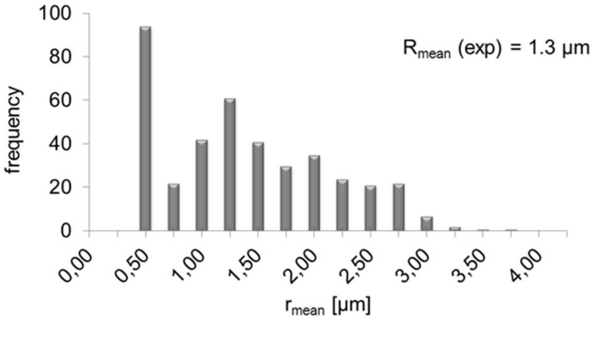

Figure 3: Size distribution of coarse complex TiN evaluated with automated SEM-EDX-particle analysis.

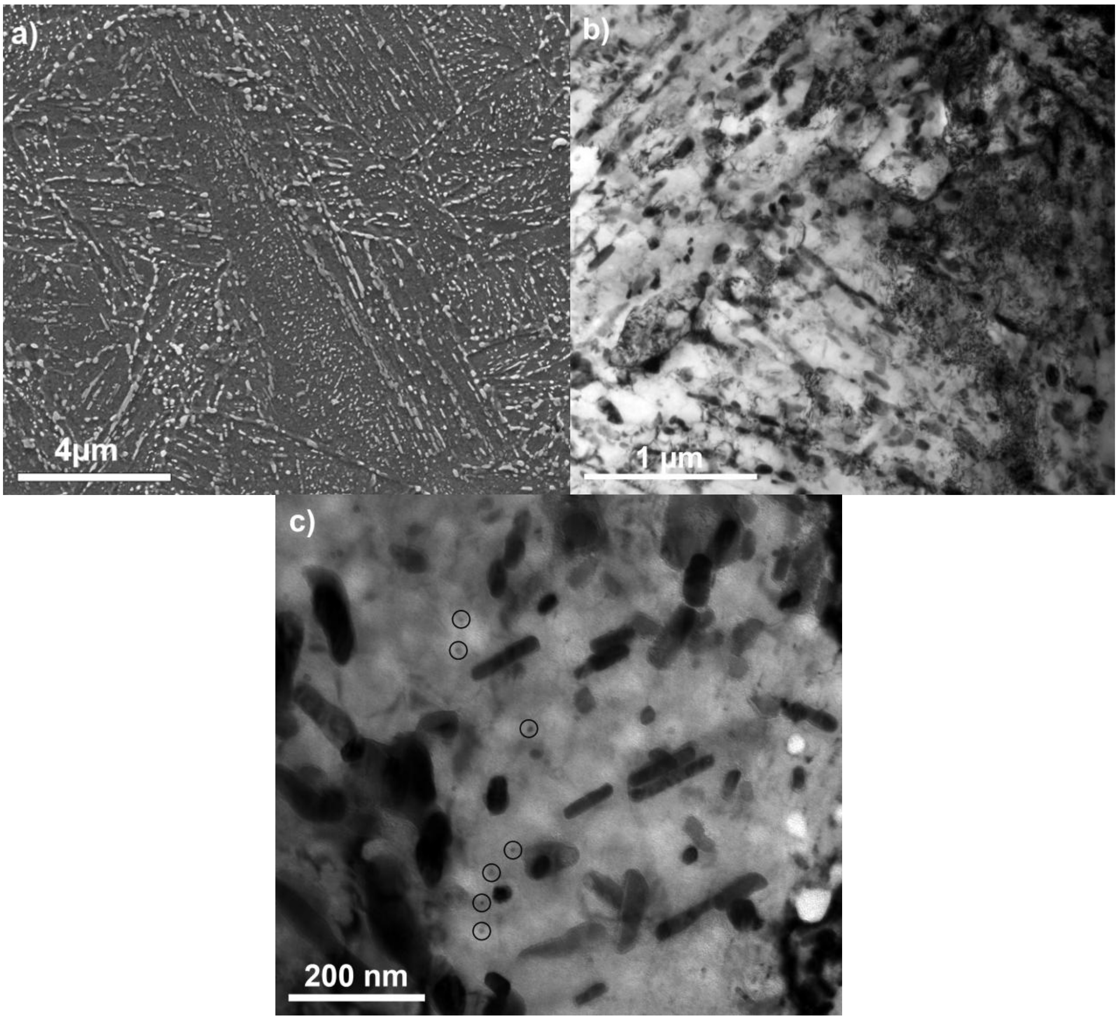

Figure 4: a) SEM-image of an electro-polished foil; b) TEM-bright field image and c) TEM-bright field image with higher resolution; fine precipitates are marked with circles.

Further investigations are performed on electro-polished foils and carbon extraction replica with SEM and TEM. TEM analyses are performed with a FEI TECNAI F20 operating at 200kV equipped with EDX and EELS (electron energy loss spectroscopy) facilities. The SEM- and TEM-images in figure 4 show a high number density of precipitates in the investigated microstructure. The nucleation sites of precipitates are mainly martensite lath boundaries and dislocations inside the laths. This precipitation behavior of M_3C and M_7C_3 has also been reported earlier by Speich and Leslie [17] for comparable C-Mn steel. Details of the precipitate morphology are displayed in figure 5, showing elongated particles on lath boundaries but also inside the laths. The other type of intralath particles is smaller and more spherical.

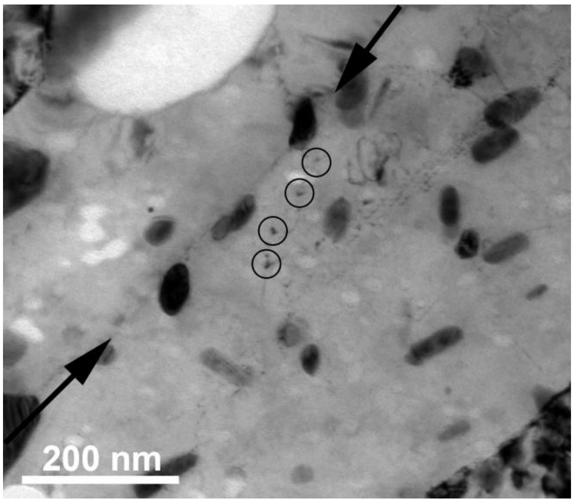

Figure 5: TEM-bright field image of an electro-polished foil. The lath boundary is indicated by arrows, small spherical precipitates are marked with circles.

The length of elongated lath boundary precipitates is in the range of 30 to 90 nm. The length of the intralath particles is in the order of 20 to 60 nm. In identification of M_7C_3-carbides compared to the M_3C particles, we utilize the special feature of M_7C_3 to show extensive stacking faults. These cause characteristic streaks in the diffraction pattern [18,19], making M_7C_3 therefore clearly recognizable by SAD. The M_7C_3-carbides have a mean radius of 20 to 30 nm. M_3C are observed with a mean radius of 30 to 65nm (figure 6). MC-type precipitates have typical radii between 3 and 12 nm (figure 7).

The EDX-spectra of precipitates can be distinguished by two types of chemical composition: The larger particles are typically (Fe,Cr)-rich, sometimes with traces of Mo. In lower density, smaller spherical intralath particles are identified with a similar spectrum. The small spherical particles are Nb-rich with traces of Ti and, occasionally, also of Mo and Fe. The Cu-signal in figure 7 b) is attributed to the TEM grid used for specimen preparation for carbon extraction replica. These results conform to other published data in literature, where similar steel grades have been investigated [18-25].

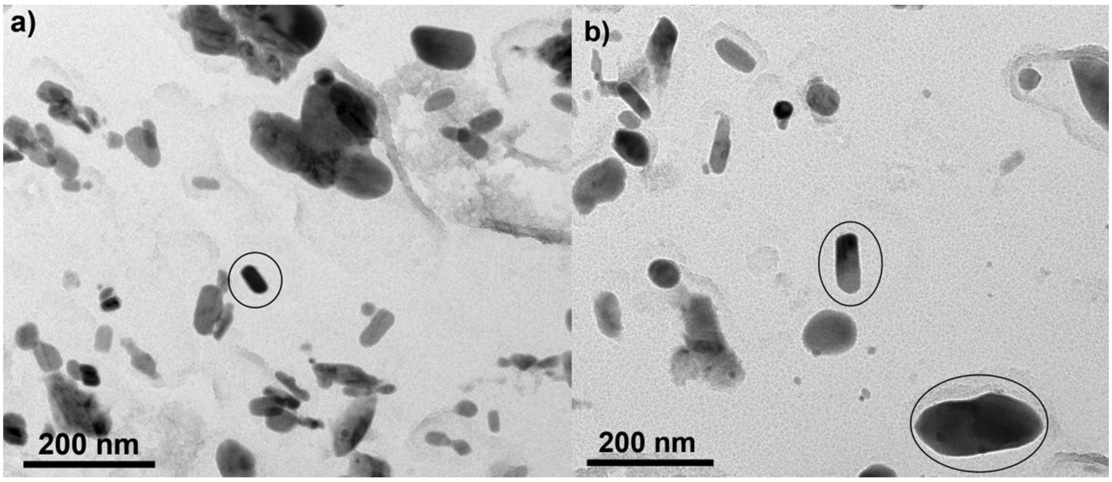

Figure 6: TEM-bright field images of carbon extraction replicas. a) in circles: M$_7$C3 identified with SAD and b) two M3C particles.

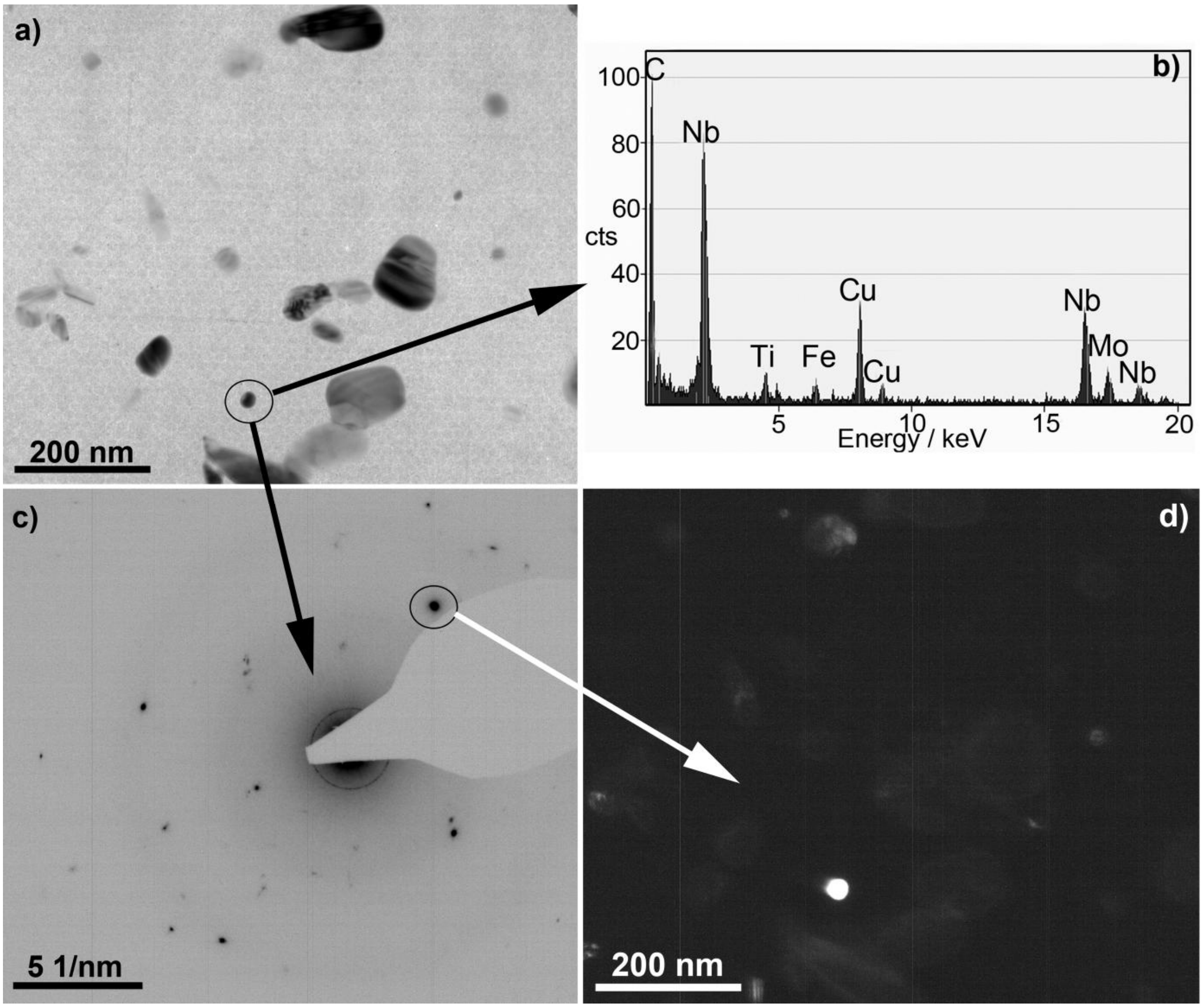

Figure 7: a) TEM-bright field image of a carbon extraction replica. An MC-particle is marked by a circle. b) EDX-spectra of this particle. The Cu-signal comes from the grid for sample preparation of the carbon extraction replica. c) SAD image of the MC precipitate. d) Dark field image of the corresponding precipitate.

5. Simulation setup

The set-up for the numerical simulation is based on the set-up, which has been used in ref. [1], with the major differences that (i) the precipitates are not treated as simplified stoichiometric phases, but as complex solution phases; (ii) due to a reassessment of the implemented thermodynamic database, no additional adjustments are applied and (iii) coarse primary TiN precipitation is fully taken into account with the Scheil-Gulliver simulation technique and a corresponding 'virtual' pre-treatment. This procedure allows taking into account primary precipitates in the precipitation kinetics routines. Details of this procedure are elaborated below.

5.1 Matrix phases and precipitates

The thermo-mechanical treatment investigated in this work involves precipitation processes in the austenite as well as the ferritic/martensitic state. In order to specify the transformation temperatures for the matrix phase governing the precipitation processes, the software package JMatPro [26] is used. For definition of the austenite to ferrite/martensite and ferrite/martensite to austenite transformation temperatures, a continuous time-temperature-transformation diagram is calculated. Based on the applied cooling rate in the steel production process after hot rolling, JMatPro predicts that the transformation of austenite proceeds into mainly bainite. The 50% transformation temperature from austenite (fcc) to bainite (bcc) is predicted to occur at around 550°C. During fast quenching, the material transforms into body-centered tetragonal (bct) martensite. The martensite start temperature is calculated with 360°C. Homogeneous austenite after reheating should be reached at a temperature of 815°C.

The dislocation densities of the matrix phases are taken from literature with 10^{11} m^{-2} for annealed austenite, $4 \cdot 10^{14}$ m^{-2} for bainite and 10^{15} m^{-2} for martensite [27,28]. In our simulations, bainite and martensite are treated thermodynamically as ferrite (bcc_a2). They only differ by their dislocation density. The high solubility of C at dislocations is presently neglected. For the dislocation density in the fully tempered martensite, a value of 10^{12} m^{-2} is assumed, which corresponds to a typical value of the bcc ferrite structure [17,27]. Further input parameters, which are determined from experimental information, are the prior austenite grain size and the martensite subgrain size.

The precipitate phases that are accounted for in our simulations are selected from experimental information from earlier investigations [1] as well as thermodynamic equilibrium calculations. Accordingly, we consider the precipitate phases AlN, Mo-rich and Cr-rich-phases with hexagonal lattice, and Nb-, Ti- and Mo-rich phases with fcc structure (MC-type), as well as Fe- and Cr-rich phases with complex orthorhombic structure (M_7C_3 and M_3C). The hexagonal phases are of M_2C and M_2N type (see also refs. [17-25]).

In the simulations, we face the difficulty of various precipitates owing the same crystal structure and, for this reason, being modeled as solution phases with identical thermodynamic data in the CALPHAD modeling. For instance, the TiN, NbC and cubic MoC precipitates are all derived from the parent fcc_a1 type. In the present simulations, use is being made of the possibility in MatCalc to define 'composition sets'. These are phases that inherit the thermodynamic properties of the parent phase, in this case fcc_a1, but contain only those elements that are relevant for the particular phase. With this simplification, the numerical efficiency of the simulation is greatly enhanced, while conserving the overall behavior of the phases in the calculations. In addition to the phase constituents, the major constituents are defined according to experimental observation. Table 2 summarizes the phase selection and settings performed in the present simulations.

Table 2: Definition of composition sets of precipitate phases in the thermo-kinetic simulation with MatCalc. Va is the abbreviation for vacancies.

Equilibrium phase	Phase constituents (substitutional:interstitial: sublattice)	Major constituents (substitutional:interstitial: sublattice)	Phase type
fcc_a1	:Cr,Mn,Mo,Nb,Ti:C,N,Va:	:Ti:N:	TiN
fcc_a1	:Cr,Mn,Mo,Nb,Ti,V:C,N,Va:	:Nb:C,N:	Nb(C,N)
fcc_a1	:Cr,Mn,Mo,Nb,Ti,V:C,N,Va:	:Mo:C:	MoC
hcp_a3	:Cr,Mn,Mo,Nb,V:C,N,Va:	:Cr:N:	Cr_2N
hcp_a3	:Cr,Mn,Mo,Nb,Ti,V:C,N,Va:	:Mo:C:	Mo_2C
cementite	:Cr,Fe,Mn,Mo,V:C,N,Va:	:Fe:C:	M_3C
M_7C_3	:Cr,Fe,Mn,Mo,V:C,Va:	:Cr,Fe:C:	M_7C_3

In addition to the phase constituents, the potential nucleation sites must be provided for each precipitate as an input quantity. This setting is obtained from experimental observation and it controls the number density of the particles and the diffusion field geometry used in the simulation (random distribution or grain boundary, see ref. [29] for details). For AlN precipitates, the nucleation sites in austenite are grain boundaries and dislocations [29-31], M_3C and M_7C_3 are assumed to nucleate at subgrain boundaries and dislocations. All other phases nucleate on dislocations only. The precipitation domains and precipitate phases participating in the simulations are summarized in table 3.

Table 3: Precipitation domains, precipitating phases and nucleation sites.

Precipitation domain	Precipitate	Nucleation sites	Population name
Pre-austenite	TiN	virtual pre-treatment	TiN(pre-aust)
Austenite	AlN, TiN, NbCN, MoC, Mo_2C, Cr_2n	Grain boundaries, dislocations for AlN; all other on dislocations	AlN(aust,gb), AlN(aust,d), TiN(aust), Nb(C,N)(aust), MoC(aust), Mo_2C(aust), Cr_2N(aust)
Bainite	AlN, TiN, NbCN, MoC, Mo_2C, Cr_2N, M_7C_3, $M_{23}C_6$, M_3C	Dislocations	AlN(bain), TiN(bain), Nb(C,N)(bain), MoC(bain), Mo_2C(bain), Cr_2N(bain), M_7C_3(bain), $M_{23}C_6$(bain), Cem(bain)
Martensite	AlN, TiN, NbCN, MoC, Mo_2C, Cr_2N, M_7C_3, $M_{23}C_6$, M_3C	Dislocations, subgrain boundaries for M_7C_3 and M_3C	AlN(mart), TiN(mart), Nb(C,N)(mart), MoC(mart), Mo_2C(mart), Cr_2N(mart), M_7C_3(mart,sgb), M_7C_3(mart,d), $M_{23}C_6$(mart), Cem(mart,sgb), Cem(mart,d)

Further input parameters are a shape factor of 3 for M_3C and M_7C_3, according to the experimentally observed aspect ratio (a detailed description of the shape factor implementation into the model is given in ref. [32]), and a diffusion enhancement factor of 4 to account for faster diffusion along the subgrain boundaries compared to the bulk volume. The pipe diffusion mechanism along dislocations is an important diffusion mechanism in the martensite and bainite phase. This effect is fully taken into account in the simulations as a function of dislocation density.

5.2 Virtual heat treatment for primary TiN particles

In the Ti-micro-alloyed steel grades investigated here, primary TiN precipitation in the residual liquid pockets already starts during the solidification process, triggered by severe Ti segregation [33,34]. Although the MatCalc framework is not designed for kinetic simulations in the liquid state, these coarse particles can be accounted for in the calculations by a combination of the Scheil-Gulliver simulation technique and a virtual (pre-) heat treatment. In the present case, this pre-treatment consists of an isothermal holding at 1445°C for 10^5 sec.

In the first step of this procedure, the Scheil-Gulliver module of MatCalc is employed to evaluate the amount and type of primary precipitates at a residual liquid fraction of 3%. Details on this type of simulation are described in ref. [35]. With the chemical composition of the present steel, the complex TiN phase is predicted to exist in the primary solidification microstructure with a phase fraction of approx. 0.052 %. In the second step, a kinetic simulation is performed with a purely hypothetical time-temperature profile that has the only purpose of precipitating TiN in the same amount and with approximately the same chemical composition as given by the Scheil-Gulliver calculation. The virtual pre-treatment simulation is commonly not based on real, or physically-based, heat treatment parameters. In the context of merely representing a means of accounting for primary precipitation, the virtual treatment can be carried out with any kind of simulation input parameters that lead to the desired primary precipitate distribution.

At the end of the virtual pre-treatment, primary TiN particles are present in the simulation system, and can seamlessly be considered in the further calculations. In this way, the simulation also correctly accounts for the effective Ti- and N-content of the matrix, excluding the Ti and N atoms, which are bound in the primary precipitates and which are not available for precipitation as secondary precipitates. The primary and secondary precipitates considered in the simulations are defined in table 3.

6. Results

6.1 Virtual heat treatment

In figure 8, the result of the numerical simulation of the virtual heat treatment is depicted in the form of a size distribution plot. The precipitating phase consists of mainly Ti and N, with small amounts of C and Nb. When analyzing the results of the Scheil-Gulliver simulation data in detail, we find that more than 65 % of the total Ti and more than 50 % of the total N are concentrated in the primary precipitates. With our virtual pre-treatment technique, these findings are (artificially) reproduced and integrated into the precipitation simulation.

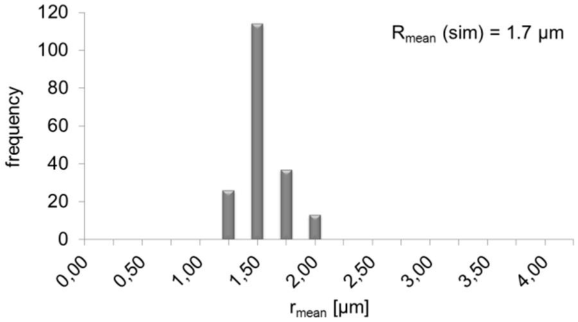

Figure 8: Calculated precipitate distribution of TiN after the virtual (pre-) heat treatment.

6.2 Precipitation kinetics

At the end of the first Q & T treatment (see Figure 1), all phases are predicted to be present in the microstructure, except M_7C_3(bain), M_3C(bain), Mo_2C(bain) and $M_{23}C_6$(bain). In parenthesis, the precipitation domain is indicated, in which nucleation of the particular precipitate population has occurred. This is also marked in fig. 1. Figure 9 shows that, during reheating to austenitization temperature, some precipitate populations start growing initially but dissolve in the course of isothermal holding at 880°C later again. TiN(aust), Nb(C,N)(aust), Nb(C,N)(bain) and AlN(bain) remain stable over the entire heat treatment period. During reheating to T = 690°C and annealing, TiN(bain) precipitates start growing and reach saturation after ~7.500 sec. Both populations of M_7C_3 and Cem(mart) precipitate within the period of reheating to annealing temperature. They also reach saturation during annealing at 690°C. The Mo-rich phases, Mo_2C(mart) and MoC(mart) are metastable and dissolve after about 5.500 and 7.000 sec, respectively. The triangles in figure 9 indicate the experimental values of the mean radii identified by TEM. It should be noted, here, that the discontinuities in the mean radius plot stem from the Kampmann-Wagner time integration procedure, where certain small but numerous particle classes dissolve due to coarsening. This procedure is accompanied by a transient decrease of the mean radius and a sharp increase after the precipitate class has completely dissolved.

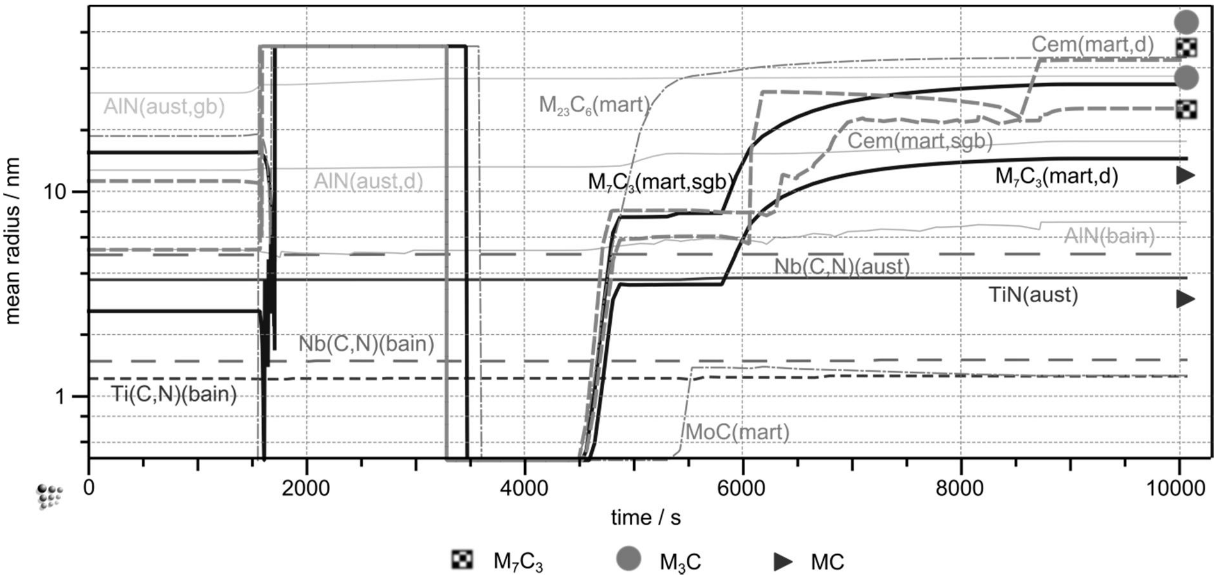

Figure 9: Mean precipitate radii vs. time of the second Q & T treatment compared to the experimentally determined mean radii of M_7C_3, M_3C and MC identified by TEM.

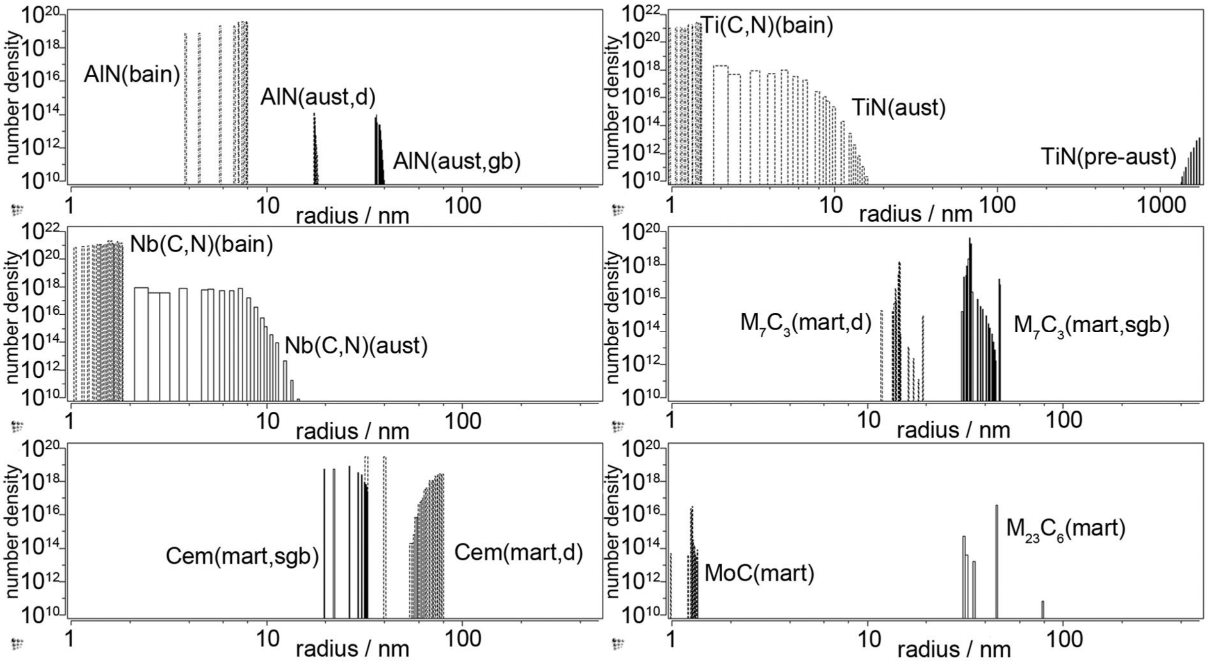

Figure 10: Calculated size distributions of precipitates after the second Q & T treatment.

In figure 10, the calculated size distribution plots of the precipitates after the second Q & T treatment are depicted. TiN and Nb(C,N) precipitates in austenite and in bainite exist with high number density. None of these phases precipitates in martensite in a considerable amount. The dominating phases in the martensitic precipitation domain are both populations of M_7C_3 and cementite (M_3C). Also, a small fraction of MoC and $M_{23}C_6$ forms in the martensitic matrix as visible in figure 10, bottom right.

A closer look on the chemical composition of the complex precipitate phases in table 4 reveals that the Ti-rich phases are carbo-nitrides, whereas the Nb-rich phases are (Nb,Ti)-carbides. However, the chemical composition of the phases changes with respect to the time-temperature history of the process. Figure 11 shows the varying carbon and nitrogen contents of the TiN(aust) phase. After the rolling process, the phase is more or less pure TiN. During the first Q & T treatment, the C content reaches its maximum at the beginning of the annealing by replacing N, drops again in the course of the second austenitization and, finally, increases a second time to the end value of about 18 at%. The Nb-rich phases that have nucleated in austenite and ferrite are quite stable in terms of their chemical composition. In Nb(C,N)(bain), the Ti-content drops during the first austenitization from about 18 at% to a value of 10 at%, whereas Nb increases by this value. The calculated final compositions are given in table 4.

Table 4: Calculated chemical composition of the mixed carbo-nitride phases (at%) at the end of the thermal treatment.

Population name	Ti	Nb	N	C	T_{start} [°C]
TiN(aust)	49.9	0.1	31.9	18.0	1210
Nb(C,N)(aust)	18.0	32.0	0.2	49.8	1160
Nb(C,N)(bain)	10.6	39.4	0.1	49.9	550
TiN(bain)	50.0	-	31.8	18.2	550

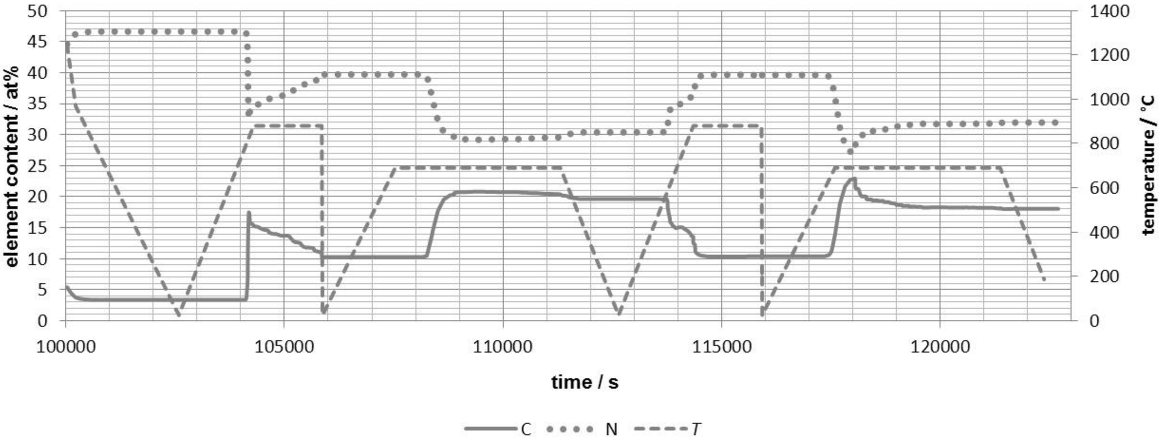

Figure 11: C (solid line) and N (dotted line) content of TiN(aust) with respect to the time-temperature profile (dashed line) of the process.

7. Discussion

On comparison of the experimental data with the results of the numerical simulation, the agreement is good concerning both populations of M_3C and M_7C_3. Experimentally, the observed particle radii of the latter population are in the range of 20 to 30 nm, whereas the former ones lie within 30 and 65 nm. The calculated mean radii are 75 nm for M_3C located at dislocations and 85 nm at subgrain boundaries, whereas they are 40 nm for M_7C_3 at dislocations and 85 nm at subgrain boundaries.

In several numerical simulations, it has been assumed that the nucleus composition of cementite particles after quenching and short-term tempering is of para-equilibrium type [36-43]. Especially, in systems containing only Mo, Mn and Si as alloying elements, cementite can form as para-composition precipitate

[36-38] which, later on during prolonged tempering, changes to ortho-equilibrium composition. Preliminary numerical analysis for our steel grades showed that para-equilibrium cementite would form and grow much too rapidly, however, compared to experimental evidence. Consequently, when including para-composition cementite into the simulations, the calculated particle sizes and number densities during tempering do not correspond to the observation. Although, para-composition cementite represents a possible precipitate variant, in the present alloys containing strong carbide formers, such as Cr, Mo, Nb, Ti or V together with a high density of lattice defects [44], indications are that cementite precipitation is significantly delayed, thus providing evidence towards a suppression of para-composition cementite nucleation. Therefore, ortho-equilibrium is chosen here as pre-condition for cementite nucleation.

Taking the Ti- and Nb-rich phases together, also, their calculated mean radii with 2 to 5 nm agrees well with the experimental values of 3 to 12 nm. The EDX-spectra of the Ti-carbo-nitrides and the (Nb,Ti)-carbides indicate that the experimentally observed particle sizes are in good accordance with the latter precipitate type. Unfortunately, with the help of SAD, it is not possible to differentiate clearly between these phases, since their lattice parameters are very similar. Therefore, a small uncertainty remains with respect to the exact type of the observed phases. Nevertheless, we believe that the results of the numerical simulation reflect the microstructural features of the material under investigation fairly good.

A slight discrepancy is found with respect to AlN precipitation. This has already been reported and discussed in ref. [1]. The MoC and $M_{23}C_6$ populations predicted to be present in the steel by our simulation have not been identified in the investigated samples. However, the calculated number density of 10^{16} m^{-3} corresponds to one particle per μm^3; hence, the probability to find these particles in a TEM investigation is extremely small. Moreover, $M_{23}C_6$ is chemically very similar to M_7C_3 and M_3C, which would make a clear identification possible only with SAD, which is rather time consuming and difficult.

8. Summary and Conclusions

The present work complements the investigations started in a recent work [1], which has demonstrated the application of a new simulation procedure for the calculation of precipitation kinetics in a quenched and tempered medium C-Mn steel micro-alloyed with V. In the present simulation, the main microalloying elements are Nb and Ti. The precipitating phases are no longer treated as idealized pure phases, such as NbC or TiN, but as complex solution phases with the parent fcc_a1 crystal structure and thermodynamics. The phases are defined via ‘composition sets’, where those elements are considered only, which are relevant for the particular phase. The major constituents of the precipitating phases are defined according to experimental information. Applying this methodology, it is possible to consider all phases in the simulation, which show mutual miscibility, like e.g. the carbides and nitrides of the micro-alloying elements, and to analyze the precipitation behavior and evolution of their mean chemical composition during processing. The results of numerical calculations correspond well with the experimentally found precipitate types and sizes.

The results suggest that the same simulation methodology can be applied also to steels with similar chemical composition but varying contents and types of micro-alloying elements. The thermo-kinetic approach presented here represents a convenient and powerful computational means to optimize heat treatments and/ or chemical compositions according to desired materials properties by numerical simulations.

9. References

[1] S. Zamberger, E. Kozeschnik: Mater. Sci. Forum Vols. 706-709 (2012), 1586.

[2] R. Kampmann, R. Wagner: Acta Scripta Metall., Series, Decomposition of alloys: early stages (1984), 91.

[3] J. Svoboda, F.D. Fischer, P. Fratzl, E. Kozeschnik: Mater. Sci. Eng. A, 385 (2004), 166.

[4] E. Kozeschnik, J. Svoboda, P. Fratzl, F.D. Fischer: Mater. Sci. Eng. A, 385 (2004), 57.

[5] E. Kozeschnik, J. Svoboda, F.D. Fischer: CALPHAD 28 (2005), 379.

[6] L. Onsager: Physical Reviews I, Vol. 37, (1931), 405.
L. Onsager: Physical Reviews II, Vol. 38, (1931), 2265.

[7] G. Koenraad, F. Janssens, D. Raabe, E. Kozeschnik, M.A. Miodownik, B. Nestler: Computational Materials Engineering - An Introduction to Computational Microstructure Evolution of Polycrystalline Materials, Elsevier Publishing, ISBN 978-0-12-369468-3, 2007.

[8] B. Sonderegger, E. Kozeschnik: Metal. Mater. Trans., 40A (2009) 499.

[9] B. Sonderegger, E. Kozeschnik: Scripta Mater. 60 (2009) 635.

[10] B. Sonderegger, E. Kozeschnik, H. Leitner, H. Clemens, J. Svoboda, F.D. Fischer: Int. J. Mat. Res. 99 (4), 2008, 410-415.

[11] R. Radis, M. Schaffer, M. Albu, G. Kothleitner, P. Pölt and E. Kozeschnik: Acta Mater., 57 (2009) 5739-5747.

[12] I. Holzer and E. Kozeschnik: Mater. Sci. Forum 638-642 (2010) 2579-2584.

[13] R. Radis and E. Kozeschnik: Model. Simul. Mater. Sci. Eng. 18 (2010) 055003 (16pp).

[14] M. Pudar, S. Zamberger, K. Spiradek-Hahn, R. Radis and E. Kozeschnik: Steel Res. Int. 81 (2010) 372-380.

[15] R. Radis and E. Kozeschnik: Steel Res. Int. 81 (2010) 681-685.

[16] R. Radis, S. Schwarz, S. Zamberger and E. Kozeschnik: Steel Res. Int. 82 (2011) 905-910.

[17] G.R. Speich, W.C. Leslie: Metal. Mater. Trans. B, Vol. 3 (1972), 1043.

[18] R.C. Thomson: Mater. Characterization, Vol. 44 (2000), 219.

[19] D.J. Dyson, K.W. Andrews: J. of the Iron Steel Institute, Vol. 207 (1969), 208.

[20] W.-S. Lee, T.-T. Su: J. Mater. Process. Techn., Vol. 87 (1999), 198.

[21] S. Ghosh: Scripta Mater., Vol. 63 (2010), 273.

[22] R.W.K. Honeycombe: Structure and Strength of Alloy Steels, Climax Molybdenum Company, London, 1974.

[23] S.W.K. Shaw, A.G. Quarrell: Journal of the Iron Steel Institute, Vol. 85 (1957), 10.

[24] G.P. Airey, T. A. Hughes, R.F. Mehl: Trans. AIME, Vol. 242 (1968), 1853.

[25] J.H. Woodhead, A.G. Quarrell: Journal of the Iron Steel Institute, Vol. 203 (1965), 605.

[26] N. Saunders, N. Guo, X. Li, A. P. Miodownik, J.-Ph. Schille: Journal of the Minerals, Metals and Materials Society, Vol. 12 (2003), 60.

[27] D. Hull, D.J. Bacon: Introduction to dislocations, Pergamon Press, Ltd. Oxford, UK, 1992

[28] C. Garcia-Mateo, F.G. Caballero, C. Capdevila, C. Garcia de Andres: Scripta Mater., Vol. 61, (2009), 855.

[29] E. Kozeschnik, J. Svoboda, R. Radis, F.D. Fischer: Model. Simul. Mater. Sci. Eng., 18 (2010), 015011.

[30] R. Radis, E. Kozeschnik: Model. Simul. Mater. Sci. Eng., 18 (2010), 055003.

[31] R.Radis, S. Schwarz, S. Zamberger, E. Kozeschnik: Steel Res. int., Vol. 82 (2011), No. 8, 905.

[32] E. Kozeschnik, J. Svoboda, F.D. Fischer: Mater. Sci. Eng. A, Vol. 441, (2006), 68.

[33] K.-I. Suzuki,S. Miyagawa, S. Yoshiyuki, K. Shiotani: ISIJ International, Vol. 35 (1995), 34.

[34] L.P. Zhang, C.L. Davis, M. Strangwood: Metal. Mater. Trans. A, Vol. 32 (2001), 1147.

[35] E. Kozeschnik, W. Rindler, B. Buchmayr: Int. J. Mater. Res., 98 (9), 2007, 826-831.

[36] S.S. Babu, K. Hono, T. Sakurai: Metal. Mater. Trans. A, Vol. 25 (1994), 499.

[37] G. Ghosh, G.B. Olson, G.B: Acta Mater., Vol. 50 (2002), 2099.

[38] M.K. Miller, P.A. Beaven, G.D.W. Smith: Metal. Mater. Trans. A, Vol. 12 (1981), 1197.

[39] R.C. Thomson, M.K. Miller: Appl. Surf. Sci., Vols. 87/88 (1995), 185.

[40] R.C. Thomson, M.K. Miller: Acta mater., Vol. 46, (1998), No. 6, 2203.

[41] G. Ghosh, G.B. Olson: Metal. Mater. Trans. A, Vol. 32 (2001), 455.

[42] R.C. Sharma, G.R. Purdy: Metal. Mater. Trans. A, Vol. 5 (1974), 939.

[43] E. Kozeschnik, H.K.D.H. Bhadeshia: Mater. Sci. Techn., Vol. 24, (2008), 343.

[44] M. Maalekian, E. Kozeschnik: Calphad, Vol. 32, (2008), 650.

Paper four

Experimental and computational study of cementite precipitation in tempered martensite

Zamberger S, Whitmore L,
Krisam S, Wojcik T and
Kozeschnik E

Modelling Simul. Mater. Sci. Eng. 23
(2015) 055012, 22pp

Experimental and computational study of cementite precipitation in tempered martensite

S Zamberger[1], L Whitmore[2], S Krisam[2], T Wojcik[2] and E Kozeschnik[2]

[1] voestalpine Stahl Donawitz GmbH, Kerpelystraße 199, 8700 Leoben, Austria

[2] Christian Doppler Laboratory for „Early Stages of Precipitation", Institute of Materials Science and Technology, Vienna University of Technology, Favoritenstraße 9-11, 1040 Vienna, Austria

Abstract. In this work, we investigate cementite precipitation during tempering of quenched 0.3C-1Cr-1Mo steel with martensitic microstructure at temperatures between 400 and 700°C. Particular focus is laid on the evolution of the Cr-content of particles during tempering, where we observe a transition from fast C diffusion-controlled to slow Cr diffusion-controlled kinetics. For characterization of the precipitates, transmission electron microscopy (TEM) in combination with thermokinetic simulation is applied. With a new concept for treatment of inner-particle diffusion in the framework of the SFFK model implemented in the software MatCalc, a successful simulation of cementite precipitation kinetics and Cr enrichment of precipitates is carried out over the entire temperature range.

1. Introduction

To meet the customers' material requirements, the steel producers are challenged to develop steel grades with tailored properties with respect to H-embrittlement, strength and toughness. The steels under consideration are typically low-alloyed C steels with Cr and Mo additions as well as microalloying elements, such as, V in the present case. This type of material is most frequently quenched and tempered (Q&T) to control the ultimate properties, since Q&T provides high flexibility in achieving desired combinations of toughness and strength. At present, the standard heat treatment is a double Q&T process for increased homogeneity and grain refinement [1,2]. During the heat treatments, various kinds of precipitates are formed within the steel that all impact the long-range diffusion of H. Consequently, the control of type, amount and morphology of precipitates is a key feature for controlling the sour gas performance of the final material. The steel under investigation has been produced at laboratory scale within an ongoing research project dealing with the investigation of H-trapping in microalloyed steels.

The precipitation behaviour of cementite during the tempering of martensite is the main focus of the present work, since the precipitation kinetics of cementite is also essential for the evolution of other carbide types, such as, in the present case, VC. The chemical composition of the cementite precipitates is analysed as a function of temperature and holding time by experimental and computational means.

The various metallurgical processes that occur during tempering are generally well known. The tempering process starts with stage I, the precipitation of transition carbides, followed by stage II, the decomposition of retained austenite and stage III, the precipitation of cementite. Additionally, often a 0th stage is reported, which describes the process of C atom cluster formation during cooling or heating at low temperatures. In alloyed carbon steels, a 4th stage occurs, which is related to the precipitation of alloy-carbides. The latter effect is also denoted as secondary hardening, see, e.g. [3-9].

Before elaborating details on the present cementite precipitation model, the terms most frequently used in this context are summarized. It is widely accepted, see e.g. Coates [10], that phase transitions in interstitial-substitutional systems, such as Fe-C-X, where X is a slow diffusing substitutional element and C commonly diffuses several orders of magnitude faster, can be described by local thermodynamic equilibrium (LE) across the interface governed by three modes. These are (i) local equilibrium (LE) with full partitioning of all elements, (ii) negligible partitioning (NP-LE) of substitutional elements, full partitioning of interstitials , (iii) paraequilibrium (PE), with no partitioning of substitutional elements and local equilibrium established only for the interstitial components or (iv) a mixture of all modes in the so-called mixed-mode (MM) model [11]. The first case is observed if the slow diffusing element is the rate-controlling component and the growth rate is low. In the other cases, the fast diffusing element is the rate controlling element and the growth rate is high. In the NP-LE regime, the concentration profile of X shows a very narrow enriched region in front of the interface. Coates called this region a ‘*spike*’, which is pushed ahead of the interface as the transformation proceeds. In PE, the slow diffusing element and the solvent are not involved at all in any kind of elemental redistribution by diffusion. The substitutional elements only influence the chemical potentials of interstitial elements on the two sides of the interface. The chemical composition evolution of precipitates is determined by the simultaneous solution of diffusional transport and mass balance across the interface in the sense of a moving boundary problem. Exemplarily, this is demonstrated for Cr-carbides in the framework of the DICTRA software in refs. [12,13], as well as in chapter 9.1 of ref. [14].

In contrast to the conventional local equilibrium-based approaches, in the present work, we utilize a model that is based on the thermodynamic extremal principle and a formulation of the precipitation problem in terms of mean-field quantities. This model offers substantial computational advantages, since it can be conveniently applied to complex multi-component precipitation reactions without the necessity of having to solve the multi-component formulation of Fick's second law in the interfacial area with a moving phase boundary. However, local chemical enrichment of precipitates in, e.g., only the outer shells of the particles, are inherently difficult to describe in a mean-field model, since the redistribution of elements in the precipitate is dependent on the precipitate size and it becomes increasingly difficult for larger precipitates due to increasing diffusion distance from the surface to the precipitate centre. Details of the models, corresponding references and an in-depth discussion of this issue are presented in chapter 3 describing our simulations.

Most studies dealing with cementite precipitation suggest that, at low tempering temperatures and/or short tempering times, the chemical composition of the carbides in terms of substitutional elements is similar or identical to that of the matrix. This corresponds to a growth mechanism controlled by PE or NP-LE [5,15-19]. At higher temperatures, where the substitutional elements become increasingly mobile, the cementite precipitates gradually adopt higher substitutional alloy contents [20,21]. Ghosh et al. [6] observed deviations from the PE/NP-LE state already after a tempering time of 15 min at 510°C. Significant Cr-enrichment in Q&T steels of comparable composition and tempering schedule have been reported earlier for tempering at 690°C [22,23].

2. Experimental

The chemical composition of the material is summarized in table 1. The laboratory melt was produced in a standard induction furnace under ambient atmosphere. It was cast into blocks of about 70 kg with a cross-section of 150 x 150 mm² and a length of about 300 mm. Before rolling, the as-cast blocks were ground to avoid surface defects. The rolling schedule was designed according to the industrial rolling process. The material was reheated to 1250°C, followed by a rough rolling and a final rolling step at lower temperatures to a thickness of 30.7 mm with subsequent slow cooling. The plate was reheated to 1050°C and rolled into dimensions of 175 x 29 mm² at 720°C. Finally, a double

Q&T process was performed, where the plates were austenitized at 920°C for 1 hr, quenched and tempered at 700°C for 2 hrs. The austenite grain diameter in this condition is about 16 µm (ASTM E112).

Table 1: Chemical composition of the steel under investigation (in wt%).

C	Si	Mn	Cr	Al	Mo	V	N
0.31	0.27	0.40	0.89	0.029	0.77	0.094	0.010

The dilatometer samples investigated in this study were machined from these plates. The heat treatment schedule applied afterwards is performed with a Baer dilatometer 805A/D. The austenitization temperature was 1250°C, which is above the calculated solution temperature of all precipitates. The heating rates for both, austenitization and annealing, are 100 K/s. The annealing treatment was performed at 400, 500, 600 and 700°C for 1 min, 10 min and 60 min. The samples were quenched to room temperature after austenitization (~ 200K/s) and tempering (~ 55K/s) in a He-Jet.

The dilatometer-samples are then cut into two pieces where one half is used for light optical microscopy and the other half is used for transmission electron microscopy (TEM) analysis. After grinding and polishing, the samples were etched with HNO_3. The TEM specimens have been prepared in a combination of mechanical lapping, polishing and electropolishing with a perchloric acid based electrolyte. TEM analysis was performed in an FEI TECNAI F20 operating at 200 kV equipped with an EDX (energy dispersive x-ray) analysis device.

3. Simulation

In this section, the methodology developed for simulation of the precipitation kinetics of cementite is outlined. Particular attention is laid on the evolution of the Cr-content of the cementite particles during tempering as a function of temperature and time. This issue is dealt with in detail because we observed a need to extend the existing model implemented in the thermo-kinetic software package MatCalc [24] to account for the (smooth) transition from fast C diffusion-controlled growth of cementite without any incorporation of Cr in the precipitates (PE or NP-LE growth mode) to the slower Cr diffusion-controlled growth kinetics with Cr partitioning (e.g., MM or LE growth).

The precipitation kinetics model utilized by MatCalc is based on the size-class oriented numerical Kampmann-Wagner [25] approach. The thermodynamic extremum principle [26,27] forms the conceptual foundation for derivation of evolution equations for the radius and chemical composition of the precipitates, as outlined in the original manuscripts [28-30], denoted further as the SFFK model and briefly reviewed later. For simulation of nucleation, an extended multi-component formulation of classical nucleation theory is utilized [31]. The interface energy is computed from the generalized broken bond model [32] taking into account the effect of interfacial curvature [33]. In our simulations, the interface energy is not treated as a fitting parameter. For a prediction of the chemical composition of the cementite nuclei, we utilize the minimum nucleation barrier concept [34].

With this model, we attempt to describe the evolution of radii, phase fractions and number densities of the precipitating phases in dependence of a given time-temperature profile and chemical composition.

3.1 Chemical composition of cementite nuclei

Classical nucleation theory (CNT) was originally developed for the description of droplet condensation from supersaturated vapour [35,36] and later developed further by several researchers for solid-state nucleation processes. Based on CNT, the transient nucleation rate, J, describes the number of nuclei that are created per unit volume and unit time as [37]

$$J = NZ\beta^* \exp\left(-\frac{G^*}{RT}\right)\exp\left(-\frac{\tau}{t}\right). \tag{1}$$

N (see appendix A) is the number of available nucleation sites, Z is the Zeldovich factor, β^* is the atomic attachment rate given as [28]

$$\beta^* = \frac{4\pi\rho^{*2}}{a^4\nu^\alpha}\left[\sum_{i=1}^{n}\frac{\left(c_{ki}-c_{0i}\right)^2}{c_{0i}D_{0i}}\right]^{-1}, \tag{2}$$

with

$$\rho^* = \frac{2\gamma}{\Delta G_{\mathrm{vol}}} . \tag{3}$$

ρ^* is the critical radius, a is the lattice spacing, γ is the interfacial energy between precipitate and matrix and ΔG_{vol} is the volume free energy change. v^α is the molar volume as defined in ref. 28, $c_{\mathrm{k}i}$ is the mean concentration in the precipitate k (k = 1, ..., m), c_{0i} is the mean concentration of component i in the matrix [28], and D_{0i} are the diffusion coefficients of all components i in the matrix (i = 1, ..., n). The values taken for the diffusivities are incorporated in the diffusion database of the thermokinetic software package MatCalc. τ in equation (1) is the incubation period, t is the time and G^* is the nucleation barrier, which is given by

$$G^* = \frac{16\pi}{3} \frac{\gamma^3}{\left(\Delta G_{\mathrm{vol}}\right)^2} . \tag{4}$$

Since G^* enters in equation (1) in the exponent, it is the most essential quantity in nucleation theory compared to the other quantities in equation (1). For any prescribed chemical composition of the precipitate, the nucleation rate is unambiguously determined by these equations. For an in-depth discussion of this topic, see, for instance, the corresponding chapter in ref. [14].

However, the chemical composition of the nuclei is not determined ‘a-priori’. Instead, it must be fixed by some additional assumption. Typically, the concept of maximum driving force is applied, where the chemical composition of the nucleus is evaluated from the condition of equal chemical potential difference between matrix and precipitate for all involved elements. This concept is also known as the parallel tangent construction. Another common assumption is para-equilibrium (PE), i.e., negligible diffusion of substitutional elements and only partitioning of fast, interstitial diffusers, such as C or N.

In the present work, we rely on a more general concept, where the composition of the nucleus is determined by the minimum of the nucleation barrier, eq. (4). This concept delivers the chemical composition as a function of temperature and supersaturation in a balance between energy cost (interfacial energy) and gain (chemical driving force / bulk free energy change) for the critical nucleus. We assume that the particle, which is most likely to be observed in an experimental analysis, corresponds to the particular one with minimum G^* [34]. In this approach, the maximum driving force concept and para-equilibrium composition appear naturally as limiting cases of either extremely low or extremely high supersaturation.

3.2 Evolution of precipitate chemical composition

In our simulations, the radius and chemical composition evolution of each precipitate as well as the matrix is described in the framework of a mean-field approach (SFFK model) [28]. Consequently, the precipitate chemical composition and the composition of the matrix are expressed in terms of mean quantities. This is depicted in Fig 1, showing the assumed concentration profiles in the case of a mean-field model and the "real" profile in a space-resolved approach with a narrow "reaction layer".

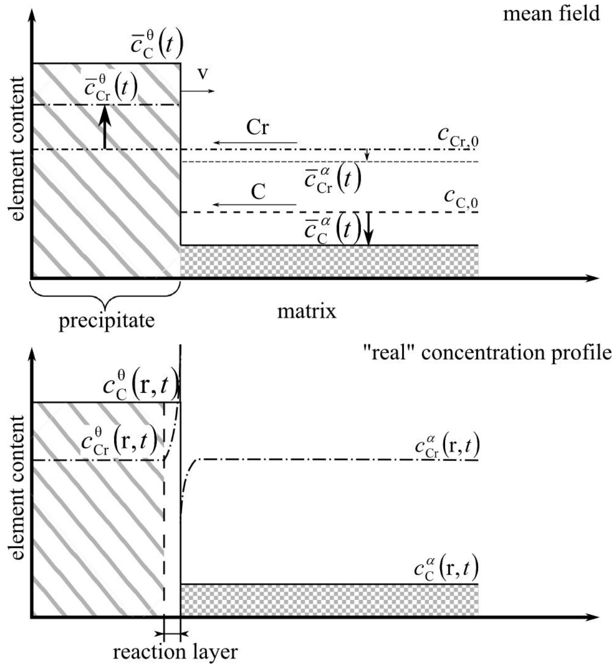

Figure 1: Sketch of the element concentration in the matrix and the precipitate as assumed in the mean field simulation and in the "real" situation. See text for discussion.

In the sketch for the mean-field model, the initial (nominal) composition is denoted by the subscript '0' for the elements C and Cr. The horizontal arrows indicate the diffusional fluxes of elements towards the precipitate, which can either cause growth of the precipitate by attachment of atoms to the precipitate surface with correlated interface movement with a velocity *v* determined by the constraint of mass balance or enrichment of the precipitate with, e.g., Cr, as indicated by the vertical arrows. In general, the evolution of precipitate radius and composition occurs simultaneously with certain fractions of either of these two mechanisms. The actual selection of how much growth and how much chemical composition change occurs is made by the Onsager thermodynamic extremal principle (TEP) [26]. Accordingly, the evolution of precipitates happens such that the rate of entropy production achieves a maximum [27,38]. Although, the corresponding model in MatCalc has been successfully applied numerous times, e.g., refs. [39-45], in the present case of cementite precipitation during martensite tempering, some special attention must be paid to the question of the evolution of the precipitate chemical composition.

The second plot in Fig. 1 sketches “real” concentration profiles of fast diffusers, here, C and slow diffusers, here, Cr. In the image, we assume that the first part of the precipitation reaction is dominated by C diffusion and the “real” composition profile for C has already become flat on both sides of the precipitate/matrix interface. Accordingly, the C diffusion-controlled part of the reaction has already come to a stop. At this stage, the interface movement has become so slow that partitioning of slow diffusing Cr commences, visible in the steep Cr gradient inside the precipitate with significant Cr enrichment close to the precipitate/matrix interface. We denote this area as the “reaction layer”, since growth/shrinkage of the precipitate occurs almost independently of the constitution of the volume inside the reaction layer.

In a mean-field model, this mechanism is difficult to mimic since the formation of a thin reaction layer (see Fig 1) close to the precipitate/matrix interface is not incorporated in the modelling concept. In the SFFK model, Cr enrichment of the precipitate always involves the continuous enrichment of the entire precipitate at the same time, instead of enriching only a small interfacial layer. Since the enrichment kinetics of the precipitate is mainly determined by the diffusion coefficient of elements inside the precipitate (see original treatment of the SFFK model [29]), this parameter is also strongly controlling the predictions of the TEP. If diffusion inside the precipitate is sluggish, the corresponding dissipation rate is low and the TEP predicts that the precipitate evolves with mainly changing its radius instead of enriching in Cr. In contrast, if the diffusion coefficient inside the precipitate is high, significant entropy production can occur by redistribution of elements inside the precipitate and Cr enrichment is favoured over radius change.

Even more important for the present study is the dependence of the free energy dissipation rate from precipitate size. Since any enrichment of elements in the precipitate is connected with diffusional redistribution of this element over the entire precipitate volume, this mechanism becomes more and more difficult with increasing particle size. This means that, once a precipitate has reached a certain critical size, the TEP will tend to predict large gradients in the radius evolution and small to negligible gradients for the composition change.

In the present work, we explicitly address this issue in dealing with a situation where cementite precipitates nucleate and grow in a highly supersaturated environment with a chemical composition close to the PE limit. After precipitate growth ceases, due to matrix depletion from fast diffusing C, with accompanying reduction of the chemical driving force, Cr enrichment of the precipitates offers an alternative mechanism for efficient free energy dissipation. Experimental evidence shows that this dissipation process occurs only within a small reaction layer, see, e.g., the DICTRA simulations of cementite dissolution in austenite presented in ref. [12,13] together with experimental concentration profiles measured across the precipitate/matrix interface.

In a mean-field based simulation, effects going beyond the local resolution of the model formulation can only be accounted for indirectly. A simple, yet efficient, way to incorporate the effect of a small reaction layer in the simulation that compensates for the decreasing redistribution capacity of larger particles, is to artificially increase the diffusion coefficient inside the particle. In the present work, the amount of increase is assumed to scale with particle size. Consequently, we introduce a coefficient, α, defined as

$$\alpha = \left(\frac{r}{r_0}\right)^n, \qquad (5)$$

where r is the radius of the precipitate, r_0 is the thickness of this hypothetic reaction layer (assumed to be 1 nm), and n is an exponent, which adopts values from 0 (no effect) to approximately 2 (increase scales with r^2). The effective diffusion coefficient inside the precipitate is then evaluated as

$$D_{\mathrm{eff}}^{\mathrm{prec}} = \alpha \cdot D_0^{\mathrm{prec}}. \qquad (6)$$

Subsequently, we first summarize the input parameters entering the simulations. Then, we investigate the capabilities of the suggested model in the form of a parameter study. Finally, we compare our results with experimental data obtained with TEM and EDX analysis.

4. Simulation Setup

The objective of this chapter is to describe the simulation set up and additional features in MatCalc that must be accounted for and that are used in the calculations. In the simulation, several microstructural and thermo-physical parameters are needed and simulation boundary conditions, such as, e.g., the grain and subgrain size of the matrix (precipitation domain), the dislocation density as well as the preferential heterogeneous nucleation sites for precipitates. These are also discussed below and in the appendix.

When studying precipitation in the course of martensite tempering, the evolution of all microstructural features in the course of the heat treatment, such as, for instance, the mean dislocation density, are of key importance. Since the virgin martensitic microstructure after quenching contains a high number of excess dislocations, which determine the number and type of available nucleation sites for the carbides, we track the dislocation density evolution by accounting for static recovery on basis of a one-parameter model for the evolution of the mean total dislocation density [46]. Although, in the present case, the material has not been plastically deformed by external strain, the observed microstructural evolution is comparable to that of deformed material. In our analysis, we see clear evidence of recovery of the transformation-induced dislocations [3,9]. We do not observe experimental evidence for possible recrystallization of the martensitic microstructure, which is why we neglect this restoration mechanism.

In the simulation, the calculation starts in a precipitate-free condition at T = 1250°C. The precipitation domain in the beginning is austenite (thermodynamic parent phase is fcc_a1) with an assumed dislocation density of 10^{11} m^{-2} [47], corresponding to a well-annealed defect-poor condition. For the grain diameter after austenitization at 1250°C, an estimated value of 75 µm is used in accordance with experimental results obtained in the as-quenched condition.

MatCalc precipitation simulations always refer to a representative volume element. Consequently, on cooling, the precipitation domain is changed instantaneously from austenite to martensite at a temperature of 310°C, which corresponds to the particular temperature where 50% austenite has transformed to martensite. This temperature is observed experimentally by dilatometry. The martensite phase is thermodynamically treated as bcc_a2 with a high amount of excess dislocations. In the as-quenched condition, the total dislocation density is assumed to be 10^{15} m^{-2} and the dislocation density in the fully annealed condition is assumed to be 10^{13} m^{-2} [47,48]. Possible effects caused by the tetragonality of martensite are neglected, since tetragonality is lost at temperatures above 300°C and tempering starts at 400°C [49].

The precipitating phases and the assumed heterogeneous nucleation sites are summarized in table 2. Detailed information on the definition of the composition sets has been reported earlier in ref. [23]. From a survey of literature [9], we expect that Fe_3C, Cr_7C_3, Mo_2C, AlN and VC precipitate in the current steel. Figure 2 shows a sketch illustrating potential heterogenous nucleation sites for cementite in martensite. These are former austenite grain boundaries, martensite lath boundaries and excess as well as geometrically necessary dislocations within the laths [5,15,43,50-52]. For the present simulations, only martensite lath boundaries and dislocations are considered, since this corresponds well with the field of view in the accompanying TEM analysis. The martensite lath boundaries are treated like subgrain boundaries. Due to the increased defect density inside subgrain boundaries, the diffusion coefficient of substitutional alloying elements along these microstructural features is artificially enhanced by a factor of 2. At dislocations, the acceleration of diffusion kinetics by pipe diffusion is accounted for according to Radis et al. [53] and using the pipe diffusion data compiled by Stechauner et al. [54].

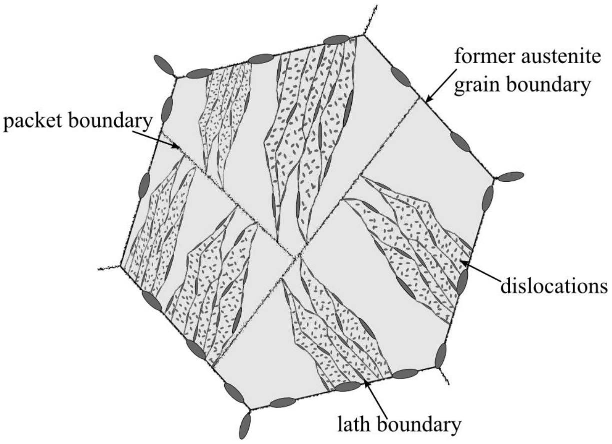

Figure 2: Sketch of the assumed microstructure after Q&P with heterogeneous nucleation sites of cementite as utilized in the numerical simulation.

All precipitates are assumed to be spherical, except for the M_3C and M_7C_3 phases, where we use shape factors in correspondence with the experiments. These shape factors account for the non-spherical diffusion fields during growth of the precipitates [55]. In an earlier study, we have assumed that cementite particles are needle-like, however, in the present detailed study, we observe that the cementite particles are platelets and, therefore, the shape factors are set to 0.3 for intra-lath cementite and 0.5 for inter-lath cementite and M_7C_3 [56].

Table 2: Precipitates, lattice structure, nucleation sites (NS), stoichiometry with major constituents (tagged with '%') in the austenitic and martensitic matrix as defined in the numerical simulation. lb ... lath boundaries; d ... dislocations

Phase	Matrix phase	Alias Name	Lattice structure	NS	Composition (:substitutional:interstitial:)
VC	Austenite	VC(A)	fcc	d	:Fe,Cr,Mn,Mo,V%:C%,N:
AlN	Austenite	AlN(A)	hex	d	:Al:N:
AlN	Martensite	AlN(A)	hex	d	:Al:N:
VC	Martensite	VC	fcc	d	:Fe,Cr,Mn,Mo,V%:C%,N,:
Mo_2C	Martensite	Mo_2C	hex	d	:Fe,Cr,Mn,Mo%, V:C%:
M_7C_3	Martensite	M_7C_3(lb); M_7C_3(d)	trigonal	lb; d	:Cr%,Fe%,Mn,Mo,Si,V:C%:
Cementite	Martensite	cem(lb); cem(d)	ortho-rhombic	lb; d	:Cr,Fe%,Mn,Mo,Si,V:C%:

Experimentally, we observe Mo_2C precipitation inside the martensite subgrains. Unfortunately, in the simulations, this phase becomes kinetically unstable using only default parameter settings for this phase. The main reason is identified in the mean-field approximation of the SFFK model, where every precipitate interacts with each other via the mean-field matrix independent of its actual location. In practice, Mo_2C precipitates nucleate inside the subgrains and they are, for this reason, to some degree spatially separated from (more stable) precipitates at the subgrain boundary. Experimentally, we observe that this separation stabilizes Mo_2C over the timespan of our investigations. In an attempt to mimic this increased relative stability, we manually add a Gibbs energy offset (SE-parameter) with a value of -1000 J/mol in addition to the Gibbs energy defined in the thermodynamic database of MatCalc [5.61rel.0056]. Moreover, we assume that the precipitate/matrix interface shows a certain degree of dilution, which provides a mechanism that effectively reduces the interfacial energy. This effect is taken into account, here, with the model developed by Sonderegger and Kozeschnik [57] and utilizing a regular solution critical temperature of 1800 K.

5. Results and Discussion

In this chapter, first, the experimental observations are summarized. Then, the results of the parameter study on the influence of the radius-dependent diffusion coefficient exponent, *n*, on the evolution of the cementite radius and composition is introduced. Finally, experiment and simulation are compared and discussed.

5.1 Experimental results

Figure 3 shows typical microstructure images of the investigated material obtained with light optical microscopy. In figure 3a, the as-quenched martensitic structure is depicted, whereas figure 3b displays the condition after tempering for one hour at 700°C.

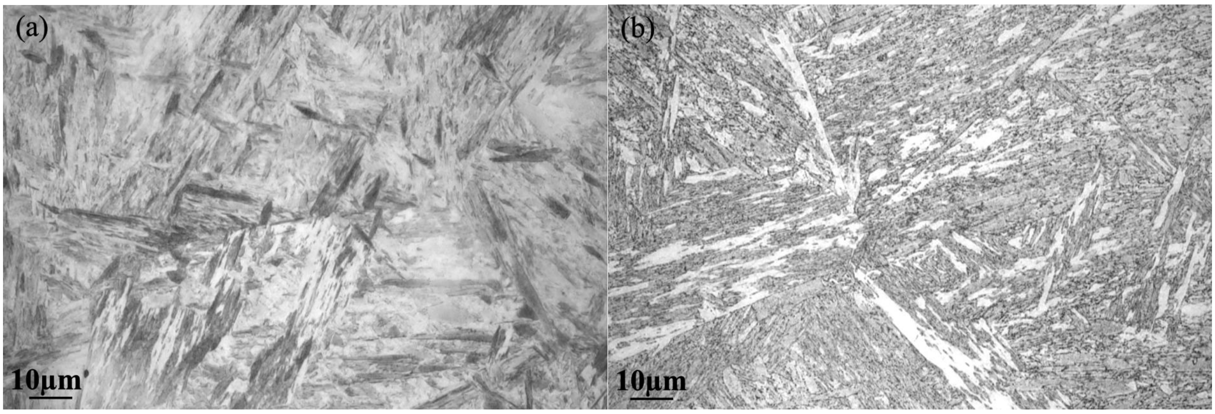

Figure 3: (a) Microstructure of the as-quenched sample and (b) of the sample tempered for 1 hr at 700°C. Light optical microscopy; HNO_3 etched.

In figures 4a and b, transmission electron microscopy (TEM) bright field images of the samples annealed for one hour at 400°C and 700°C, are depicted. In both conditions particles are visible, although, in figure 4b, the particles seem to be more distinct and easier to recognize than in figure 4a. This is due to a higher degree of recovery in the sample annealed at the higher temperature. No precipitates have been detected in the as-quenched condition. Figures 5a and b show TEM bright-field images of the sample annealed at 700°C for 60s. The particles sizes are determined from the TEM-images by utilizing the software ImageJ (1.47v) [58]. The size distributions of the samples tempered at 700°C are presented in figure 6. From the diagrams it can be seen that the particles tend to coarsen with increasing tempering time, since the relative frequency of the small size classes decreases.

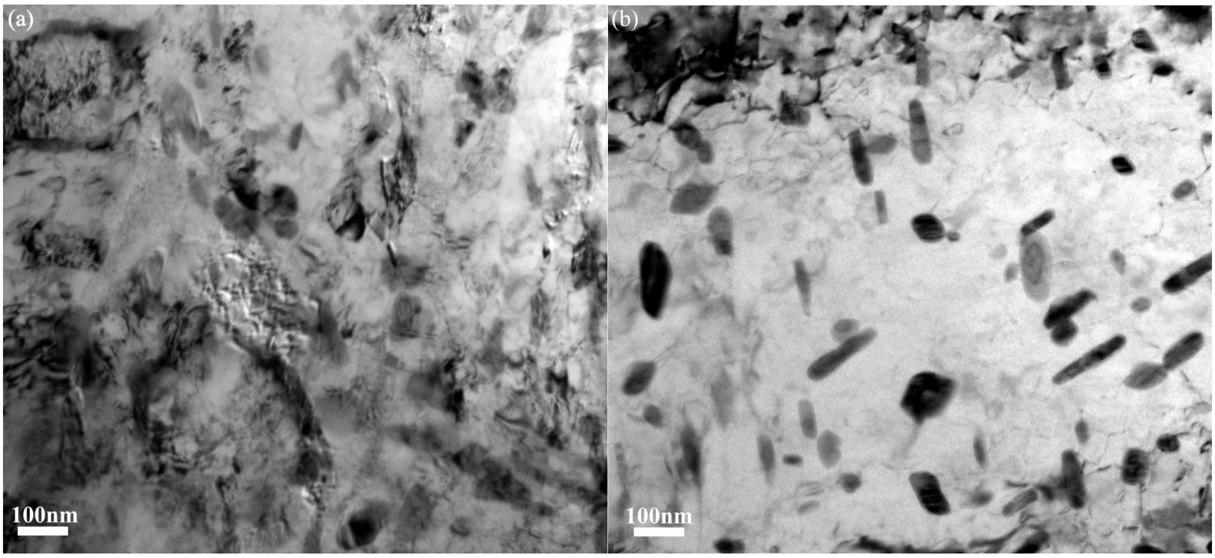

Figure 4: TEM bright field images of sample 4 annealed for 1 hr at 400°C (a) and sample 13 tempered for 1 hr at 700°C (b).

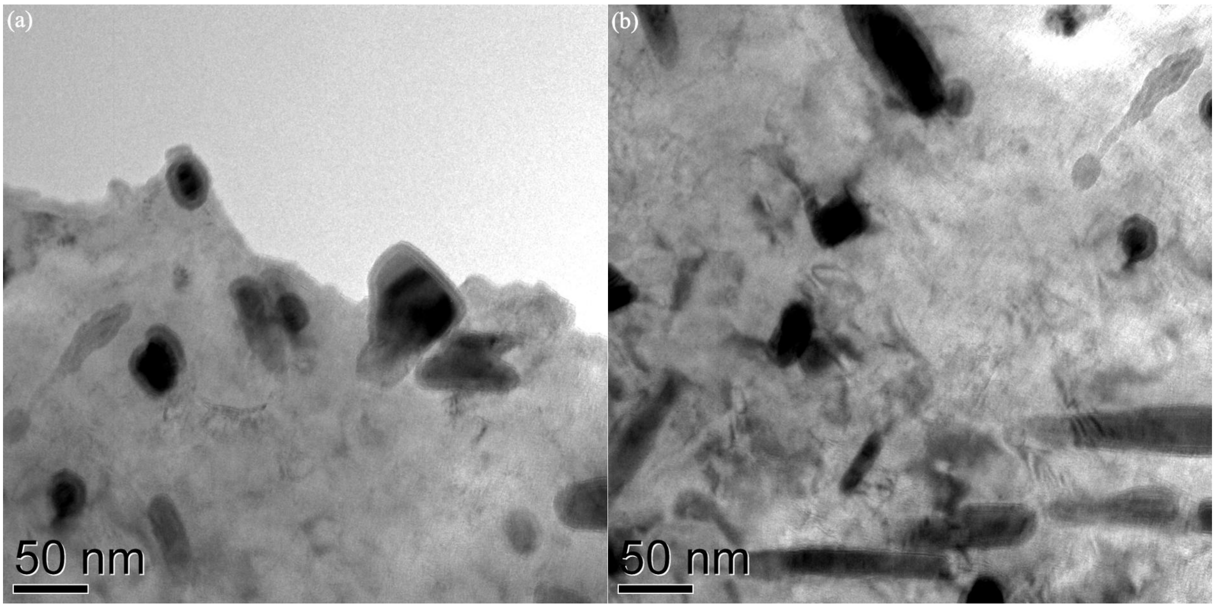

Figure 5: TEM bright field images of sample 11, annealed at 700°C for 60 sec. a) and b) represent different foils of the same condition.

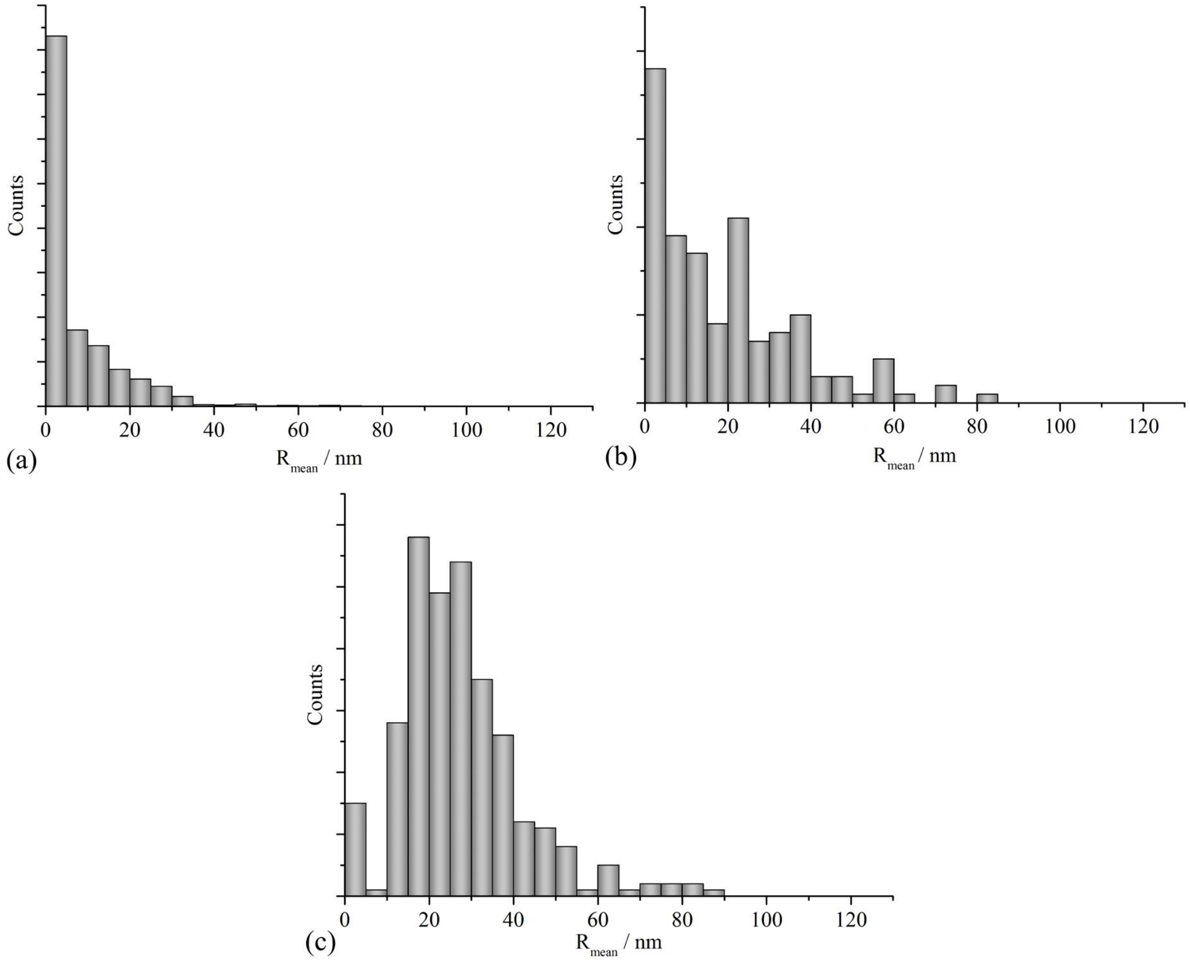

Figure 6: Size distribution of the samples tempered at 700°C for (a) 1 min, (b) 10 min and (c) 1 hr.

The crystal structure of the cementite particles is confirmed with selected area diffraction (SAD) patterns. The chemical composition is determined with EDX-measurements on the thin foils. The diagram in figure 7 displays the results of these measurements in terms of the Cr/Fe-ratio. This is done to facilitate comparison with the simulation results. For reference, a solid line is drawn at the 'nominal' Cr/Fe-ratio. The results clearly show that the Cr/Fe-ratio at the lowest temperature is practically identical to the nominal ratio, indicating that the precipitates are formed by only diffusion (partitioning) of C and that no Cr-enrichment occurs within one hour of annealing. At the highest temperature, Cr-enrichment is evident already after short-time heat treatment, with increasing Cr/Fe ratio with longer tempering duration.

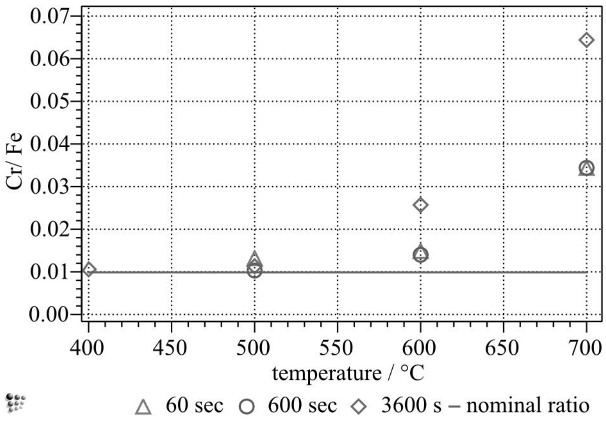

Figure 7: Measured Cr/Fe ratios of cementite precipitates vs. temperature (results of the EDX-measurements); tempering times: triangles … 1min; circles … 10min; diamonds … 1hr; solid line … nominal Cr/Fe

5.2 Results of the parameter study

The parameter study summarized in figure 8 investigates the influence of different values of the exponent *n* of the coefficient α in eq. 5 on the precipitate evolution. Figure 8b shows details of the calculated mean radius evolution for varying *n*-values between 0 and 2.5 for tempering at 700C. Up to approximately 20s simulation time, corresponding to the quenching process and subsequent heating to annealing temperature, the simulation predicts that the influence of *n* is negligible. Figure 8d, showing the evolution of the Cr content of the matrix, indicates that this is due to the fact that the matrix chemical composition remains constant for the substitutional elements. Note that the slight increase of the matrix Cr-content at around t = 8s is an artefact stemming from the increase in precipitate phase fraction containing a higher C mole fraction than the surrounding. The Cr mole fraction in cementite is consequently lower than the one in the matrix and the matrix Cr mole fraction thus higher due to mass conservation. This effect comes from the choice of variables, therefore, and does not correspond to a real Cr-enrichment. The Cr/Fe ratio remains identical up to this stage in both phases.

With the onset of coarsening, the impact of α becomes pronounced. As long as the driving force for precipitation is high due to high supersaturation in C, the thermodynamic extremum principle predicts a maximum entropy production by mere growth of the precipitates with Cr/Fe practical identical in cementite and matrix. From the moment on, when the matrix C content approaches its equilibrium value, the driving force decreases rapidly and cementite growth seizes. At this point, the precipitates have reached a mean size (radius) of around 30nm and two processes compete in the entropy production process:

Enrichment of precipitates with Cr and further reduction of the matrix C content by coarsening with accompanying reduction of precipitate/matrix interfacial area.

The coarsening rate decreases with increasing α-values and, starting with n=1.5, the calculated mean radius runs into a plateau. As a result, the mean particle size is reduced with increasing α, whereas the number density remains on a higher level, since Ostwald ripening of the particles is progressively suppressed (figure 8c). Figure 8d summarizes the Cr-content evolution in the matrix compared to the nominal Cr-content. With increasing α-value, the Cr-content of the particles is increased. As a consequence, the matrix becomes Cr-depleted faster with increasing α.

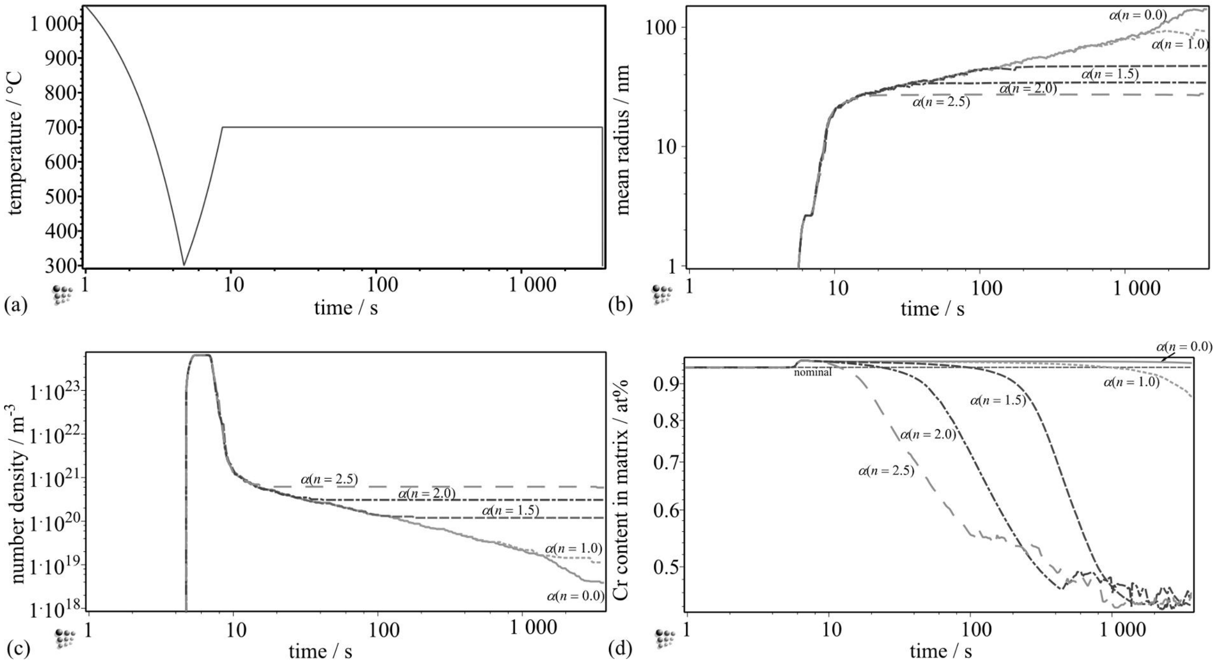

Figure 8: a) Time-temperature profile used in the parameter study, where the exponent n of the coefficient α is varied between 0 and 2.5. b) Calculated mean radius of the cementite particles with lath boundaries as nucleation site. c) Number density of the cementite precipitates. d) Cr-content of the matrix.

5.3 Validation of the simulation

In the last part of this study, the simulation results are validated against the experimental data. The two plots in figure 9 show the calculated mean radii and number density of the “lath-boundary” cementite population for all annealing temperatures for α with n = 2.

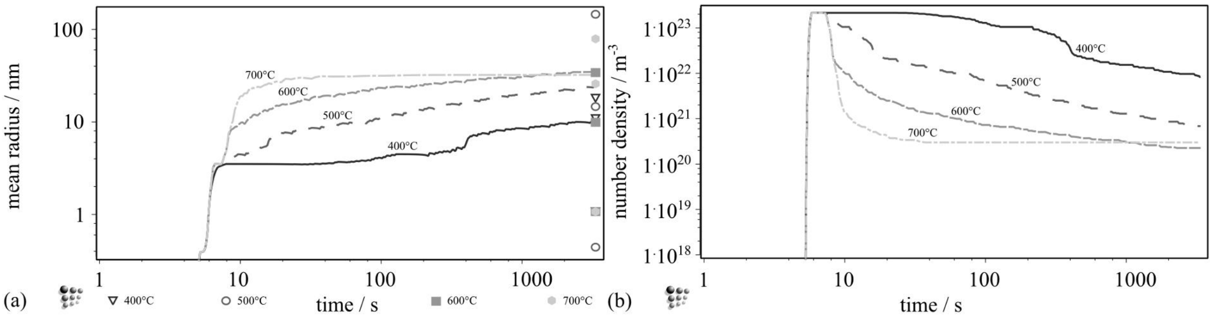

Figure 9: a) Calculated mean radii of the “lath-boundary” cementite population. The symbols represent the measured minimum, mean and maximum radius of the particles after one hour at 400°c, 500°C, 600°C and 700°C. b) calculated number density of the particles after annealing.

The symbols in figure 9a display the measured minimum, mean and maximum particle radii after one hour of tempering at temperatures between 400 and 700°C. Qualitatively, the calculated radii agree reasonably well with the experimental mean values in terms of the observed size range, although a more detailed comparison is impaired by the substantial scatter of the experimental values (see also the size distributions shown in figure 6). Nevertheless, the figure clearly emphasizes the impact of Cr enrichment of the cementite precipitates on the size evolution at different temperatures. At 400°C, the evolution is mainly determined by coarsening of precipitates with para-composition, i.e., with identical Fe/Cr ratio in precipitate and matrix. With increasing temperature, we observe a gradual enrichment with Cr until coarsening becomes very sluggish at 700°C and the radius increase almost shows a plateau. The corresponding number density of precipitates is summarized in figure 9b. The precipitate evolution is finally examined in detail for both cementite populations at dislocations and lath boundaries after tempering at 700°C.

The lines in figure 10 represent the calculated mean radii of the cementite population nucleated at lath boundaries (dash-dotted line) and at dislocations (solid line) with $\alpha(n = 2)$ together with experimental data. The triangles correspond to the minimum, the mean and the maximum measured radii of the particles.

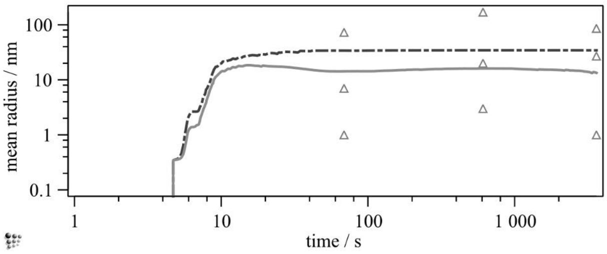

Figure 10: Comparison between the calculated mean radii with $\alpha(n = 2)$ for both cementite populations with the experimentally measured particle radii of the samples 11, 12 and 13 (tempered at 700°C for 1 min, 10 min and 1 hr).

The mean radii of the cementite populations differ due to the different shape factors applied in the simulation as well as different assumed diffusivities. For the analysis of particle size, we do not distinguish between different nucleation sites. However, the agreement between calculated mean radii of both cementite populations and the mean measured radii is satisfying and, most important, the apparent stasis in the size evolution as observed in the experiment is well reproduced by our new simulation methodology.

The last issue discussed in this section is the evolution of the mean Cr-content of the particles. Figure 11 summarizes these results in the form of a surface plot of the Cr/Fe ratio of the cementite particles nucleated at lath boundaries. The symbols indicate the measured values.

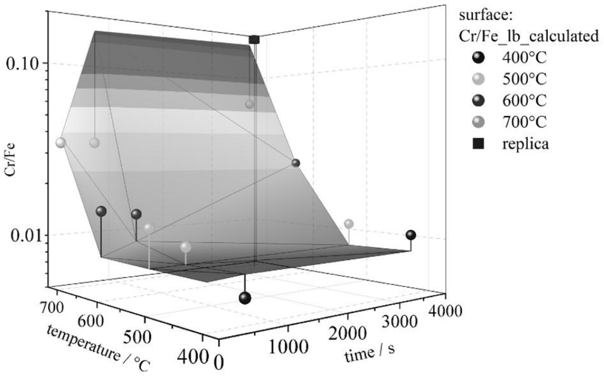

Figure 11: Comparison between measured Cr/Fe-relation of the precipitates (symbols) and the calculated values of lath boundary cementite precipitates at different times and temperatures (surface).

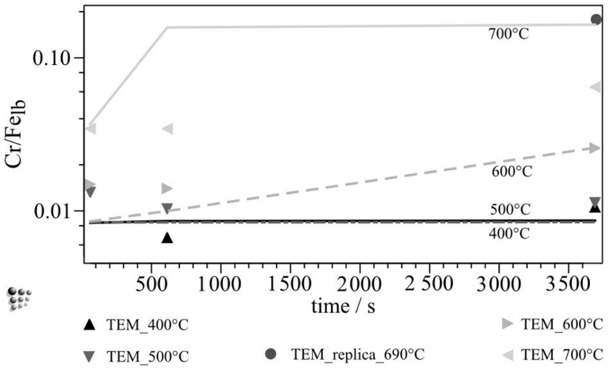

Figure 12: Comparison between measured Cr/Fe-ratio of the precipitates (symbols) and the calculated values of lath boundary cementite precipitates.

The increasing Cr-content of the particles with temperature and time is reflected well by the simulation with minor differences between calculated and measured values. We do not consider these as substantial because there are several issues that might be the source of these differences. First, only a limited number of measurements have been performed at lower temperatures and short tempering times, which lead to larger error bars in these data. Second, the EDX-measurements performed in the present work have been performed on TEM thin foils. Consequently, the EDX signal also contains information about the chemical environment (steel matrix) of the precipitates, thus introducing some uncertainty. As a reference, the results from previous work on material of comparable chemical composition are also added in the figure (filled circle in figure 12). This Cr/Fe-ratio was determined on carbon rextraction replica and the mean value of this analysis is in good quantitative aggreement with our calculations.

6. Summary

In the present work, the precipitation kinetics during tempering of martensite is investigated experimentally and with computational means. Special emphasis is put on the evolution of size and chemical composition of cementite precipitates at different times and temperatures. A new simulation methodology is developed where (i) the nucleus composition of cementite precipitates is calculated on basis of the minimum nucleation barrier concept and (ii) a new method for computational treatment of the evolution of the chemical composition of the cementite particles is developed where the diffusion coefficient inside the precipitate is modified such that the effect of a small reaction layer on the precipitate surface can be incorporated. In this way, the experimentally observed enrichment of the cementite precipitates with slower diffusing elements, such as Cr in the present case, can be well reproduced and the evolution of size and chemical composition of cementite particles can be simulated over the entire temperature range with satisfying correspondence to the experimental data.

Appendix A

In this section, further details are given to provide full information about the input parameters used in the simulations.

A.1. Potential nucleation sites

For quantification of potential nucleation sites, martensite lath boundaries are treated as subgrain boundaries in MatCalc. They are different to (prior austenite) grain boundaries, since they are low-angle boundaries inside a high-angle boundary grain structure and they provide faster diffusion paths compared to the matrix, but they are slower compared to the diffusion paths at grain boundaries. For precipitate nucleation at subgrain boundaries, we assume that each atom located on the boundary acts as a potential nucleation site. The number of nucleation sites is evaluated from the geometrical model of an array of elongated tetrakaidecahedrons, as described, e.g., in Ref. [14]. The essential parameter is then the “subgrain size”, where a mean value for the martensite laths from the experiments is taken (0.2µm, elongation factor 20).

For nucleation at dislocations, we assume that each single atom along the dislocation core represents a potential nucleation site and with the dislocation density ρ, the number of nucleation sites is N_{disl} [14]

$$N_{\mathrm{disl}} = \frac{\rho}{a} , \qquad (A.1)$$

where a is the mean atomic distance.

A.2. Evaluation of precipitate nucleation rates

In table A.2.1, the essential expressions for evaluation of the nucleation rate, J, in a multicomponent environment are summarized. Details are given in ref. [14].

Table A.2.1: Quantities and expressions used in the evaluation of the nucleation rate, J, in multicomponent systems [14].

Quantity/ (dimension)	description	Expression	comment
Z (dimensionless)	Zeldovich factor	$Z = \left[-\frac{1}{2\pi k_B T} \left(\frac{\partial^2 \Delta G_{\mathrm{nucl}}}{\partial n^2} \right)_{n^*} \right]^{1/2}$	
ΔG_{nucl} (J)	Cluster formation energy	$\Delta G_{\mathrm{nucl}} = \frac{4}{3}\pi\rho^3 \cdot \Delta G_{\mathrm{vol}} + 4\pi\rho^2 \cdot \gamma$	ρ ... cluster radius
ρ^* (m)	critical radius	$-\frac{2\gamma}{\Delta G_{\mathrm{vol}}}$ (spherical)	
ΔG_{vol} (J/m³)	volume free energy change	$-\frac{d^{\beta}_{\mathrm{chem}}}{v^{\alpha}} + \Delta G^{\mathrm{el}}_{\mathrm{vol}}$	$d^{\beta}_{\mathrm{chem}}$ ... chemical driving force; $\Delta G^{\mathrm{el}}_{\mathrm{vol}}$ ... elastic energy associated with the elastic stress field around an ellipsoidal inclusion; v^{α} ... molar volume
γ (J/m²)	surface free energy/ interfacial energy	$\frac{n_S \cdot z_{S,\mathrm{eff}}}{N_A \cdot z_{L,\mathrm{eff}}} \cdot \Delta h_{\mathrm{sol}}$	n_S ... number of atoms per unit area of interface; $z_{S,\mathrm{eff}}$ ... effective number of broken bonds across the interface; $z_{L,\mathrm{eff}}$ ... effective coordination number; Δh_{sol} ... enthalpy of solution; N_A ... Avogadro's number
τ (s)	incubation time	$\tau = \frac{1}{2\beta^* Z^2}$	β^* ... atomic attachment rate (eq. 2)

A.3. Model for the dislocation density evolution

The model for evolution of the dislocation density is based on the work of Roters et al. [59] and Sherstnev et al. [47]. The corresponding equations are summarized in Table A.3.1.

Table A.3.1: Model for the total dislocation density evolution.

Quantity/ (dimension)	description	equation	explanation
$\dot{\rho} = \frac{d\rho}{dt}$ ($\mathrm{m^{-2}s^{-1}}$)	general law for the evolution of dislocation density	$\dot{\rho} = \dot{\rho}^{+} - \dot{\rho}^{-}$	$\dot{\rho}^{+}$ ...production term $\dot{\rho}^{-}$ ...annihilation term
$\dot{\rho}^{+}$ ($\mathrm{m^{-2}s^{-1}}$)	Athermal dislocation storage of moving dislocations	$\dot{\rho}^{+} = \frac{1}{b \cdot L} M \cdot \dot{\varphi}$	M...Taylor factor [2.5 ... 3.1]; b...Burgers vector; $\dot{\varphi}$ ... plastic strain rate
L(m)	L ... mean free path of the moving dislocations	$L = \frac{A}{\sqrt{\rho}}$	ρ ... total dislocation density; $A \approx 10..100$ parameter describing the effectiveness of dislocation storage
$\dot{\rho}^{-}_{\mathrm{glide}}$ ($\mathrm{m^{-2}s^{-1}}$)	Contribution from dynamic recovery	$\dot{\rho}^{-}_{\mathrm{glide}} = -2 \cdot B \cdot \frac{d_{\mathrm{ann}}}{b} \cdot \rho \cdot M \cdot \dot{\varphi}$	$B \approx 2..5$ dislocation annihilation coefficient; d_{ann}...critical distance where annihilation is possible
d_{ann} (m)	critical distance	$d_{\mathrm{ann}} = \frac{Gb^4}{2\pi(1-\nu)E^{\mathrm{f}}_{\mathrm{v}}}$	G...Shear modulus; n...Poisson's ratio; $E^{\mathrm{f}}_{\mathrm{v}}$ ...vacation formation energy
$\dot{\rho}^{-}_{\mathrm{climb}}$ ($\mathrm{m^{-2}s^{-1}}$)	Contribution from static recovery	$\dot{\rho}^{-}_{\mathrm{climb}} = -2 \cdot C \cdot D_{\mathrm{d}} \cdot \frac{Gb^3}{k_{\mathrm{B}}T}\left(\rho^2 - \rho^2_{\mathrm{eq}}\right)$	k_{B}...Boltzmann constant; T...temperature; ρ_{eq}...dislocation density in the undeformed material $C \approx 1 \cdot 10^{-3}..1 \cdot 10^{-6}$ dislocation annihilation coefficient
D_{d} ($\mathrm{m^{2}s^{-1}}$)	Self-diffusion coefficient	$D_{\mathrm{d}} = \alpha_{\mathrm{d}} \cdot D_{\mathrm{b}}$	D_{b}...bulk diffusivity; temperature-dependent factor α_{d} [42]

The calculated evolution of the martensite dislocation density during the annealing processes is shown in figure A.3.1.

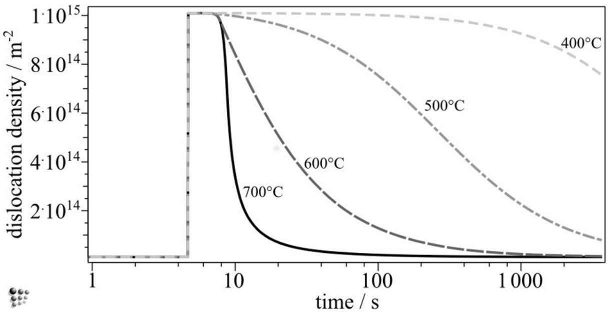

Figure A.3.1: Evolution of the martensite dislocation density during heating to annealing temperature and annealing itself.

7. References

[1] Lopez Turconi G, Echaniz G, Anelli E, Scoppio L, Cumino G, Perez T and Morales C 2001 *Corrosion 2001* (Houston / TX / USA) Paper No. 01077

[2] Khani Sanij M H, Ghasemi Banadkouki S S, Mashreghi A R and Moshrefifar M 2012 Materials and Design Vol. 42 339-46

[3] Speich G R and Leslie W C 1972 Metall. Mater. Trans. A Vol. 3A 1043-54

[4] Thomson R C 2000 Mater. Charact. Vol. 44 219-33

[5] Ghosh G and Olson G B 2002 Acta Mater.Vol. 50/8 2099-119

[6] Ghosh G, Campbell C E and Olson G B 1999 Metall. Mater. Trans. A 30A 501-12

[7] Ohmura T, Hara T and Tsuzaki K 2003 Scripta Mater. 49 1157-62

[8] Jung M, Lee S J and Lee Y K 2009 Metall. Mater. Trans. A 40A 551-9

[9] Honeycombe R W K 1974 Climax Molybdenum Company Publication (CO. LTD., London, UK)

[10] Coates D E 1973 Metall. Mater. Trans. Vol. 4 2313-2325

[11] Sietsma J and van der Zwaag S 2004 Acta Mater. Vol. 52 4143-52

[12] Liu Z K, Höglund L, Jönsson B and Agren J 1991 Metall. Mater. Trans. A Vol. 22A 1745-52

[13] Song W, Choi P P, Inden G, Prahl U, Raabe D and Bleck W 2014 Metall. Mater. Trans. A Vol. 45A 505-606

[14] Kozeschnik E 2013 Modelling Solid-State Precipitation (New York, USA: Momentum Press, LLC)

[15] Thomson R C and Miller M K 1995 Appl. Surf. Sci. 87/88 185-93

[16] Babu S S, Hono K and Sakurai T 1994 Metall. Mater. Trans. A 25A 499-508

[17] Hillert M and Agren J 2004 Scripta Mater. Vol. 50 697-9

[18] Kozeschnik E 2000 Calphad Vol 24 495-502

[19] Miyamoto G, Oh J C, Hono K, Furuhara T and Maki T 2007 Acta Mater. 55 5027-5038

[20] Woodhead J H and Quarrell A G 1965 J. Iron Steel Inst. Vol. 203 605-20

[21] Hultgren A 1946 Trans. ASM Vol. 39 915-1005

[22] Zamberger S and Kozeschnik E 2012 Mater. Sci. Forum Vols. 706-709 1586-91

[23] Zamberger S, Wojcik T, Klarner J, Klösch G, Schifferl H and Kozeschnik E 2013 Steel Res. Int. Vol. 84 20-30

[24] http://matcalc.at

[25] Kampmann R and Wagner R 1984 Decomposition of alloys, the early stages Proc. of the 2nd Acta-Scripta Metallurgica Conference (Oxford / UK) 91-103

[26] Onsager L 1931 Phys. Rev. I 37 405-26
Onsager L 1931 Phys. Rev. II 38 2265-79

[27] Svoboda J, Turek I and Fischer F D 2005 Philos. Mag. Vol. 85 3699-707

[28] Svoboda J, Fischer F D, Fratzl P and Kozeschnik E 2004 Mater. Sci. Eng. A 385 166-74

[29] Kozeschnik E, Svoboda J, Fratzl P and Fischer F D 2004 Mater. Sci. Eng. A 385 157-65

[30] Kozeschnik E, Svoboda J and Fischer F D 2005 CALPHAD 28 379-82

[31] Janssens K G F, Raabe D, Kozeschnik E, Miodownik M A and Nestler B 2007 Computational Materials Engineering – An Introduction to Computational Microstructure Evolution of Polycrystalline Materials (Oxford, UK: Elsevier Academic Press)

[32] Sonderegger B and Kozeschnik E 2009 Metall. Mater. Trans. A Vol. 40A 499-510

[33] Sonderegger B and Kozeschnik E 2009 Scripta Mater. 60 635-8

[34] Kozeschnik E 2008 Scripta Mater. 59 1018-21

[35] Volmer M and Weber A 1926 Z. Phy.Chem. 119 277-301

[36] Becker R and Döring W 1935 Ann. der Physik 24 719-52

[37] Russell K C 1980 Adv. Colloid. Interfac. Vol. 13 205-318

[38] Fischer F D, Svoboda J and Petryk H 2014 Acta Mater. 67 1-20

[39] Sonderegger B, Kozeschnik E, Leitner H, Clemens H, Svoboda J and Fischer F D 2008 Int. J. Mater. Res. 99/4 410-415

[40] Schaffer R, Albu M, Kothleitner G, Pölt P and Kozeschnik E 2009 Acta Mater. 57 5739-47

[41] Holzer I and Kozeschnik E 2010 Mater. Sci. Forum Vols. 638-642 2579-84

[42] Radis R and Kozeschnik E 2010 Modelling Simul. Mater. Sci. Eng. 18 055003

[43] Pudar M, Zamberger S, Spiradek-Hahn C, Radis R and Kozeschnik E 2010 Steel. Res. Int.81 372-80

[44] Radis R and Kozeschnik E 2010 Steel Res. Int.81 681-5

[45] Radis R, Schwarz S, Zamberger S and Kozeschnik E 2011 Steel Res. Int. 82 905-10

[46] Sherstnev P, Lang P and Kozeschnik E 2012 Proc. of 6th European Congress on Computational Methods in Applied Sciences and Engineering (Vienna, Austria) e-Book Full Papers [3-9503537-0-4] 5331-38

[47] Hull D and Bacon D J 1992 Introduction to Dislocations (Oxford / UK: Pergamon Press, Ltd.)

[48] Garcia-Mateo C, Caballero F G, Capdevila C and Garcia De Andres C 2009 Scripta. Mater. 61 855-8

[49] Kim B, Celada C, San Martin D, Sourmail T and Rivera-Díaz-del-Castillo P E J 2013 Acta Mater. 61 6983-92

[50] Caron R N and Krauss G 1972 Metall. Mater. Trans. A Vol. 3A 2381-9

[51] Airey G P, Hughes TA and Mehl R F 1968 Trans. AIME Vol. 242 1853-63

[52] Furuhara T, Kobayashi K and Maki T 2004 ISIJ Int. Vol. 44 1937-44

[53] Radis R and Kozeschnik E 2012 Modelling Simul. Mater. Sci. Eng. 20 055010

[54] Stechauner G and Kozeschnik E 2014 CALPHAD 47 92-9

[55] Kozeschnik E, Svoboda J and Fischer F D 2006 Mat. Sci. Eng. A. 441 68-72

[56] Thomas G 1978 Metall. Mater. Trans.A Vol. 9A 439-50

[57] Sonderegger B and Kozeschnik E 2010 Metall. Mater. Trans. A Vol. 41A 3262-9

[58] Rasband W National Institutes of Health USA: http://imagej.nih.gov/ij

[59] Roters F, Raabe D and Gottstein G 2000 Acta mater. 48 4181-9

Paper five

Long-range diffusion of H in the presence of traps in a microalloyed steel

Zamberger S, Lang P, Klösch G,
Klarner J and Kozeschnik E

Comput. Mater. Sci.
doi:10.1016/j.commatsci.2015.11.014

Long-range diffusion of H in the presence of traps in a microalloyed steel

S Zamberger[1], P Lang[2], G Klösch[1], J Klarner[3], E Kozeschnik[4]

[1]voestalpine Stahl Donawitz GmbH, Kerpelystrasse 199, A-8700 Leoben, Austria

[2]Department of Materials Science and Metallurgy University of Cambridge, 27 Charles Babbage Rd, Cambridge CB3 0FS, UK

[3]voestalpine Tubulars GmbH & Co KG, Alpinestraße 17, A-8652 Kindberg, Austria

[4]Christian Doppler Laboratory of Early Stages of Precipitation, Institute of Materials Science and Technology, Vienna University of Technology, Favoritenstrasse 9, A-1040 Vienna, Austria

Abstract. In the present work, we apply a new model for trapping of interstitial elements at various types of atomic traps to investigate the H-trapping efficiency of different kinds of precipitates in a microalloyed steel grade. The model is briefly introduced and reviewed. The trapping strength representative for the different stages of the precipitation process is evaluated, as well as the influence of size and shape of the particles on the trapping capacity. The significant impact of the applied trapping energies between precipitate interface and H-atoms is discussed. On basis of the present work, the considerable scatter of experimental H-diffusion data at low temperatures is straightforwardly explained and quantitatively reproduced in the simulations.

1. Introduction

The oil industry is more and more going into exploitation of sour oil reservoirs and gas fields that contain increasing amounts of H_2S, thus increasing the potential for stress corrosion cracking of the container materials (pipes, vessels etc.). An important feature related to this phenomenon is the attachment of hydrogen atoms at localised trapping sites inside the material. In complex microstructures, trapping of H can substantially impact its long-range diffusion kinetics and alter its solubility and chemical potentials. Several investigations showed that microstructural features, such as, grain boundaries, subgrain boundaries, dislocations, but also impurity elements in solid solution and interfaces of precipitates can act as potential trapping sites for diffusing H-atoms [1-6].

Experimentally, H-diffusion and H-trapping effects have been investigated numerous times on basis of permeation measurements [7-20], thermal desorption [12,16,21-28], high resolution tritium autoradiography [29-31], thermal analysis [4,32] and the microprint technique [33,34]. For steel, the experimental results are sometimes contradictory with respect to the effect of secondary phase particles acting as H-traps, on one hand, and in the question, whether these are harmful or not in terms of H-induced embrittlement. For instance, in ref. [8], different microstructures have been investigated on basis of permeation measurements, with the conclusion that the permeation coefficient differs significantly in pearlite, martensite and bainite, but carbide precipitation in tempered martensite does not influence the permeation coefficient significantly. Similar results are reported in refs. [9,19]. In contrast, Valentini et al. [10] find that Ti in solution as well as Ti(C,N) act as potential trapping sites in a microalloyed steel in hot rolled condition. Other reports confirm this trapping effect of Ti-particles [1,2,22,24,35-36].

Mo-rich M_2C carbides are often identified as strong H-traps [6,12,29,37], similarly to other Cr- and Mo-rich particles [6,20,37]. With regard to the detrimental effect of, e.g., Mo-rich precipitates, Mendibide and Sourmail [20] conclude that there exists a critical Mo-content of 0.75wt%, above which no fine Mo-rich M_3C and MC type precipitates form, but coarse M_2C and M_6C carbides, which are supposed to be harmful with respect to H-embrittlement.

Reports on the effect of V and Nb are rather scarce. Charbonnier et al. [29] observe that the addition of V in combination with Mo and Ti leads to the precipitation of finely dispersed MC-type particles, which he designates as "*good traps*" for H. Spencer and Duquette [38] also indicate that V-carbides act as beneficial traps. Yokota and Shiraga [39] and Asahi et al. [40] demonstrate that V-precipitates trap H in tempered martensitic steel. Lopez Turconi et al. [41] investigated a Nb-alloyed (0,020-0,035wt%) Cr-Mo steel and first evidenced that, due to fine MC precipitates, the prior austenite grain boundary size is refined, which leads, among other factors, to an improved sulphide stress cracking resistance. Positive effects of Nb additions on the stress cracking resistance of the material are also reported in ref. [20].

On the computational side, Oriani [42] and McNabb and Foster [43] presented seminal work on H-trapping. Their models are based on the assumption that different kinds of traps with respect to their trapping capacity are present in the material. Following the proposal of McNabb and Foster, there exist three categories of traps: (i) shallow traps with so low trapping energy for the H-atoms that there impact on diffusivity is negligible, (ii) deep traps with so high trapping energy that H-atoms bound there do not longer contribute to the diffusion process, since the trapping effect is of quasi permanent nature, and (iii) intermediate traps with binding energies to H in just the right magnitude such that H atoms become temporarily trapped and the diffusion process of H through the material can be potentially hindered [43]. Examples can be found in ref. [35], where the McNabb-Foster model is applied for calculation of the irreversible trapping parameters and the Oriani approach for the calculation of the interaction energy between the trapping sites and H atoms.

Svoboda and Fischer [44-46] recently generalized the problem in terms of a concentration and site fraction based formulation. Their model describes the distribution of H atoms between lattice and trap sites starting from a local thermodynamic equilibrium condition also allowing for multiple sorts of traps simultaneously [46,47]. Further details on the model and its application are given below.

In the present work, the numerical simulation of precipitation kinetics is performed with the thermo-kinetic software MatCalc [48]. In this approach, the size-class oriented Kampmann-Wagner [49] approach is realized, in combination with an extended classical nucleation theory for homogeneous and heterogeneous nucleation in multi-component systems [50-52]. For the derivation of the evolution equations for the radius and chemical composition of the precipitates, the thermodynamic extremum principle is utilized [53-57]. Examples for MatCalc application to various precipitation problems are given in, e.g., [58-62]. Other computer codes for the treatment of precipitation kinetics are, e.g., DICTRA [63], PrecipiCalc [64], PanPrecipitation [65] or TC-Prisma [66]. Chapter 9 in Ref. [67] provides an overview of these codes together with an assessment of their potential field of application. Although these software codes can deal with either long-range diffusion, e.g., DICTRA, or precipitation kinetics, none of them combines these two aspects in a single simulation together with a suitable hydrogen trapping framework.

In the present work, for the first time, we fill this gap by utilizing a powerful precipitation kinetics simulation environment (MatCalc) in combination with the numerical analysis of long-range diffusion in the presence of H trapping. Main focus is the computational analysis of H-trapping in microalloyed steel. With the aid of parameter studies, the influence of the trapping energy between the interfaces of precipitates and H on the trapping effect is shown, the correlation between the precipitate distribution and morphology, which is determined by size, number density and shape, and the trapping efficiency is analysed. A comparison of calculated diffusion coefficients with respect to different trapping sites is given in the last section of the simulation results chapter.

For the analysis of H-trapping, the model recently developed by Fischer et al. [44] as implemented in the thermo-kinetic software package MatCalc (vers.5.61rel.057) [48] is used. The model, explained below in more detail, describes the trapping behaviour of interstitial atoms (here: H) in a system containing different kinds of traps based on the assumption of local thermodynamic equilibrium between the trap and lattice atoms. With the aid of this model, conclusions are elaborated with respect to the design of optimum microstructures for minimal susceptibility for H-induced stress corrosion cracking.

2. Material

The present steel can be classified as a medium-C steel grade with Cr and Mo as main alloying elements and with microalloying additions of Nb, Ti and V (table 1). The material is continuously cast into cylindrical dimension with *d* = 230mm. The blooms are reheated to 1300°C and afterwards rolled into seamless tubes. The temperature profile for the rolling process is given in Figure 1. The tubes are quenched and tempered (Q&T) twice with the aim of producing a fine and homogenous microstructure.

Table 1: Chemical composition of the steel (wt%).

C	Si	Mn	Cr	Mo	Al	Ti	V	Nb	N
0.24	0.29	0.34	0.95	0.78	0.036	0.017	0.036	0.065	0.005

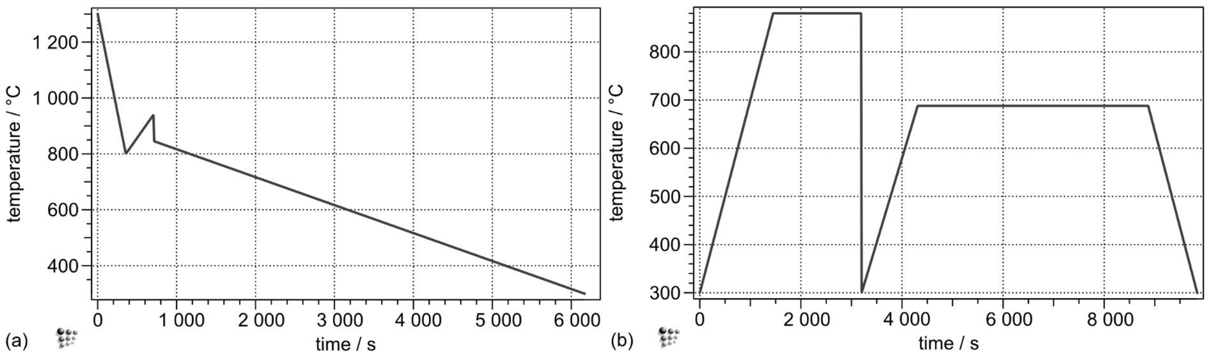

Figure 1: Simplified time-temperature profiles of the rolling process (a) and the quench and tempering treatment (b).

3. Precipitation kinetics simulation

With our computer simulation, we aim at (i) describing the precipitation kinetics of carbo-nitrides in the production process in a first independent step as well as (ii) reproducing the long-range diffusion of hydrogen with the morphology of these secondary phase particles as starting condition in a subsequent H exposure simulation. The precipitation processes along the entire production chain comprising of casting, pre-heat treatment and thermo-mechanical finishing are accounted for in the precipitation simulations. The results are taken as the microstructural starting point for the H-trap analysis, where we evaluate the evolution of the long-range H diffusion field in the presence of NbC, TiN and M_7C_3 precipitates.

The precipitation kinetics analysis is performed on basis of the procedure developed in earlier work [68]. For the sake of simplicity and reduction of computational time, the chemical composition of the steel given in Table 2 is used in the simulation of H-diffusion. The time-temperature profile given in Figure 1 is the basis for the simulation of the precipitation kinetics.

Table 2: Chemical composition of the steel as used in the simulations.

	C	Cr	Mo	Ti	Nb	N	H
wt%	0.24	0.95	0.78	0.017	0.065	0.006	$1.00 \cdot 10^{-6}$
at%	1.13	1.01	0.45	0.020	0.039	0.022	$5.50 \cdot 10^{-5}$

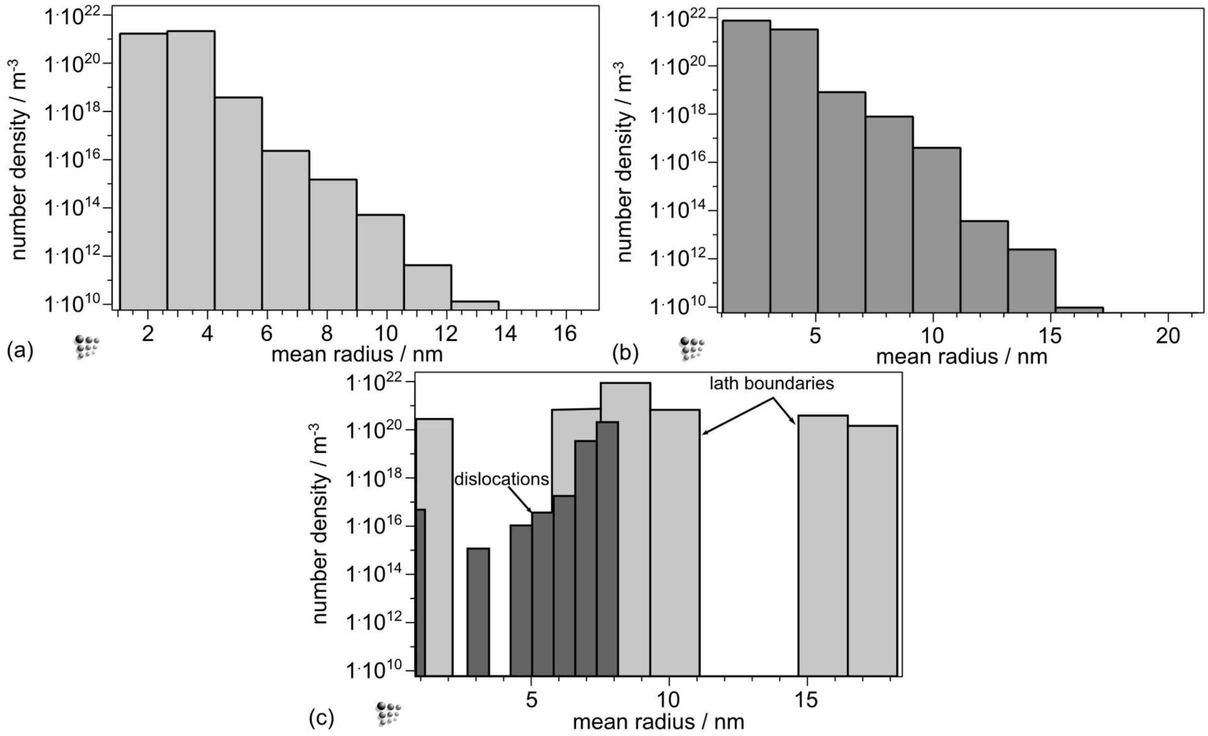

Figure 2: Results of the numerical simulation of the precipitation kinetics after the second Q&T treatment. Precipitate distribution plots for (a) TiN, (b) NbC and (c) M_7C_3 (nucleated at dislocations and lath boundaries).

The precipitate size distributions obtained in the thermo-kinetic simulations after the second Q&T treatment are summarized in Figure 2. For the simulation of the long-range diffusion of hydrogen, the information about size, number density and chemical composition of precipitates is transferred into the simulation cells of the MatCalc [48] diffusion module. The long-range diffusion process is evaluated on basis of the formalism developed for multi-component diffusion analysis [67,69] and solved numerically utilizing a finite differences scheme. In the simulations, the diffusion module is fully coupled to the precipitation kinetics module, where both, the evolution of precipitates as well as the distribution of lattice (free) H and H trapped at these sites are evaluated synchronously to the long-range diffusion of free H in the ferrous matrix. The theoretical basis of the trapping model and the evaluation of effective diffusion coefficients in the presence of traps are outlined below.

4. The model

Fischer et al. [45] and Svoboda et al. [46] have recently developed a model describing the trapping behaviour of H atoms in a system containing different kinds of traps based on the assumption of local thermodynamic equilibrium between the traps and the lattice. In the model, the interstitial sublattice is separated into ‘normal’ interstitial lattice positions and ‘trapped’ positions. Fick’s first law for the diffusional flux was then applied for the description of the concentrations c_L and c_{Tk}, which are the concentrations of H in the lattice and at the trapping sites k, respectively [44]. With these quantities obtained from solution of the evolution equations derived in refs. [44-46], it is possible to determine the chemical diffusion coefficient as

$$\tilde{D} = \frac{D}{2}\left(1 + \frac{cV_L(1-K) - {}^{V_L}\!/_{V_T} + K}{\sqrt{\left(cV_L(1-K) - {}^{V_L}\!/_{V_T} - K\right)^2 + 4cV_L K(1-K)}}\right). \tag{1}$$

D is the tracer diffusion coefficient of the interstitial component in the trap-free lattice. The relation $\tilde{D}/D$ depends on the molar concentration of the interstitial component, c, being the sum of c_L and c_{Tk}, the molar volumes of lattice positions V_L and trap positions V_T and the equilibrium constant K. V_L refers to one mole of interstitial positions in the lattice which can be occupied by freely diffusing interstitial element (lattice position) and V_T to one mole of interstitial positions which are regarded as trap positions [44]. K is given by

$$K = \exp\left(-\frac{\Delta E}{RT}\right), \tag{2}$$

where ΔE is the trapping energy in $\mathrm{Jmol^{-1}}$, R is the ideal gas constant (8.31447 $\mathrm{Jmol^{-1}K^{-1}}$) and T the temperature in K.

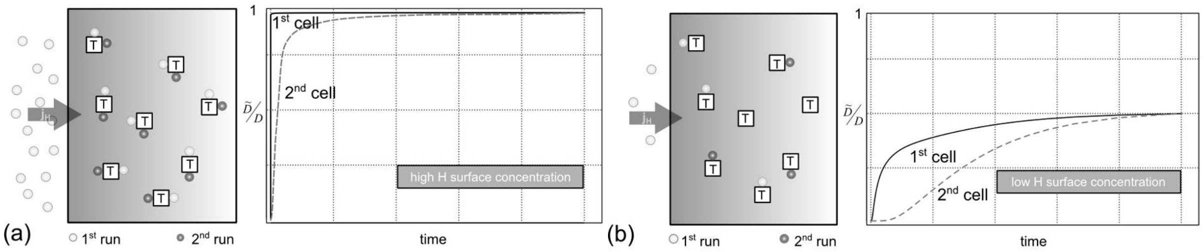

Figure 3: Sketch for the influence of the H-concentration at the surface on the trapping kinetics in the material. The curves show the trapping effect ($\tilde{D}/D$) from left to the right of the sample (see text for discussion).

The sketch given in Figure 3 illustrates the effect of the molar concentration of H at the surface on the trapping kinetics inside the material. The driving force for the diffusion process stems from the concentration gradient between the surface and the bulk material. In Figure 3a, the simulation conditions for high H-concentration at the surface are indicated. H-atoms diffuse into the bulk material and, due to their high concentration the available traps are filled rapidly. The traps considered here are the interfaces of the secondary phase particles. The H atoms entering from the surface next cannot be trapped any more due to a saturation of the available trapping sites. Consequently, the ratio $\tilde{D}/D$ increases quickly to a maximum value of ~ 1, which means that there is nearly no retardation of H-diffusion in the corresponding part of the material. In Figure 3b, the surface concentration of H is comparably lower and, after a first charging of the bulk material with H, there are still unoccupied traps available. The quotient $\tilde{D}/D$ is, therefore, small and the fewer H-atoms entering the bulk volume from the surface are efficiently trapped for a certain time.

5. Simulation setup for hydrogen diffusion

The simulation of simultaneous long-range diffusion of H and carbide precipitation strongly depends on local conditions and it is, therefore, performed with spatial resolution. In our simulations, the diffusion-sample is represented by 20 equally sized cells spanning a length of 2.1 mm. This geometry corresponds to the experimental conditions present in the permeation tests performed in a companion research project. The simulation is performed in 1D-geometry.

The thermodynamic properties of each cell are defined by the properties of the MatCalc ‘precipitation domain’ with the thermodynamic matrix phase bcc_a2 as defined in the corresponding thermodynamic and diffusion databases [70]. The precipitation domain linked to each cell, thus, contains information on the properties of ferrite and tempered martensite, respectively, relevant for the simulation routines. For analysis of the charging process, the surface H-concentration is set to a fixed mole fraction of $5.5 \cdot 10^{-5}$. The bulk concentration is initialized with a concentration 100 times less, i.e., a mole fraction of $5.5 \cdot 10^{-7}$. For discharging, the starting condition is a bulk H mole fraction of $5.5 \cdot 10^{-5}$ and the surface concentration is set to a value of $1.0 \cdot 10^{-12}$. The sketch given in Figure 4 illustrates this setup.

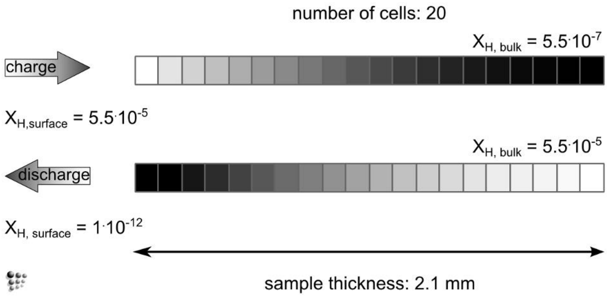

Figure 4: Sketch of the simulation grid for the calculated hydrogen charging and discharging processes.

Further input parameters for the H-diffusion simulation are the temperature, 30°C, and the trapping energy for H at the different types of precipitates.

6. Results of the diffusion simulation

In this chapter, we investigate the influence of NbC-traps on the charging and discharging processes. The significant impact of the utilized value for the trapping energy is shown in the subsequent section, where the trapping energy is varied between 18 and 56 kJ/mol, according to the reported spread of data in literature [71,72]. Then, we present an analysis of the influence of precipitates on the overall trapping efficiency. Finally, a comparison of the calculated H-diffusivities with diffusion coefficients given in literature is shown.

6.1 Charging and discharging processes

The plots in Figure 5 and Figure 6 summarize the charging curves for either the diffusion simulation without traps or the one with NbC as active traps. The plots in both figures show in a) the total H-content and in b) the free H-content in the lattice. Each line corresponds to the H-content transient of one of the cells in the spatial arrangement.

In the absence of traps, Figure 5, the H-content in the material increases rapidly to the prescribed surface concentration of $1.0 \cdot 10^{-5}$. The outmost cell with index 1, which is in contact with the atmosphere (externally applied H-content), reaches 90% of the final loading within around 500s. Due to rapid diffusion of H in steel, our simulation predicts that the rightmost cell arrives at this load value in less than 4000 s.

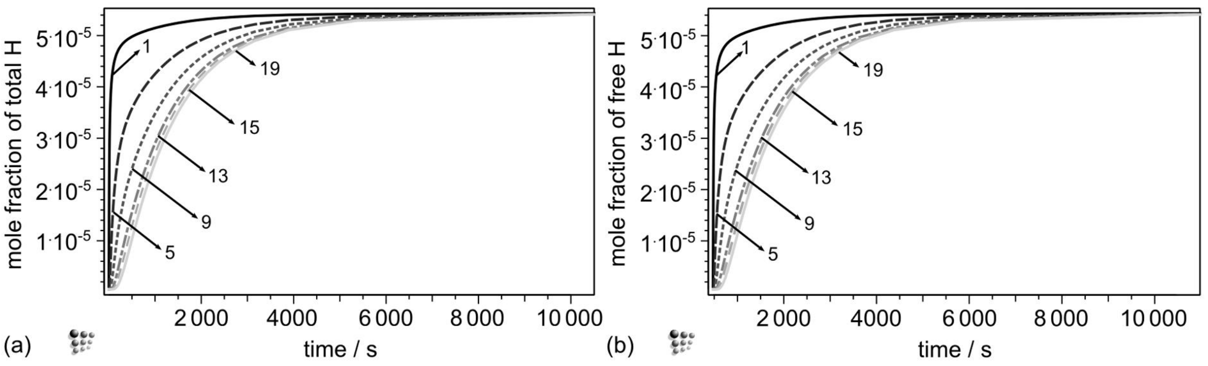

Figure 5: Charging kinetics for selected cells without traps. a) total H-content; b) free H-content.

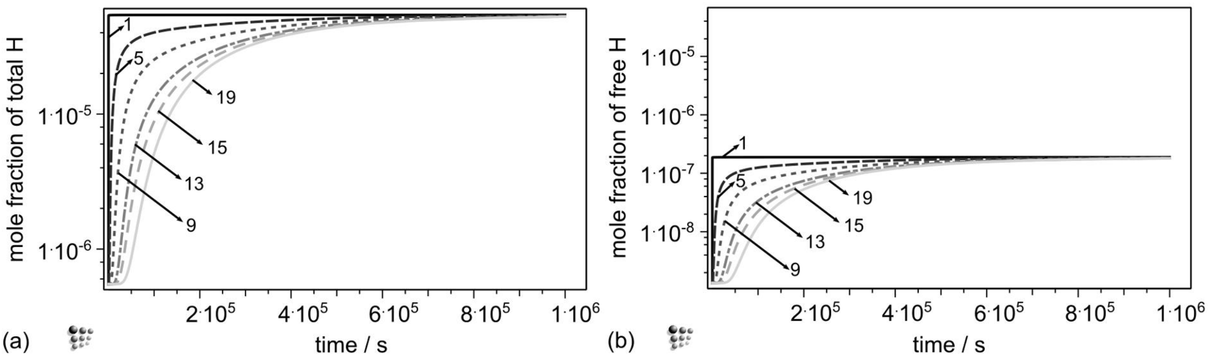

Figure 6: Charging kinetics for selected cells with NbC acting as traps with a trapping energy of 37 kJ/mol. a) total H-content; b) free H-content.

In the presence of NbC precipitation, H atoms are trapped on the particle surface [73] with one potential trapping position at each atom on the precipitate surface. The calculations are performed with a trapping energy of 37 kJ/mol, which is a representative mean value from various literature sources [71,72]. Figure 6 clearly shows that (i) H-diffusion is significantly impeded in the presence of traps. The H-content of cell 19 reaches 90% of the saturation level only after approximately 10^6 s, which is almost three orders of magnitude later than in the absence of trapping. (ii) The charging curve for the rightmost cell starts to increase only after a significant incubation period of about 30 000 s. When comparing any H-diffusion simulation with results obtained in permeation experiments, this delay time corresponds to the particular time when the first H-atoms have passed through the permeation sample and can be detected by some appropriate method. (iii) Most striking, the presence of strong H-traps reduces the amount of free H atoms, which are these atoms that are not trapped at the precipitate surface and move freely through the Fe lattice, by more than 2 orders of magnitude (Figure 6b). This latter effect also represents the main source for the substantially reduced long-range diffusive transport in the presence of trapping.

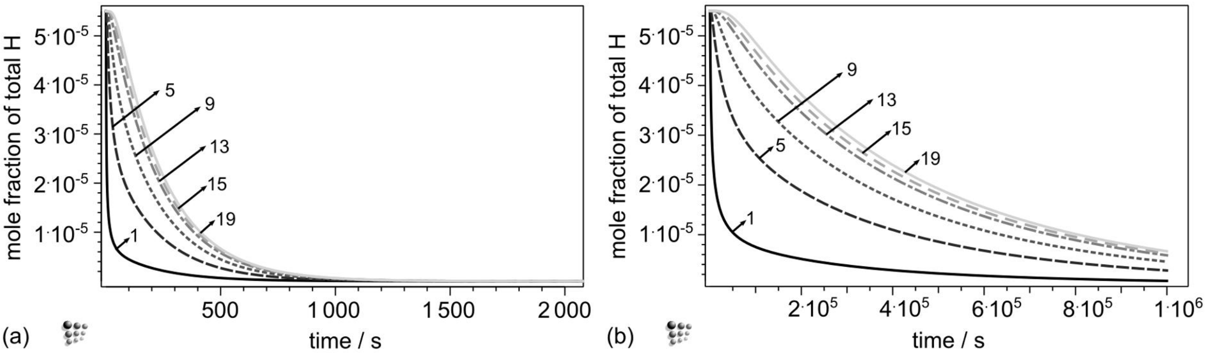

Figure 7: Discharging kinetics for selected cells a) without traps and b) in the presence of NbC-precipitates (ΔE = 37 kJ/mol); the y-axis shows the total H-content in the sample.

Figure 7 shows the discharging kinetics of selected cells starting from the charged condition, i.e., a total H-content of the mole fraction of $1.0 \cdot 10^{-5}$ and a predicted free H-content of the mole fraction of $1.9 \cdot 10^{-7}$ in the bulk and all traps containing the amount of H satisfying the equilibrium condition. The surface H-concentration is set to a mole fraction of $1.0 \cdot 10^{-12}$. The different discharging behaviour of the material is visualized without traps and in the presence of NbC with a trapping energy of 37 kJ/mol. The decrease of trapped H in the last cell of the diffusion sample starts after a significant delay in time. The discharging process cannot be fully accomplished within the simulation time.

6.2 Influence of trapping energy

The influence of different values for the trapping energy is visualized by the parameter study in Figure 8 and Figure 9. The trapping energy is varied between 18 kJ/mol and 56 kJ/mol (see e.g. refs. [71,72]), according to the values given in these literature sources. In the diagrams, the charging and discharging kinetics for the rightmost cell of the sample are compiled. On the y-axis, the total and the free H-content in the lattice are plotted.

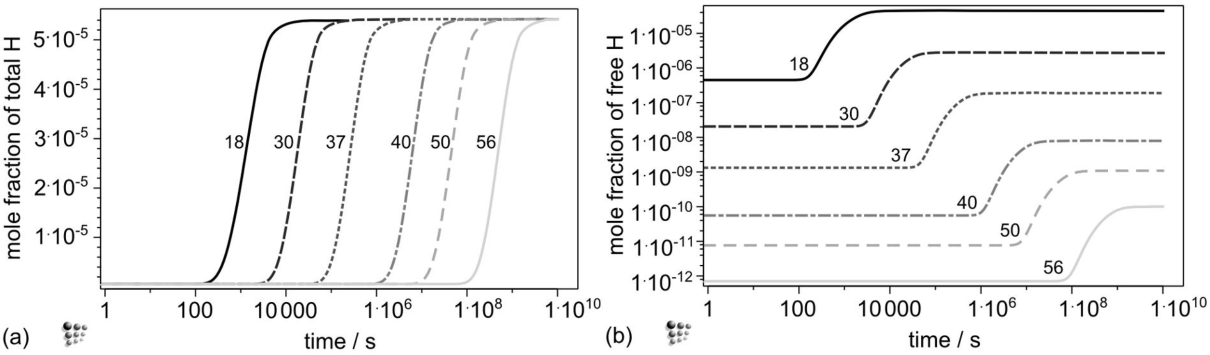

Figure 8: Influence of the binding energy on the free H-content in the lattice during simulated charging. The numbers in the plots indicate the applied values in kJ/mol. a) shows the total H-content and b) the free H-content in the lattice.

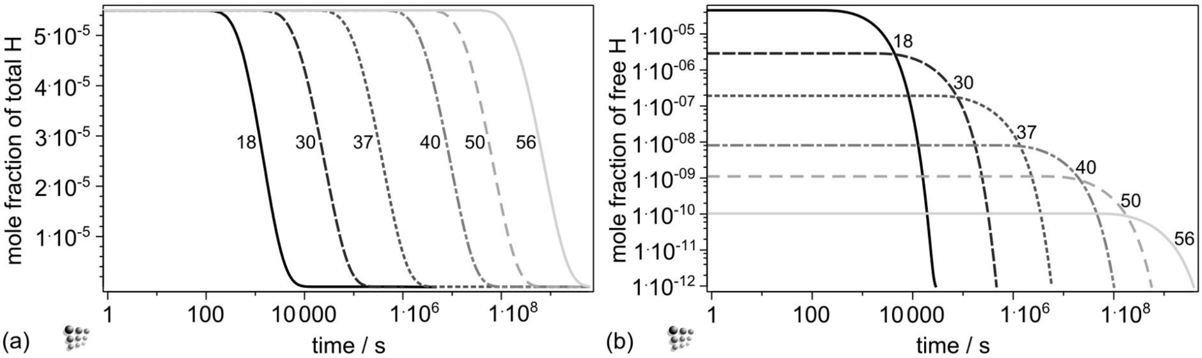

Figure 9: Influence of the binding energy on the free H-content in the lattice during simulated discharging. The numbers in the plots indicate the applied values in kJ/mol. a) shows the total H-content and b) the free H-content in the lattice.

With increasing trapping energy, a significant time delay is observed and the free H-content in the lattice is reduced by 7 orders of magnitude. In addition, the increasing time delay is significant between the minimum and maximum value for the trapping energy. From this example, it is evident that the selection of appropriate input data for any simulation of H diffusion is critical due to its severe impact on the results.

In determining the absolute values of the binding energy, Gehrmann et al. [74] carried out stationary as well as transient H permeation measurements. The first method was aimed at determining the binding energy of H atoms to 'weak' traps. With the latter, and applying the time-lag method, the binding energy of 'strong' traps was evaluated in model alloys of the type Fe-C-M, with M = Mo, Nb, V, Ti and Zr. The trapping enthalpies for the weak traps in all alloying systems were determined within a range of 13 to 21 kJ/mol. For the strong traps, the authors report values between 56 and 59 kJ/mol. For the binding energy to NbC precipitates in the same Fe-Nb-C model alloy, two different values were observed, 18 and 56 kJ/mol. These authors [74] suggested that the trapping potential of precipitates increases with their state of incoherency, i.e., the degree of incoherency between precipitate and matrix, in accordance with results reported in refs. [1,24,71].

In additional studies on the trapping potential of NbC-particles, see e.g. Wallaert et al. [75] and Wei et al. [76], thermal desorption spectroscopy was applied for determination of the activation energy of H to escape the traps. Wallaert et al. also observed a low energy peak in their desorption spectra with values between 24 and 33 kJ/mol. These authors came to the conclusion that the lower values should be attributed to the detrapping of H from grain boundaries. The higher desorption enthalpy values measured in these materials delivered an activation energy of 39 kJ/mol [75], which were attributed to H-trapping at NbC particles. For larger precipitates (100-200nm), the desorption activation energy increased to 48 kJ/mol. The authors in refs. [75,76] concluded that the misfit dislocation cores surrounding coherent or semicoherent interfaces of the particles represent efficient hydrogen traps. A value of > 60 kJ/mol was given for the material containing disk-like shaped NbC with a length >160 nm. For these particles, it was suggested that the H atoms are not trapped solely at the interface, but also in the carbon vacancies within the incoherent NbC precipitates, in accordance with the analysis of Wei and Tsuzaki [24] for TiC.

Choo and Lee [32] suggest that the binding energy should be evaluated as the difference of the desorption activation energy and the diffusion activation energy of H in the undisturbed lattice, which is 7.6 kJ/mol.

In view of the calculated particle distribution of the present steel, the mean value of 37 kJ/mol as used for the calculations in chapter 6.1, appears to be a plausible representative mean value. The parameter study in this section demonstrates quantitatively, how the exact nature of H interaction with the various traps impacts the long-range diffusion kinetics of H.

6.3 Influence of precipitate morphology and distribution on the trapping effect

To optimize industrial processes, such as tempering of steel, one has to understand the fundamental relation between precipitation behaviour and trapping effect. To illustrate this, a parameter study with one precipitate population (M_7C_3) nucleating at dislocations in a martensitic matrix is performed.

The result of a virtual tempering treatment at 500°C is shown in Figure 10. The points marked in the plots are connected with the different stages during the phase transformation. During nucleation (up to point A), the number density of precipitates increases continuously, reaching its maximum between 0.1s and 1s simulation time. In this stage, the precipitates are very small, the total precipitate/matrix interfacial area is large and, therefore, the trapping potential reaches its maximum. The smaller the value $\tilde{D}/D$ becomes, the stronger is the trapping effect (Figure 10d). The nucleation rate (Figure 10c) decreases to zero at the time when all available precipitate nucleation sites are occupied and/or the matrix is depleted from the precipitate-forming elements. In the growth stage, extending until the plateau in mean radius between points A and B is reached, the mean radius increases, the number density remains almost constant and the trapping effect remains to be substantial. With the onset of coarsening (point B) of the particles during further heating, the trapping effect decreases continuously. At point C, when the isothermal heat treatment temperature is reached, the mean radius of the particles still increases, the number density decreases and the trapping effect also decreases continuously.

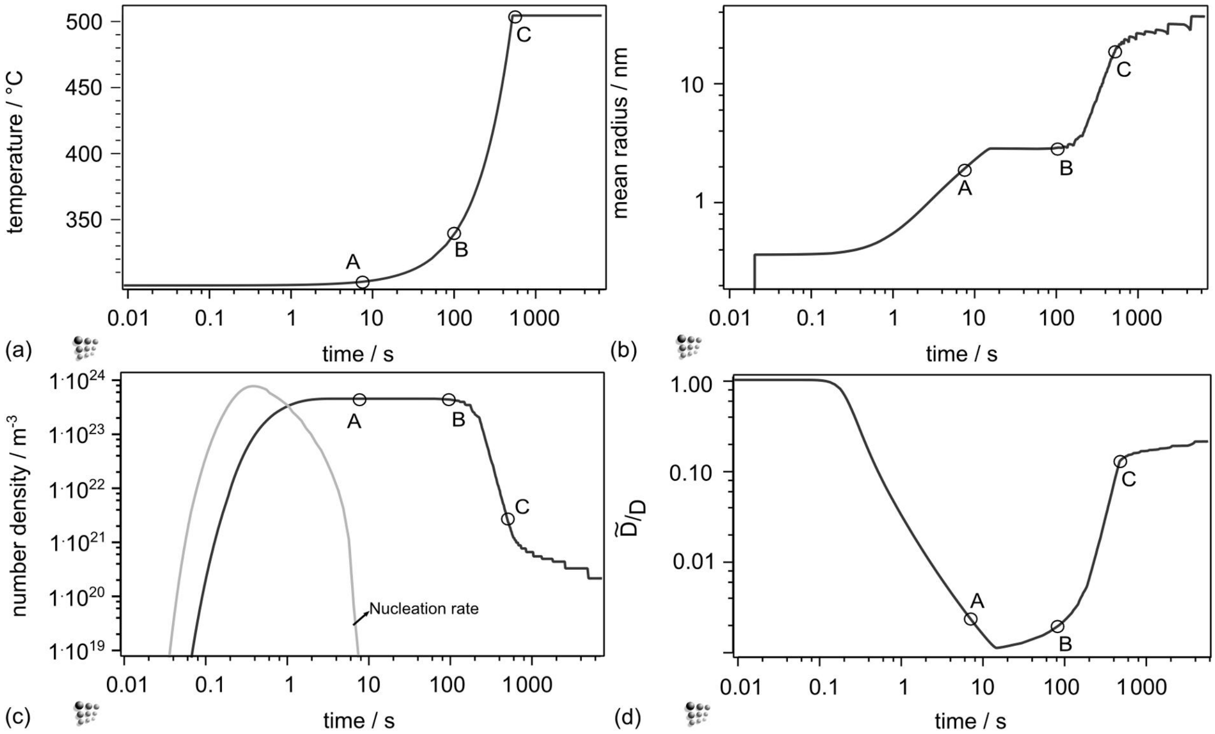

Figure 10: Effect of the different precipitation stages on the trapping effect.

A direct influence on the growth kinetics is observed by the shape of the precipitating phases [6,77]. This is investigated again on the example of M_7C_3, where the simulated shape is changed artificially from plates, to globular particles to needles utilizing the shape factor treatment described in ref. [78]. With the different shapes, the diffusion fields surrounding the particles are different, leading to a change in precipitate growth kinetics. From the plots in Figure 11, needle-like particles are observed to start growing later and also coarsen later compared to spherical and plate-like precipitates.

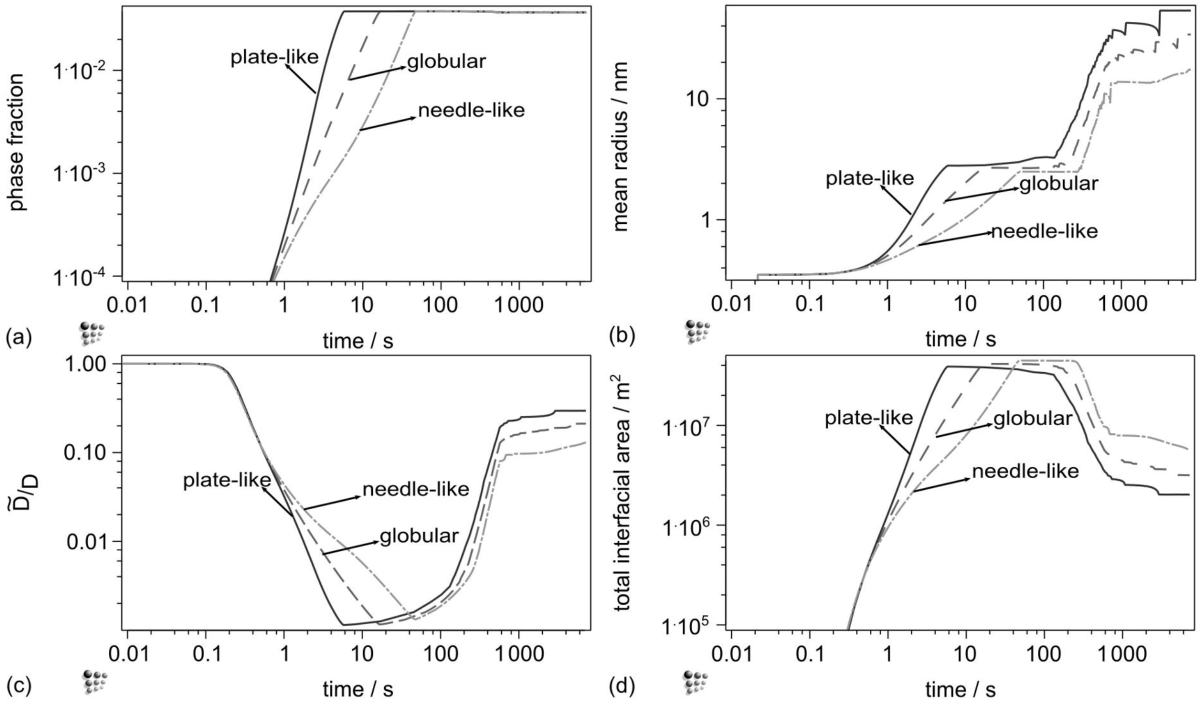

Figure 11: Influence of the particle shape on the trapping effect (annealing temperature 500°C).

Consequently, the particles remain smaller, their interfacial area is higher and the trapping effect of needle-like particles is stronger. From Figure 11, we again observe that smaller particles show a higher trapping potential compared to coarse ones at the same phase fraction (Figure 11b). This is in good accordance with observations from various literature sources [22,29,37]. The effect of temperature on the trapping effect is illustrated in Figure 12, where the trapping potential of globular particles at two different isothermal heat treatment temperatures is shown, again, emphasizing the important influence of the particle size distribution.

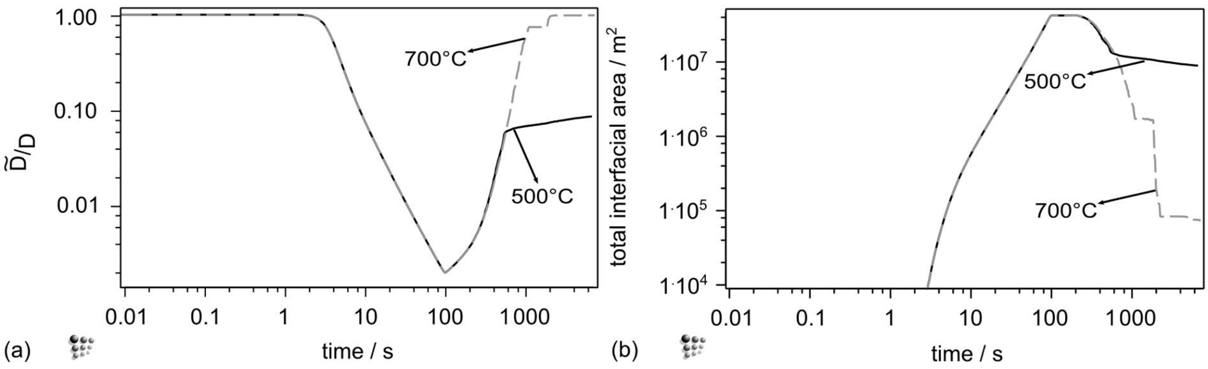

Figure 12: Influence of the isothermal heat treatment temperature: 500°C and 700°C. a) trapping effect of spherical particles. b) total interfacial area of spherical particles.

6.4 H-diffusion in the presence of multiple sorts of traps

In this last section, our simulation results are compared to diffusion coefficients of steels reported in literature. Figure 13 shows a comparison between literature data and calculated diffusion coefficients for H based on different types of traps and trapping energies. The values used in the simulation are summarized in Table 3. For comparison, the calculated diffusion coefficients at room temperature are indicated by the symbols on the left hand side of Figure 13.

Table 3: Calculated diffusion coefficient of H considering different kinds of traps.

Symbol	Trap	Trapping energy [kJ/mol] ΔE	D_{calc} [m²/s]
Filled triangle	TiN+M_7C_3+NbC+Cr+Mo	61 [79], 55 [80], 56 [79], 17 [3], 11 [79]	$1.41 \cdot 10^{-16}$
Circle	M_7C_3	55 [80]	$1.86 \cdot 10^{-16}$
Rectangle	NbC	56 [79]	$3.86 \cdot 10^{-15}$
Filled rectangle	NbC	18 [79]	$1.12 \cdot 10^{-9}$

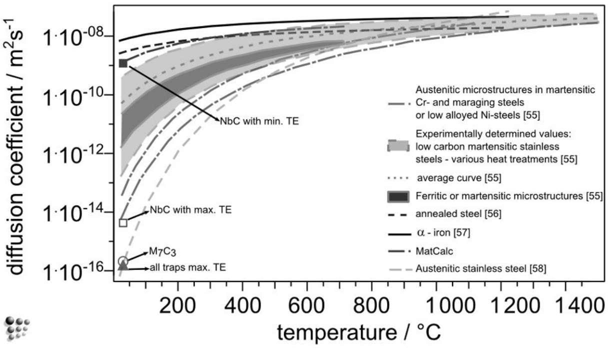

Figure 13: Comparison of calculated diffusion coefficients for hydrogen and measured diffusion coefficients from literature [81-84]. Symbols: filled triangle … all traps (max. trapping energy (TE) for TiN and NbC); circle … M_7C_3; rectangle … NbC (max. trapping energy); filled rectangle … NbC (min. trapping energy)

The authors in refs. [4,43] report that the broad scatter, which is found in the data for H-diffusion coefficients, can be explained by the presence of various types of traps in the material. This conclusion is well reproduced and confirmed in our calculations, which are shown in Figure 13. For example, if only one weak kind of trap is considered (NbC with min. ΔE) in the simulation as opposed to a situation with various kinds of strong traps (filled triangle), the full range of experimental values for the diffusion coefficient data is reproduced. Again, the severe influence of the trapping energy values is clearly visible in the results for NbC traps calculated with reported minimum and maximum values for the trapping energy (rectangles in Figure 13). The lowest calculated value is observed by consideration of all precipitating phases (with max. ΔE for NbC and TiN) and Cr and Mo in solid solution. From Figure 13, it is obvious that the largest influence on the long-range diffusion of H stems from the M_7C_3 particles (circle in Figure 13). This value is only slightly higher than the one calculated with all traps (filled triangle in Figure 13). As a consequence, every heat treatment that changes the M_7C_3 precipitation behaviour will also impact the effective diffusion coefficient of H.

7. Summary and Conclusions

In the present work, we describe the results obtained with a recently developed model for the simulation of long-range diffusion of hydrogen with simultaneous multi-component precipitation of carbo-nitrides in the presence of traps [44]. From the various parameter studies performed in this work and from comparison with experimental information, the following conclusions are drawn:

(1) Precipitates formed in microalloyed steel significantly influence the hydrogen long-range diffusion kinetics compared to the diffusivity of hydrogen measured in a material without active traps.

(2) In the presence of sufficiently strong traps, the delay time in discharging kinetics of a hydrogen loaded material can be considerable and reach several orders of magnitude.

(3) The trapping energy value substantially influences the trapping characteristics and diffusion kinetics. The literature data for the trapping energies show a broad scatter, thus indicating that these data have to be assessed carefully in future work in order to provide reliable input information for computer simulation.

(4) Different precipitate morphologies influence both, the growth kinetics during precipitation as well as the effective total precipitate/matrix interfacial area available for hydrogen trapping.

(5) The observed huge scatter of literature data on experimental hydrogen diffusivities in steel is clearly reproduced and explained by our simulations considering the existence of multiple sorts of traps, such as, e.g. alloying elements in solid solution, lattice defects, such as grain boundaries, and various precipitate populations.

8. References

[1] G.M. Pressouyre, A classification of hydrogen traps in steel, Metall. Mater. Trans. A 10A/10 (1979) 1571-1573, doi:10.1007/BF02812023

[2] J.P. Hirth, Effects of hydrogen on the properties of iron and steel, Metall. Mater. Trans. A 11A/6 (1980) 861-890, doi:10.1007/BF02654700

[3] K.T. Kim, J.K. Park, J.Y. Lee, S.H. Hwang, Effect of alloying elements on hydrogen diffusivity in ☐-iron, JOM 16/9 (1981) 2590-2596, doi:10.1007/BF01113601

[4] H.G. Lee, J.-Y. Lee, Hydrogen trapping by TiC particles in iron, Acta Metall. 32/1 (1984) 131-136, doi:10.1016/0001-6160(84)90210-4

[5] R.L.S. Thomas, J.R. Scully, R.P. Gangloff, Internal hydrogen embrittlement of ultrahigh-strength AERMET 100 steel, Metall. Mater. Trans. A 34A/2 (2003) 327-344, doi:10.1007/s11661-003-0334-3

[6] N. Parvathavarthini, S. Saroja, R.K. Dayal, H.S. Khatak, Studies on hydrogen permeability of 2.25%Cr-1%Mo ferritic steel: correlation with microstructure, J. of Nucl. Mater. 288/1-2 (2001) 187-196, doi:10.1016/s0022-3115(00)00706-6

[7] W.M. Robertson, A.W. Thompson, Permeation measurements of hydrogen trapping in 1045 steel, Metall. Mater. Trans. A 11A/4 (1980) 553-557, doi:10.1007/BF02670691

[8] E. Riecke, Untersuchungen zum Einfluss des Stahlgefüges auf die stationäre Wasserstoffpermeation, Mater. Corros. 32/2 (1981) 66-72, doi:10.1002/maco.19810320203

[9] M.F. Stevens, I.M. Bernstein, Microstructural trapping effects on hydrogen induced cracking of a microalloyed steel, Metall. Mater. Trans. A 20A/5 (1989) 909-919, 10.1007/BF02651657

[10] R. Valentini, A. Solina, S. Matera, P. De Gregorio, Influence of titanium and carbon contents on the hydrogen trapping of microalloyed steels, Metall. Mater. Trans. A 27A/12 (1996) 3773-3780, doi:10.1007/BF02595626

[11] Y. Huan, Y, A. Nakajima, A. Nishikata, T. Tsuru, Effect of mechanical deformation on permeation of hydrogen in iron, ISIJ Int. 43/4 (2003) pp. 548-554, doi:10.2355/isijinternational.43.548

[12] D. Li, R.P. Gangloff, J.R. Scully, Hydrogen trap states in ultrahigh-strength AERMET 100 steel, Metall. Mater. Trans. A 35A/3 (2004) 849-864, doi:10.1007/s11661-004-0011-1

[13] S. Serna, H. Martinez, S.Y. Lopez, J.G. Gonzalez-Rodriguez, J.L. Albarran, Electrochemical technique applied to evaluate the hydrogen permeability in microalloyed steels, Int. J. Hydrogen Energ. 30/12 (2005) 1333-1338, doi:10.1016/j.ijhydene.2005.04.012

[14] Y.F. Cheng, Analysis of electrochemical hydrogen permeation through X-65 pipeline steel and its implications on pipeline stress corrosion cracking, Int. J. Hydrogen Energ. 32/9 (2007) 1269-1276, doi:10.1016/j.ijhydene.2006.07.018

[15] M.J. Cancio, P. Bruzzoni, J.R. Collet-Lacoste, T.E. Perez, Hydrogen transport in 1Cr-0.7Mo steels charged with different hydrogen activities, Eurocorr 2008, UK

[16] S. Frappart, X. Feaugas, J. Creus, F. Thebault, L. Delattre, H. Marchebois, Study of the hydrogen diffusion and segregation into Fe-C-Mo martensitic HSLA steel using electrochemical permeation test, J. Phys. Chem. Solids 71/10 (2010) 1467-1479, doi:10.1016/j.jpcs.2010.07.017

[17] E. Fallahmohammadi, F. Bolzoni, L. Lazzari, Measurement of lattice and apparent diffusion coefficient of hydrogen in X65 and F22 pipeline steels, Int. J. Hydrogen Energ. 38/5 (2013) 2531-2543, doi:10.1016/j.ijhydene.2012.11.059

[18] A.J. Haq, K. Mzaka, D.P. Dunne, A. Calka, E.V. Pereloma, Effect of microstructure and composition on hydrogen permeation in X70 pipeline steels, Int. J. Hydrogen Energ. 38/5 (2013) 2544-2556, doi:10.1016/j.ijhydene.2012.11.127

[19] J. Rehrl, K. Mraczek, A. Pichler, E. Werner, The impact of Nb, Ti, Zr, B, V, and Mo on the hydrogen diffusion in four different AHSS/UHSS microstructures, Steel Res. Int. 85/3 (2014) 336-346, doi:10.1002/srin.201300087

[20] C. Mendibide, T. Sourmail, Composition optimization of high-strength steels for sulfide stress cracking resistance improvement, Corros. Sci. 51/12 (2009) 2878-2884, doi:10.1016/j.corsci.2009.08.013

[21] J.-Y. Lee, J.-L. Lee, A trapping theory of hydrogen in pure iron, Philos. Mag. A 56A/3 (1987) 293-309, doi:10.1080/01418618708214387

[22] F.-G. Wei, T. Hara, T. Tsuchida, K. Tsuzaki, Hydrogen trapping in quenched and tempered 0.42C-0.30Ti steel containing bimodally dispersed TiC particles, ISIJ Int. 43/4 (2003) 539-547, doi:10.2355/isijinternational.43.539

[23] F.-G.Wei, K. Tsuzaki, Hydrogen absorption of incoherent TiC particles in iron from environment at high temperatures, Metall. Mater. Trans. A 35A/10 (2004) 3155-3163, doi:10.1007/s11661-004-0060-5

[24] F.-G. Wei, K. Tsuzaki, Quantitative analysis on hydrogen trapping of TiC particles in steel, Metall. Mater. Trans. A 37A/2 (2006) 331-353, doi:10.1007/s11661-006-0004-3

[25] U. Hadam, T. Zakroczymski, Absorption of hydrogen in tensile strained iron and high-carbon steel studied by electrochemical permeation and desorption techniques, Int. J. Hydrogen Energ. 34/5 (2009) 2449-2459, doi:10.1016/j.ijhydene.2008.12.088

[26] S. Frappart, X. Feaugas, J. Creus, F. Thebault, L. Delattre, H. Marchebois, Hydrogen trapping in martensitic steel investigated using electrochemical permeation and thermal desorption spectroscopy, Scripta Mater. 65/10 (2011) 839-862, doi:10.1016/j.scriptamat.2011.07.042

[27] D. Perez-Escobar, K. Verbeken, L. Duprez, M. Verhaege, Evaluation of hydrogen trapping in high strength steels by thermal desorption spectroscopy, Mat. Sci. Eng.: A 551 (2012) 50-58, doi:10.1016/j.msea.2012.04.078

[28] T. Yamaguchi, M. Nagumo, Simulation of Hydrogen Thermal Desorption under Reversible trapping by lattice defects, ISIJ Int. 43/4 (2003) 514-519, doi:10.2355/isijinternational.43.514

[29] J.C. Charbonnier, H. Margot-Marette, A.M. Brass, M. Aucouturier, Sulfide stress cracking of high strength modified Cr-Mo steels, Metall. Mater. Trans. A 16A/5 (1985) 935-944, doi:10.1007/BF02814846

[30] M. Garet, A.M. Brass, C. Haut, F. Guttierez-Solana, Hydrogen trapping on non metallic inclusions in Cr-Mo low alloy steels, Corros. Sci. 40/7 (1998) 1073-1086, doi:10.1016/s0010-938x(98)00008-0

[31] G. Katano, K. Ueyama, M. Mori, Observation of hydrogen distribution in high-strength steel, J. Mater. Sci. 36/9 (2001) 2277-2286, doi:10.1023/A:1017568706014

[32] W.Y. Choo, J.Y. Lee, Thermal analysis of trapped hydrogen in pure iron, Metall. Mater. Trans. A 13A/1 (1982) 135-140, doi:10.1007/BF02642424

[33] T. Ohmisawa, S. Uchiyama, M. Nagumo, Detection of hydrogen trap distribution in steel using a microprint technique, J. Alloy. Compd. 356-357 (2003) 290-294, doi:10.1016/s0925-8388(03)00355-4

[34] A. Nagao, K. Hayashi, K. Oi, S. Mitao, Effect of uniform distribution of fine cementite on hydrogen embrittlement of low carbon martensitic steel plates, ISIJ Int. 52/2 (2012) 213-221, doi:10.2355/isijinternational.52.213

[35] G.M. Pressouyre, I.M. Bernstein, A quantitative analysis of hydrogen trapping, Metall. Mater. Trans. A 9A/11 (1978) 1571-1580, doi:10.1007/BF02661939

[36] G.M. Pressouyre, I.M. Bernstein, An example of the effect of hydrogen trapping on hydrogen embrittlement, Metall. Mater. Trans. A 12A/5 (1981) 835-844, doi:10.1007/BF02648348

[37] Y. Liu, M. Wang, G. Liu, Effect of hydrogen on ductility of high strength 3Ni-Cr-Mo-V steels, Mat. Sci. Eng.: A 594 (2014) 40-47, doi:10.1016/j.msea.2013.11.058

[38] G.L. Spencer, D.J. Duquette, The role of vanadium carbide traps in reducing the hydrogen embrittlement susceptibility of high strength alloy steels, Tech. Reports US Army armament research and engineering center watervliet ny benet labs (1998) 27 p, No. TR-ARCCB-TR-98016

[39] T. Yokota, T. Shiraga, Evaluation of hydrogen content trapped by vanadium precipitates in steel, ISIJ Int. 43/4 (2003) 534-538, doi:10.2355/isijinternational.43.534

[40] H. Asahi, D. Hirakami, S. Yamasaki, Hydrogen trapping behaviour in vanadium-added steel, ISIJ Int. 43/4 (2003) 527-533, doi:10.2355/isijinternational.43.527

[41] G. Lopez Turconi, G. Echaniz, G. Cumino, E. Anelli, L. Scoppio, T. Perez, C. Morales, Improvement of resistance to SSC initiation and propagation of high strength OCTG through microstructure and precipitation control, Corrosion 2001 (2001) conference paper no. 01077

[42] R.A. Oriani, The diffusion and trapping of hydrogen in steel, Acta Met. 18/1 (1970) 147-157, doi:10.1016/0001-6160(70)90078-7

[43] A. McNabb, P.K. Foster, A new analysis of the diffusion of hydrogen in iron and ferritic steel, Trans. AIME 227 (1963) 618-627

[44] J. Svoboda, F.D. Fischer, Modelling for hydrogen diffusion in metals with traps revisited, Acta Mater. 60/3 (2012) 1211-1220, doi:10.1016/j.actamat.2011.11.025

[45] F.D. Fischer, J. Svoboda, E. Kozeschnik, Interstitial diffusion in systems with multiple sorts of traps, Modelling Simul. Mater. Sci. Eng. 21/2 (2013) 025008/ 13p, doi:10.1088/0965-0393/21/2/025008

[46] J. Svoboda, Y.V. Shan, E. Kozeschnik, F.D. Fischer, Determination of depths of traps for interstitials from thermodynamic data: a new view on carbon trapping and diffusion, Modelling Simul. Mater. Sci. Eng.21/6 (2013) 065012/ 15p, doi:10.1088/0965-0393-/21/6/065012

[47] F.D. Fischer, G. Mori, J. Svoboda, Modelling the influence of trapping on hydrogen permeation in metals, Corr. Sci. 76 (2013) 382-389, doi:10.1016/j.corsci.2013.07.010

[48] website http://matcalc.at

[49] R. Kampmann, R. Wagner, Decomposition of alloys, the early stages, Proc. of the 2nd Acta-Scripta Metallurgica Conf., Oxford, UK, 1984

[50] B. Sonderegger, E. Kozeschnik, Generalized nearest-neighbor broken-bond analysis of randomly oriented coherent interfaces in multicomponent fcc and bcc structures, Metall. Mater. Trans. A 40A/3 (2009) 499-510, doi:10.1007/s11661-008-9752-6

[51] B. Sonderegger, E. Kozeschnik, Size dependence of the interfacial energy in the generalized nearest-neighbor broken-bond approach, Scripta. Mater. 60/8 (2009) 635-638, doi:10.1016/j.scriptamat.2008.12.025

[52] B. Sonderegger, E. Kozeschnik, Interfacial energy of diffuse phase boundaries in the generalized broken-bond approach, Metall. Mater. Trans. A 41/12 (2010) 3262-3269, doi:10.1007/s11661-010-0370-8

[53] L. Onsager, Reciprocal relations in irreversible processes I., Phys. Rev. I 37 (1931) 405-426, doi:10.1103/PhysRev.37.405
L. Onsager, Reciprocal relations in irreversible processes II., Phys. Rev. II 38 (1931) 2265-2279, doi:10.1103/PhysRev.38.2265

[54] J. Svoboda, F.D. Fischer, P. Fratzl, E. Kozeschnik, Modelling of kinetics in multi-component multi-phase systems with spherical precipitates I: Theory, Mat. Sci. Eng.: A 385/1-2 (2004) 166-174, doi:10.1016/j.msea.2004.06.018

[55] E. Kozeschnik, J. Svoboda, P. Fratzl, F.D. Fischer, Modelling of kinetics in multi-component multi-phase systems with spherical precipitates II: Numerical solution and application, Mat. Sci. Eng.: A 385/1-2 (2004) 157-165, doi:10.1016/j.msea.2004.06.016

[56] E. Kozeschnik, J. Svoboda, F.D. Fischer, Modified evolution equations for the precipitation kinetics of complex phases in multi-component systems, Calphad 28/4 (2004) 379-382, doi:10.1016/j.calphad.2004.11.003

[57] J. Svoboda, I. Turek, D.D. Fischer, Application of the thermodynamic extremal principle to modeling of thermodynamic processes in material sciences, Phil. Mag. 85/31 (2005) 3699-3707, doi:10.1080/14786430500267760

[58] B. Sonderegger, E. Kozeschnik, H. Leitner, H. Clemens, J. Svoboda, F.D. Fischer, Computational analysis of the precipitation kinetics in a complex tool steel, Int. J. Mat. Res. 99/4 (2008) 410-415, doi:10.3139/146.101653

[59] R. Radis, M. Schaffer, M. Albu, G. Kothleitner, P. Pölt, E. Kozeschnik, Multimodal size distributions of ☐' precipitates during continuous cooling of UDIMET 720 Li, Acta Mater. 57/19 (2009) 5739-5747, doi:10.1016/j.actamat.2009.08.002

[60] I. Holzer, E. Kozeschnik, Simulation of Copper Precipitation in Fe-Cu Alloys, Mater. Sci. Forum 638-642 (2010) 2579-2584

[61] R. Radis, E. Kozeschnik, Kinetics of AlN precipitation in microalloyed steel, Modelling Simul. Mater. Sci. Eng. 18/5 (2010) 055003, doi:10.1088/0965-0393/18/5/055003

[62] M. Pudar, S. Zamberger, K. Spiradek-Hahn, R. Radis, E. Kozeschnik, Computational analysis of precipitation during continuous casting of microalloyed steel, Steel Res. Int. 81/5 (2010) 372-380, doi:10.1002/srin.201000021

[63] http://www.thermocalc.com/products-services/software/dictra/

[64] http://www.questek.com/materials-by-design.html

[65] http://www.computherm.com

[66] http://www.thermocalc.com/products-services/software/tc-prisma/

[67] E. Kozeschnik, „Modeling Solid-State Precipitation“, Momentum Press, New York, 2013, pp. 308 ff., doi:10.5643/9781606500644

[68] S. Zamberger, T. Wojcik, J. Klarner, G. Klösch, H. Schifferl, E. Kozeschnik, Computational and experimental analysis of carbo-nitride precipitation in tempered martensite, Steel Res. Int. 84/1 (2013) 20-30, doi:10.1002/srin.201200047

[69] A. Engström, L. Höglund, J. Ågren, Computer simulation of diffusion in multiphase systems, Metall. Mater. Trans. A 25A/6 (1994) 1127-1134, doi:10.1007/BF02652288

[70] Thermodynamic database: mc_fe_v2.029; database for diffusion data: mc_fe_v2.007. Institute of Materials Science and Technology, TU Wien, Austria.

[71] F. Gehrmann, „Einfluss der Nitride von V, Nb und Ti auf die Diffusion und Löslichkeit von Wasserstoff in Eisen“, PHD-thesis TU Dortmund University; Fortschritt-Berichte VDI, VDI-Verlag GmbH, 1994

[72] H.J. Grabke, F. Gehrmann, E. Riecke, Hydrogen in microalloyed steels, Steel Res. Int. 72/5-6 (2001) 225-235

[73] P. Lang, M. Rath, E. Kozeschnik, P.E.J. Rivera-Diaz-del-Castillo, Modelling the influence of austenitisation temperature in hydrogen trapping in Nb

containing martensitic steels, Scripta. Mater. 101 (2015) 60-63, doi:10.1016/j.scriptamat.2015.01.019

[74] F. Gehrmann, E. Riecke, H. Grabke, Einfluss der Nitride von Mo, V, Nb, Ti und Zr auf die Korrosion und Wasserstoffaufnahme von Stählen im Vergleich mit deren Karbiden, Technische Forschung Stahl EUR 16083 ISBN 92-828-1428-9 (1997)

[75] E. Wallaert, T. Depover, A. Muhammad, K. Verbeken, Thermal desorption spectroscopy evaluation of the Hydrogen-trapping capacity of NBC and NbN precipitates, Metall. Mater. Trans. A 45A/5 (2014) 2412-2420, doi:10.1007/s11661-013-2181-1

[76] F. Wei, K. Tsuzaki, Hydrogen trapping character of nano-sized NbC precipitates in tempered martensite, Proc. 2008 Int. Hydrogen Conf., 1st ed., ASM International, Wyoming, WY (2008), 456-463

[77] H.J. Kang, J.S. Yoo, J.T. Park, S.T. Ahn, N. Kang, K.-M. Cho, Effect of nano-carbide formation on hydrogen-delayed fracture for quenching and tempering steels during high-frequency induction heat treatment, Mat. Sci. Eng. A-Struct. 543 (2012) 6-11, doi:10.1016/j.msea.2012.02.008

[78] E. Kozeschnik, J. Svoboda, F.D. Fischer, Shape factors in modeling of precipitation, Mat. Sci. Eng. A-Struct. 441 (2006) 68-72, doi:10.1016/j.msea.2006.08.088

[79] J. Rehrl, Wasserstoffversprödung in hochfesten, mikrolegierten Stählen, PHD-thesis Technical University of Munich; Institute of Materials Science and Mechanics of Materials (2014) 186p

[80] D.M. Symons, G.A. Young, J.R. Scully, The effect of strain on the trapping of hydrogen at grain-boundary carbides in Ni-Cr-Fe alloys, Metall. Mater. Trans. A 32A/2 (2001) 369-377, doi:10.1007/s11661-001-0268-6

[81] Th. Boellinghaus, H. Hoffmeister, K. Feuerstake, H. Alzer, J. Krewinkel, Finite element calculation of hydrogen uptake and diffusion in martensitic stainless steel welds, Mathematical Modelling of Weld Phenomena 4 (1998) Cerjak, H. ed.; The Institute of Materials, London

[82] J.S. Georgiev, L.A. Anestiev, Influence of the surface processes on the hydrogen permeation through ferritic steel and amorphous Fe40Ni40Mo4B16 alloy specimens, J. of Nuclear Materials 249/2 (1997) 133-141, doi:10.1016/s0022-3115(97)00228-6

[83] K. Kiuchi, R.B. McLellan, The solubility and diffusivity of hydrogen in well-annealed and deformed iron, Acta Metallurgica 31/7 (1983) 961-984, doi:10.1016/0001-6160(83)90192-x

[84] Y. Mine, T Kimoto, Hydrogen uptake in austenitic stainless steels by exposure to gaseous hydrogen and its effect on tensile deformation, Corros. Sci. 53/8 (2011) 2619-2629, doi:10.1016/j.corsci.2011.04.022